Characterization of Reactor Background Radiation at HFIR for the PROSPECT Experiment

A Thesis Presented for the

Master of Science

Degree

The University of Tennessee, Knoxville

Blaine Alexander Heffron

May 2017

I dedicate this work to my family and friends who have supported me throughout my time at UT.

Acknowledgments

I would like to thank my colleagues that helped me with this work, especially Elisa and Brennan for helping take measurements and plan the experiments, James for helping with various computational and programmatic challenges, and Michael F. for his help with the liquid neutron detectors. I'd like to thank the post-docs in the PROSPECT collaboration, especially Tom for helping setup the P2C experiment, Michael for his extensive analysis and simulation libraries, and Karin for her quick-start guide to ROOT analysis. I'd also like to thank the guys at HFIR, especially David G. for his help getting radioactive sources for efficiency measurements and Geoffrey for providing us with just about any information we needed regarding the reactor.

Thanks to the secretaries Anne, Sherry, Chrisanne, and Jessica for helping me navigate the bureaucracies of ORNL and UTK.

Thanks to Charlie and David R. for their expertise in regards gamma ray spectroscopy.

Thanks to Anna for providing me with the work opportunity at LANL and sharing her knowledge of reactor physics.

Thanks to Krzysztof for letting me help with the MTAS experiment.

Thanks to Sakaguchi-san for providing me with the opportunity to help with the SAMURAI experiment at RIKEN.

Finally, thanks to Alfredo for advising and providing the opportunities to perform this work.

Abstract

This work describes an investigation of the background radiation present at the High Flux Isotope Reactor (HFIR) on behalf of the PROSPECT collaboration. The PROSPECT experiment is designed to make a precision measurement of the antineutrino spectrum at HFIR and search for sterile neutrinos. Temporal and spacial variation of neutron and gamma backgrounds at the experiment site for the PROSPECT detector are measured in order to determine if the reactor correlated radiation will contribute a significant background to the inverse beta decay signal. Knowledge of spacial background variation will also be used to inform the design of a local shield wall that is being built to mitigate gamma backgrounds entering the experiment hall. PROSPECT will be a movable detector, allowing it to measure at positions between 7 meters (near) and 12 meters (far) from the reactor core. While the reactor is on, we measured variation in gamma rates between 50% and 175% of the average at various positions throughout the volume of the near position. We find that the average gamma rate in the far position is 30% of the average gamma rates at the near position. Rate histories for neutron and gamma measurements are provided for entire reactor on cycles, and correlations are found between fluctuations in radiation and beamline operations below the experiment location. Simulation of the proposed PROSPECT detector along with its shielding package is carried out to determine the impact of reactor correlated backgrounds. We find an inverse beta decay event rate of 0.01 mHz within the region of interest from the ambient reactor on gamma field, compared to a 9.51 ± .70 mHz event rate from cosmic

radiation. The backgrounds induced by a nearby materials irradiation experiment which may run during portions of PROSPECT's data taking are also investigated through measurement and simulation.

Table of Contents

List of Tables

List of Figures

Chapter 1

Introduction

This work details background measurements and simulations that have been carried out on behalf of the PROSPECT[1] experiment at Oak Ridge National Laboratory's (ORNL) High Flux Isotope Reactor (HFIR)[2]. The PROSPECT experiment aims to measure the reactor antineutrino spectrum using nearly four tons of ^{6}Li doped liquid scintillator and test for short baseline neutrino oscillation with a segmented detector that is movable within a range of 7-12 meters from the reactor core. A study of cosmic backgrounds at HFIR was previously carried out[3], finding that reactor-correlated backgrounds contribute orders of magnitude fewer counts in the region of interest for inverse beta decay (IBD) signals. This work is a more detailed study focusing on how the reactor-correlated neutrons and gammas vary throughout the experiment hall spatially and in time as reactor and beamline operations are carried out.

1.1 Motivation

The motivation for this work comes from the need to understand all sources of background for IBD detection at the HFIR site. The goal of the PROSPECT program is to measure the reactor antineutrino spectrum with an energy resolution of $4.5\%/\sqrt{E}$, which will require detailed knowledge of reactor backgrounds to ensure that these contribute well below the IBD signal. The motivation for measuring the antineutrino spectrum is twofold: recent reactor antineutrino measurements found a spectral shape discrepancy in the 5 to 7 MeV region[4] [5] [6] (henceforth called "the bump"), and an updated prediction of the expected reactor antineutrino flux[7] creates a 6% flux deficit on average for all previous reactor measurements[8] (henceforth called "the anomaly"). The expected antineutrino spectrum is calculated either using a "conversion method" in which measured reactor electron spectrum from ILL[9] (recently republished in finer detail in [10]) is converted to antineutrino energy or a "summation method" in which antineutrino spectra from each beta decaying nuclei of each fission daughter is summed together. Each have their own uncertainties ranging from errors in nuclear physics data such as fission yields and beta branching ratios obtained from the nuclear databases or corrections to the calculated beta decay spectra for forbidden transitions[11]. With ^{239}Pu and ^{241}Pu being ruled out as sole culprits of the bump[12], a measurement at a highly-enriched Uranium (HEU) reactor such as HFIR which burns nearly 100% ^{235}U will be crucial for disentangling the various sources of the discrepancy.

The reactor deficit can also result from uncertainties in fission yields and branching ratios, with ^{235}U being a primary suspect[13]. Another popular explanation for the deficit is the existence of eV-scale sterile neutrinos[14] [15] [16]. With a movable detector design, PROSPECT will be able to probe the best fit region of the parameter space for ν_e disappearance with a single eV-scale sterile neutrino with a $> 4\sigma$ confidence level within 1 year of running. Because the detector will move within a span of 5 meters, knowledge of the environmental backgrounds as the detector moves between near and far positions will be critical for optimal background subtraction, and will be one of the focuses of this work.

1.2 Thesis Outline

Chapter 2 begins with a history of neutrino detection, leading up to the discovery of flavor oscillation. We then describe various reactor antineutrino measurements which sets the stage for the PROSPECT physics program. Anomalies in the recent reactor antineutrino measurements are discussed along with a brief description of the sterile neutrino hypothesis which has been posited to address the anomalies.

Chapter 3 lists the hardware used for the background measurements for this work, along with a description of the various experimental setups. Additionally, some information on the detection principles for scintillating detectors which includes light collection, light detection, and signal processing is included.

Chapter 4 describes the PROSPECT experiment including detector layout, description of the experiment site, detection method, and existing background studies that have been performed on-site. Then details are given regarding recent background measurements focusing on neutron and gamma radiation as a function of position within the experiment hall along with rate histories throughout reactor-on and reactor-off cycles.

Chapter 5 goes into more detail regarding the analysis of each detector type, including pulse digitization, energy histogram analysis, calibration, detector efficiency, and energy resolution.

Finally Chapter 6 describes various simulations carried out in order to better understand the impact of the measured backgrounds on the final PROSPECT detector. This includes analysis of radiation from cosmogenics, room backgrounds including reactor-correlated gammas, and backgrounds from a nearby materials irradiation facility (MIF). This chapter concludes with results on predictions for the IBD background rates that will be seen by PROSPECT from the various sources of radiation present at HFIR while the reactor is on.

Chapter 2

Neutrino Physics - History and recent anomalies

In this chapter we review the experimental history of neutrino experiments, dating back to the first detection in 1953. We then discuss the current anomalies in both shape and overall rate from reactor experiments, and detail a few possible explanations for said anomalies.

2.1 History of Neutrino Detection

The neutrino was first described in 1934 by Fermi in his theory of Beta Decay, in which the reaction

$$n^0 \rightarrow p^+ + e^- + \bar{\nu}_e \tag{2.1}$$

was postulated in order to explain the continuous spectrum of electron energies measured from beta decaying nuclei. In this reaction the $\bar{\nu}_e$ would be an additional neutral particle emitted in order to share kinetic energy with the electron while still conserving charge. It wasn't until 1956 when the first neutrino was detected using a source of antineutrinos from a nuclear reactor at Savanna River Site[17]. Now known as the Reines and Cowan experiment, the inverse beta decay (IBD) reaction

$$\bar{\nu_e} + p \rightarrow n + e^+ \tag{2.2}$$

was detected using a container of water to provide protons for the IBD interactions. The container was surrounded by liquid scintillator and photomultiplier tubes (PMTs) used to detect the annihilation gammas from the outgoing positron. The outgoing neutron was detected via neutron capture on cadmium, which was dissolved into the water using a cadmium chloride mixture. This pioneering experiment draws many parallels to modern day antineutrino experiments which are in essence a refinement of this same experimental technique.

Questions remained about this neutral particle, such as its rest mass. The first experiment to measure the neutrino's velocity in 1976[18] used a comparison of muon and neutrino velocities, finding that the neutrino velocity agreed with the speed of light in vacuum at a 95% confidence level. Experiments since, including the latest measurement by OPERA[19], confirm this finding measuring $(v - c)/c = (2.7 \pm 3.1(stat.)^{+3.4}_{-3.3}(sys.)) \times 10^{-6}$.

The first experimental evidence of a nonzero neutrino mass came back in 1968, when Davis et al. measured the solar neutrino flux finding a deficit relative to experimental calculations[20]. This result was confirmed in 1989 by the Kamiokande experiment[21], and later by the GALLEX[22] and SAGE[23] experiments. These results point to neutrino flavor oscillation, which can only be possible if the neutrino has a nonzero rest mass[24]. In 1996, the LSND experiment claimed evidence of $\nu_\mu \rightarrow \nu_e$ oscillation[25], finding an oscillation probability of $0.31 \pm 0.05(stat.)^{+0.11}_{-0.10}(sys.)$. Since then a number of experiments have been carried out to measure the oscillation parameters that describe neutrino mixing.

2.2 Spectral Shape and Rate Anomalies

In 1981, a measurement of the electron spectrum from the high flux ILL reactor in Grenoble, France was performed by Schreckenbach et al. in order to provide a reference for experimental measurements of the reactor antineutrino spectrum [9]. This measurement provides the basis for the antineutrino spectra calculated by the so-called conversion method, in which the antineutrino spectra is calculated from the electron spectra [7], which takes into account coulombic repulsion of the outgoing electron not experienced by the antineutrino. Another approach to calculating the antineutrino spectrum for a reactor is to sum the antineutrino spectrum calculated for each beta decay transition for each of the fission products for a given fissioning nuclei, relying on nuclear databases for fission branching ratios and transition strengths and energies of the decay [26]. The Huber-Mueller model is the combination of the conversion method and $ab{-}initio$ approach [27] [7]. Reactor antineutrino measurements taken at ILL-Grenoble [9], Gösgen [28], Rovno [29], Krasnoyarsk [30], Savannah River [31], and Bugey [32] found a flux that is on average $94.4 \pm 2.3\%$ of the intensity predicted by the Huber-Mueller model, a discrepancy known as the reactor antineutrino anomaly [8].

In addition to a discrepancy detected in the overall rate of neutrinos coming from reactors, the latest Θ_{13} measurements by Daya Bay [4], Reno [5], and Double Chooz [6] provide antineutrino spectra with shapes inconsistent with the Huber-Mueller model, specifically finding the flux in the $5 - 7MeV$ region is higher than expected [11].

The deficit of reactor antineutrinos being detected cannot be explained by the current values of the oscillation parameters measured for Θ_{13} and Θ_{12}. While there are a number of systematic effects that could cause such a discrepancy, ranging from errors in the ILL measurement to lack of accuracy in nuclear databases, there are also theoretical explanations for the deficit. The most popular explanation is one or more sterile neutrino flavors [15] which could provide oscillation at small distances (meter to kilometer scale). Oscillations at this length scale would be detectable by antineutrino measurements near reactors, hence the motivation for the PROSPECT experiment. PROSPECT's movable design allows for a definitive test for light sterile neutrinos over a specific region of the model space. To visualize the coverage of the sterile neutrino parameter space by the PROSPECT experiment, see A.2.

Chapter 3

Instrumentation for HFIR Background Measurements

This chapter consists of details on the setups used for background measurements and information about the hardware used. It also includes the operating principles for each of the detector types used.

3.1 Overview of Setups

A number of campaigns have been undertaken in order to characterize the background radiation during both reactor-off and on periods in the experiment hall within the vicinity of the future PROSPECT experiment. The first major campaign using a 20 liter test cell known as P20[1] was deployed in order to understand the IBD-like backgrounds in the on-site environment using LiLS similar to that which will be used in the full experiment. The cell was deployed within a shielding package which can be viewed in figure 3.1. The major finding of P20 was that such a shielding package successfully mitigated reactor correlated backgrounds for IBD events to levels that the single cell was insensitive to, implying that cosmic backgrounds were the dominant source of time correlated IBD events. This work will focus on subsequent deployments of sodium iodide (NaI) and various neutron detectors in order to better characterize the ambient reactor-correlated backgrounds to ensure that this assumption is valid, and to predict the impact of these backgrounds in the full detector which, due to space and weight constraints, will utilize a thinner passive shield relative to P20. The subsequent sections will detail the hardware and measurement procedures for the background campaigns taken since the completion of P20.

3.1.1 P2C

The first campaign after P20 will be called P2C, named because a 2-liter test cell was placed inside the P20 shielding package after the 20-liter cell was removed for further testing at Yale[33]. In addition to the 2-liter cell, a 2" NaI detector, a 2" deuterated liquid scintillator, a 4" deuterated liquid scintillator, and a 1" outer diameter (OD) x 12" ^{3}He tube was placed inside of the P20 shielding package. Note the deuterated liquid is commercially available Eljen-315[34] liquid scintillator. Identical models for each of these detectors excluding the 2-liter test cell were deployed outside of the shielding for comparison to determine the shielding factor for thermal neutrons (meV - eV), fast neutrons (MeV), and MeV scale gammas.

The detectors inside the shield had voltage applied for a 10 month long period which allowed for analysis of rate variations of gamma and neutron radiation throughout a number of reactor-on cycles. Additionally, scans along the surface of the shield with the identical 2" NaI and deuterated detectors were done to investigate variation of radiation entering the shield at different positions along its surface. Data is presented in section 4.5.1.

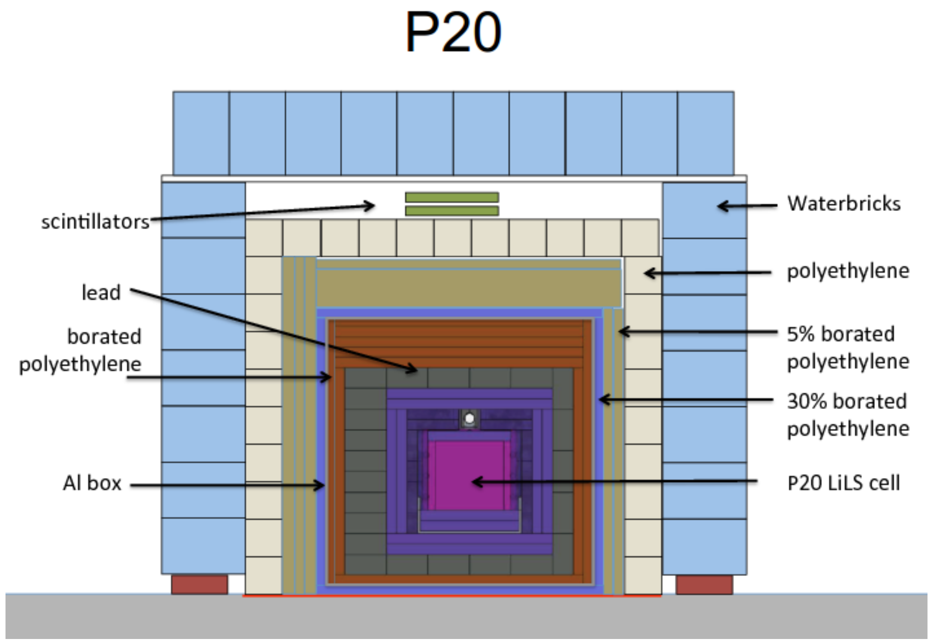

Figure 3.1: Shielding used in the P20 and P2C experiments.

3.1.2 Position Scans with NaI Detectors

After sufficient information was obtained from the P2C experiment, the P20 shielding package was dismantled. Initial reactor-on and reactor-off scans were done throughout the experiment hall using a 2 x 2 array of 2" x 4" x 16" NaI detectors. This was done by biasing the detectors and performing calibrations with ^{60}Co and ^{137}Cs before beginning the scan, then taking data at each location for 5 minutes. After a 5 minute time period elapsed, the acquisition would be turned off then the array moved to the next position, and this process was repeated for several locations throughout the experiment hall. This scan was performed to identify hotspots of radiation throughout the room. After this initial scan was completed, a large detector array named DANG (Detector Array for measuring Neutrons and Gammas) was assembled using the same NaI detectors used in the 2 x 2 array, plus fast neutron detectors made with the commercial NE-213 liquid scintillator (equivalent to Eljen Technologies EJ-301[35]) and two 10 bar ^{3}He tubes with a 3" OD and 24" in length.

3.1.3 2 x 2 Array

The 2 x 2 array of NaI detectors pictured below (figure 3.2) was built to provide a portable means of surveying the gamma radiation throughout the experiment hall.

Figure 3.2: 2 x 2 array of NaI bricks. Detectors on a row are 40 inches apart, first row is 21.5 inches off the ground, second row is 60 inches.

3.1.4 Detector Array for Measuring Neutrons and Gammas

DANG consists of 8 NaI detectors, 8 NE-213 detectors, and 2 ^{3}He detectors. The 2 x 2 array design was improved on by providing a base to put the electronics crate and acquisition computer on, allowing the entire system to be moved to any location within the experiment hall. The height was chosen so that the top detectors are located just above the top cells of the full PROSPECT detector, but low enough to fit through the doorways leading to the back room.

Figure 3.3: DANG: Detector Array for Neutron and Gamma detection.

Note of the two ^{3}He tubes, the topmost detector is surrounded by 1" thick of high density polyethylene which is used as a neutron moderator. This was placed in order to get an idea of the fraction of neutrons that had already thermalized (kinetic energies in the meV range) by the time they reach the array.

3.2 Operating Principles of Scintillation Detectors

Scintillation materials are selected for their ability to convert ionizing interactions of charged particles passing through into visible light that can be detected using PMTs or other means of light detection[36]. These materials can be liquid, as in the case of the lithiated liquid scintillator used in the PROSPECT cells[33], or solid crystals such as the NaI(Tl) used in the HFIR background studies (see section 3.4). For inorganic scintillators such as NaI, the scintillating material has a valence band and conduction band, with an energy gap in between. As charged particles deposit their energy into the surrounding medium, the electrons get excited from the valence band into the conduction band. These electrons will then deexcite back to the valence band, emitting photons along the way.

In order to increase the number of photons emitted relative to more common energy deposition channels such as phonons, a dopant is often used. For example, thallium is commonly used in sodium-iodide crystals. This dopant adds energy levels within the band gap through which electrons excited to the conduction band can deposit their energy, lowering the energy of the resulting photons[36]. This is often done in the case of liquid scintillators in order to shift the emitted photons into larger wavelengths which can be better accepted by PMT windows. It can also be used to shift the wavelength of the emitted photons out of the self absorption range.

Materials are chosen so that the emittance spectrum of the photons is in a range transparent to the scintillating material. This minimizes the photons that get reabsorbed by the material, allowing for better light collection and hence better energy resolution. The scintillation material is encased in a material that will reflect light within this emittance spectrum, its geometry is chosen in order to maximize light collected by the detection device. A window between the detection device and the scintillation material must be chosen to minimize absorption of the scintillation light while maximizing transmittance to the detection medium.

3.3 Electronics

For all of the background measurement campaigns performed, a CAEN digitizer[37] was used as an analog to digital converter, converting the charge sensed by the PMT into a digital value. This data is then sent to an acquisition computer to be stored for further analysis.

3.3.1 Digitizers

For the P2C experiment, the CAEN Vx1720[38] was used to digitize pulses coming from the detector electronics. The Vx1720 has a 250 MHz sampling frequency with an input range of 2 Volts. The input signal can be digitized into a 12 bit integer, allowing for 4096 values to represent the voltage sensed over a given 4 ns window. Because the rates inside the P20 shield were small, the waveform of each event was recorded, allowing for subsequent analysis using C++ and python scripts.

When recording waveforms, one must set a threshold voltage that the input signal must cross in order to record the signal. Once the threshold is crossed, a user-defined timing window defines which samples are recorded to disk. For the PMTs used in the deuterated, NaI, and NE213 detectors, a microsecond long window is sufficient to capture the quick rise and subsequent falloff of the pulse for a given energy deposition event. The binary output of the digitizer is analyzed using C++ and python scripts, which finds the height, integral, rise time, arrival time, and baseline of each pulse. For the liquid scintillator detectors which can discriminate particle types based on the shape of the pulse, a short integral is also stored for each pulse so that pulse-shape discrimination (PSD) can be utilized to distinguish neutrons and gammas (see section 5.2.2 for more information on PSD analysis).

For the subsequent background scans, the Vx1730[39] was used. This digitizer has a faster sampling rate of 500 MHz, and a resolution increase of a factor of 4, using a 14 bit integer for mapping voltage input. Besides these two differences, the Vx1730 is roughly equivalent to the Vx1720. Because these background scans were done outside of a shielding package, rates in the tens of kHz were common, making storage of each waveform intractable. For this reason, CAEN's DPP-PSD firmware was utilized to perform on-board integration which allowed for the storage of each event's short and long integral along with the threshold crossing time to be stored rather than the entire waveform.

3.4 NaI Detectors

NaI is a common material used for gamma ray detection, often chosen for its large efficiency relative to other materials such as germanium[40]. Generally the sodium-iodide is doped with thallium, with increased levels of doping resulting in an increase in light output per energy deposited, until about 2000 ppm thallium, beyond which light output decreases[41].

A gamma impinging on NaI(Tl) will deposit energy via the photoelectric effect and Compton scattering[42]. The photoelectric effect causes a photon to be absorbed by an electron, exciting the electron which then loses energy via multiple scattering, brehmsstrahlung, and ionization[36]. Compton scattering is an elastic collision between electron and photon, whereby only part of the photon's energy is absorbed by the electron and subsequently deposited in the scintillator material. The outgoing photon from the Compton interaction can then produce more interactions in the material via Compton scattering or photoelectric absorption, or it can leave the detection medium, only depositing the energy it imparted onto the electron. The resulting spectrum of energy deposited from a given gamma energy will show a full absorption peak which will obey a Gaussian distribution with a width that defines the materials energy resolution along with a Compton profile that falls off at the so-called

Compton edge, which corresponds to the maximum energy imparted to the electron from a Compton scatter.

At energies larger than 1.022 MeV (twice the rest mass of the electron), pair production becomes a possibility. Pair production is defined as the process by which a photon spontaneously converts its energy into an electron positron pair. If pair production occurs within the NaI(Tl) medium, the resulting positron will quickly lose energy and annihilate with another electron in the medium, resulting in two 511 keV gammas which can subsequently either escape or be absorbed in the medium. This will result in a second peak 511 keV below the full absorption peak, known as the single escape peak, and possibly a second escape peak 1.022 MeV below the full absorption peak called the double escape peak corresponding to both 511 keV gammas escaping the detector.

The NaI(Tl) crystals used in the HFIR background studies were all manufactured by Saint-Gobain[43]. These crystals have a light output of 38,000 photons per MeV gamma interaction. Their emission spectrum peaks at 415 nm, which is suitable for many PMT windows. The primary time constant at room temperature is 250 ns. This is defined as the time in which 63% of the scintillation light has been emitted after an energy deposition event.

The 2" x 4" x 16" NaI brick detector uses an ET Technologies model 9266B[44] PMT which utilizes a bialkali photocathode sensitive to blue-green light. It is encased in a stainless-steel shell and utilizes an Ortec 276L base[45]. This is the NaI detector that most of the data used in this thesis comes from. The NaI used in P2C is a 2" OD x 2" cylindrical crystal inside an aluminum casing. It is a Bicron 2M2/2[46] model.

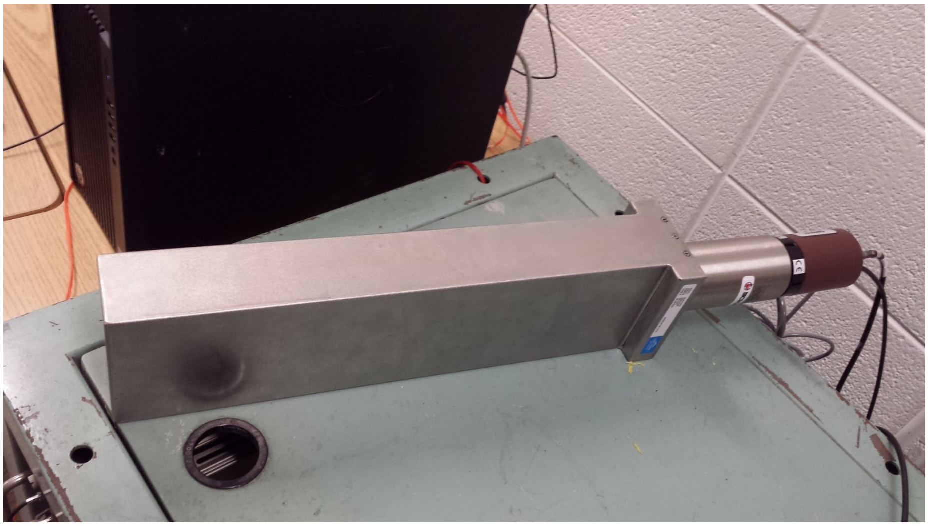

Figure 3.4: 2" x 4" x 16" NaI detector with stainless steel casing.

3.5 Neutron Detectors

Several neutron detectors have been used to provide the data for this work. The DANG array has both ^{3}He tubes and NE213 detectors which are filled with EJ-301[35]. The P2C experiment utilized two types of deuterated detectors. We will briefly go over the technical details of these detectors.

3.5.1 Deuterated Detectors

Two types of cylindrical deuterated detectors were utilized for the P2C experiment, a 2" and a 4" detector, both manufactured by Eljen Technologies. These have 103 cm^3 and 1235.5 cm^3 of active volume, filled with deuterated-benzene[34], which allows for pulse shape discrimination (PSD) between neutron and electron recoils. They have an aluminum housing coated with TiO_2-based reflective coating and a 6.3 mm Pyrex glass optical window which couples the liquid to the PMT. Both contain bialkali photocathode PMTs, with the 2" using ET Enterprises model 9807B[47] which contains a 2" diameter end window sensitive to blue-green light. The 4" detector uses an ET Enterprises model 9821B[48] which only has a 3" diameter window, creating a mismatch between the detector liquid and the PMT window which makes it have much poorer PSD capabilities than the 2" detector.

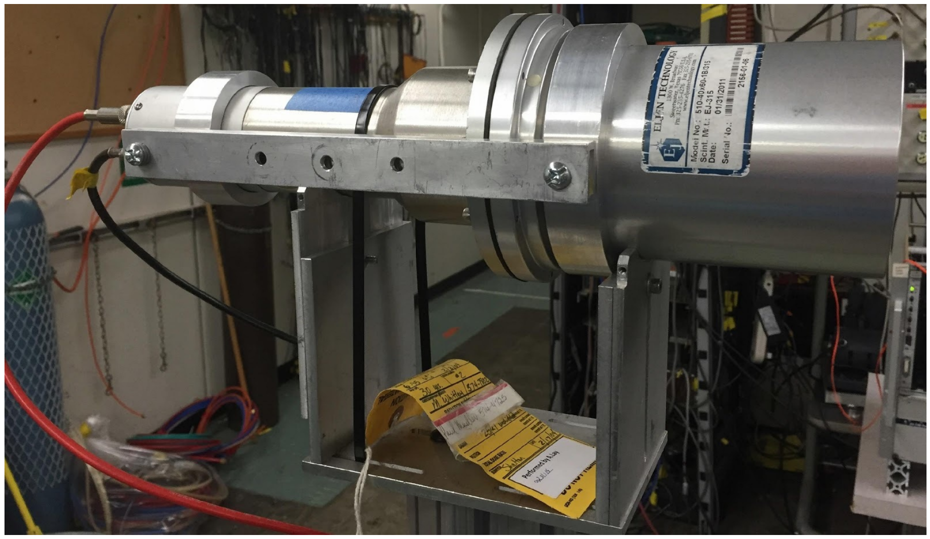

Figure 3.5: 4" Deuterated detector filled with EJ-315[34] liquid scintillator.

3.5.2 ^{3}He tubes

The 2" OD x 24" ^{3}He tubes attached to the DANG array are both filled with 10 bar of ^{3}He. The detectors mainly use the nuclear reaction ^{3}He(n,p)^{3}H (Q = 0.765 MeV)[49]. The charged reaction product will ionize the gas as it moves through the material, and a bias applied to the detector draws the electrons to be processed by the electronics. These detectors use a stainless-steel tube which acts as a cathode, with a wire attached as the anode. Charge is sent through a fast preamplifier[50] to a shaping amplifier which turns this signal from one with a very long tail (see figure 5.11) into a Gaussian, which can then be fed into the digitization electronics. These pulses last about 10 μs, which is a much longer decay time than the signals of the NaI or liquid scintillator detectors, which are a few 100 ns in width. For this reason, the ^{3}He are operated in Geiger mode, meaning that we tune the voltage threshold for triggering a count of these pulses if enough energy is deposited to exceed the typical electron noise, which means it is most likely a neutron interacting in the gas.

3.5.3 NE213

NE213 detectors are called NE213 because they are are filled a liquid called NE-213 which is the commercial equivalent of Eljen Technologies EJ301[35]. These are standard liquid scintillators used for pulse shape discrimination of fast neutrons. The exterior is an aluminum housing with a hexagonal shape. The liquid is optically coupled through a glass window to a Photonis XP4318B[51] type PMT and a VD123k[52] type voltage divider.

Chapter 4

Backgrounds for the PROSPECT Experiment

In this chapter a basic description of the PROSPECT experiment is given, including details on the segmented detector design and proposed shielding package. Then, a description of the experiment hall at HFIR is given. Finally, measured neutron and gamma background data taken in the experiment hall is shown.

4.1 Motivation

Due to the recently uncovered shape and rate anomalies (see section 2.2), a number of next generation antineutrino measurements [53] [54] [55] are underway to pinpoint the source of these anomalies. At Oak Ridge National Laboratory's High Flux Isotope Reactor (HFIR), the PROSPECT (Precision Reactor Oscillation and Spectrum) [1] experiment is underway working to deploy 3.7 tons of lithiated liquid scintillator to obtain a high resolution (4.5% energy resolution at 1 MeV) measurement of the antineutrino spectrum. PROSPECT is designed to probe the best-fit region of the mixing parameters for a 1eV-scale sterile neutrino independent of knowledge of the exact shape of the reactor spectra utilizing a movable detector which can measure the spectra between 7 and 12 meters from HFIR's core. In addition to probing a portion of the sterile neutrino model space, PROPECT's high resolution measurement of the antineutrino spectrum can give insights into the shape discrepancies found at commercial reactors (see section 2.2). This is because HFIR is a Highly Enriched Uranium (HEU) reactor, which means that a significant fraction (>99%) of the fissioning nuclei is ^{235}U. This measurement will allow for a direct comparison to theoretical calculations of the ^{235}U spectrum. In contrast, commercial reactors generally have some fuel mixture of ^{239}Pu, ^{241}Pu, ^{235}U, and ^{238}U which leads to uncertainty in the source of discrepancies between spectral shape calculations and measurements.

4.2 Detector Design

PROSPECT is a phased experiment, with the first phase set to begin assembly in 2017. The PROSPECT phase I antineutrino detector (AD-1) will consist of an 11x14 array of optically segmented lithiated liquid scintillator (LiLS) cells, with the active volume spanning a 63" x 46" x 80" volume (see figure 4.1). The phase II detector will be constructed if evidence for sterile neutrinos are found and interest exists to invest in an additional, larger detector constructed at about 20 meters from the reactor core. This work will focus on the AD-1 design.

For light collection, a PMT will be optically coupled to both ends of every cell, with a Winston cone coupler connecting the cell end and the PMT face. The passive shield surrounding the active detector volume as pictured in figure 4.2 will consist of waterbricks[56] on top for attenuating high energy neutrons from cosmic ray interactions in the atmosphere and lead and polyethylene shielding for attenuating reactor-correlated gammas and neutrons. The inner layer of shielding contains borated polyethylene which serves as a thermal neutron absorber, and it is placed on the inside in order to absorb neutrons that are emitted from gamma interactions in the shielding. In addition to the passive shield, a local shield wall of lead bricks (see figure 4.1) will be built alongside the wall adjacent to the reactor room, which will serve to attenuate the hottest source of gammas in the experiment room.

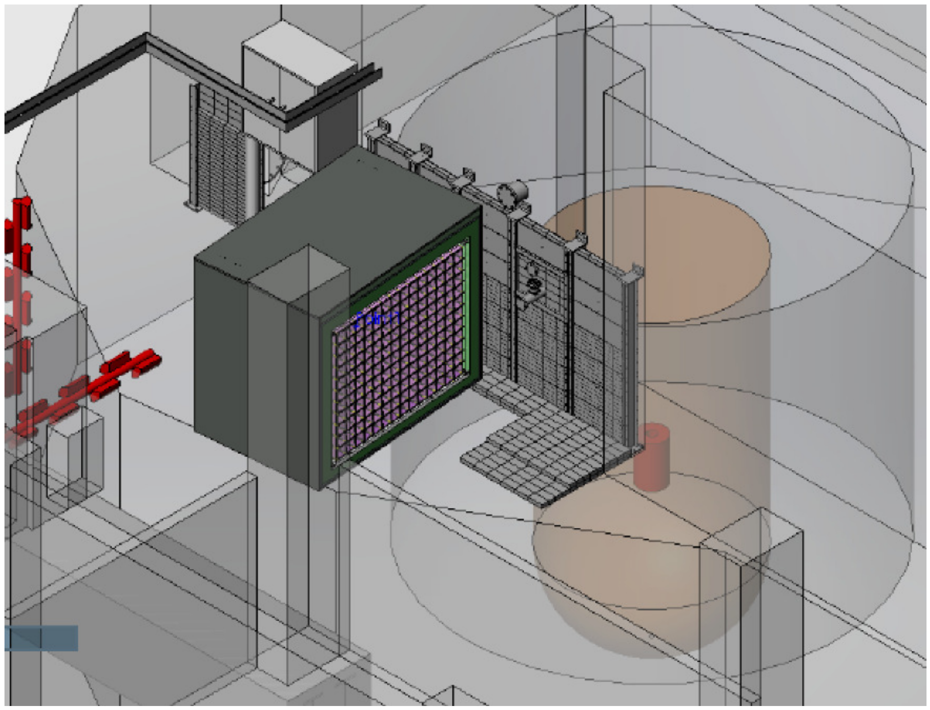

Figure 4.1: Proposed location for PROSPECT Detector inside passive shield next to local shield wall. One story below in the adjacent room lies the reactor core (red cylinder)[1].

The design takes into account constraints from HFIR for floor loading and ceiling clearance. Additionally, with movable air pallets the detector can be moved to an intermediate and a far position, allowing a scan of baselines ranging from 7m to 12m from the reactor core. This range of baselines will extend the detector's sensitivity for probing the sterile neutrino hypothesis as pictured in figure A.2.

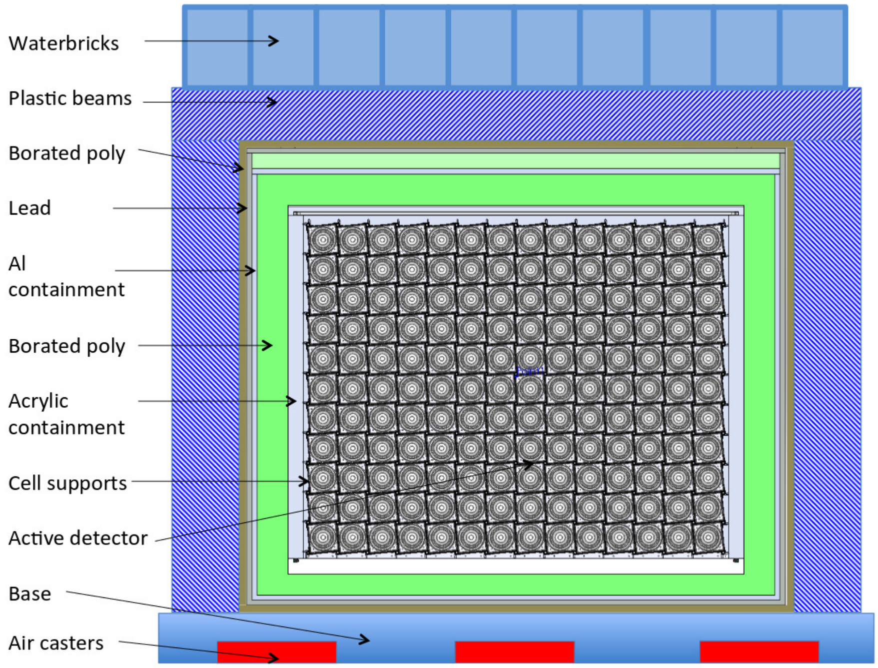

Figure 4.2: Schematic of AD-1 design plus surrounding passive shield. Shown is the cross section of an 11x14 matrix of optically separated cells each approximately 16.9 cm x 16.9 cm. Into the page the cells extend 120 cm[1].

4.2.1 Inverse Beta Decay Detection

The base liquid scintillator being used is EJ-309, a commercially available scintillator from Eljen Technologies[57]. This was selected for its ability to discriminate neutrons and gammas using the shape of the detected pulse (see section 5.2.2 for more details). EJ-309 was specifically chosen over EJ-301 which provides a better pulse shape discrimination because of its high flash-point, which is required by the environmental safety standards of the HFIR facility. Wavelength shifters (bis-MSB) and fluors (PPO) are added to the commercial base along with enriched ^{6}Li which provides a neutron capture signal via the reaction

$$^6Li + n \Rightarrow \alpha(2.73 \text{ MeV}) + t(2.05 \text{ MeV}).^{[58]} \tag{4.1}$$

The light produced from the resulting triton and alpha particles ends up in the neutron band between 0.5 MeV_{ee} and 0.75 MeV_{ee} (see figure 4.3), allowing for a gate on neutron captures.

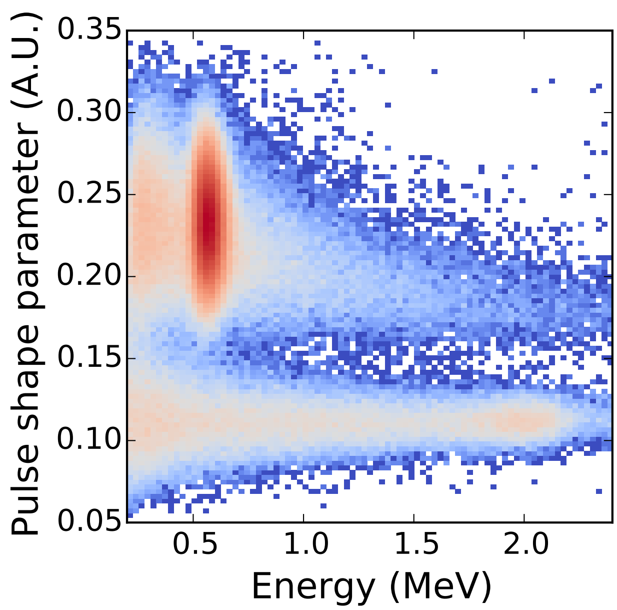

Figure 4.3: LiLS pulse shape discrimination for a 20-liter test cell irradiated with ^{252}Cf to provide neutron captures and recoils. The lower band corresponds to gamma recoils[1].

The EJ-309 base has a high proton density which makes it ideal for IBD reactions. The outgoing positron from the IBD will produce light from energy deposition in the liquid followed by its annihilation with an electron, from which the outgoing 511 keV gammas can also be detected. This is called the prompt signal, and is detected nanoseconds after the IBD occurs. The neutron will thermalize before being captured, which happens on average $\sim$40 μs after the prompt signal, so it is called the delay signal. This requirement for a neutron signal within a $\sim$100 μs window after a positron-like signal allows for strong rejection of accidental backgrounds due to coincidence events.

4.3 Description of HFIR

The High Flux Isotope Reactor located at Oak Ridge National Lab[2] is an HEU reactor which means that most of the fissioning nuclei consist of ^{235}U. The core is compact compared to commercial reactors, with a diameter of 15 inches. The typical operating thermal power is 85 MW, and the core configuration consists of fuel elements made from U_3O_8 dispersed in Al with burnable ^{10}B used as reactor poison[3]. A beryllium neutron reflector surrounds the fuel rods. Control rods which consist of tantalum, aluminum and europium are used to absorb neutrons controlling the thermal power.

The reactor-on cycle typically lasts 21 days, after which the reactor is shutdown for a similarly long period which is used for refueling. This fuel cycle is chosen to minimize the amount of plutonium buildup in the core which makes it an ideal case for studying ^{235}U fission. The reactor-off periods also allow for background studies that separate the constant IBD-like backgrounds from the signal, specifically radioactive contaminants within the detector and cosmic radiation.

The near location is located in the experiment hall at HFIR which at its closest is 7 meters from the core, situated one building level above and one room over from the core. Extending to the back of the experiment hall allows a baseline of 12 meters. This experiment hall is pictured below in a schematic showing HFIR's core in relation to the region of the PROSPECT detector, with two of HFIR's beamlines (HB-3 + HB-3A and HB4) pictured in the background, both situated below the experiment hall. The box pictured is where the P20 shield was situated, and is approximately the same position of the full detector front position (see figure 4.4).

Beamline HB4 is the cold neutron beamline; because it is the longest beamline and its geometry directly below the experiment hall is kept relatively constant, HB4's operation is not expected to produce changes in radiation in the experiment hall that PROSPECT will be sensitive to. HB3 and HB3-A, on the other hand, have large

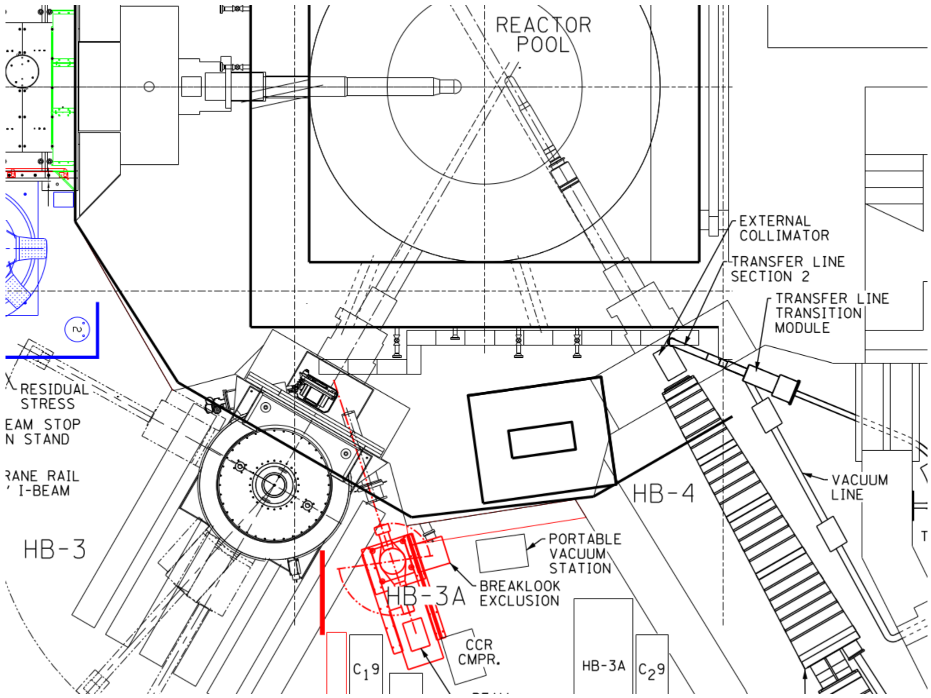

Figure 4.4: Schematic of the experiment hall plus P20 shield with reactor core and two beamlines (HB3 + HB3-A and HB4) superimposed in the background. Bold lines indicate the outline of the concrete monolith which surrounds the core. P20 sits atop the monolith.

spectrometers situated only a few meters away from the PROSPECT detector in the floor below, and thus produces measurable changes in the gamma and neutron backgrounds. Rate history and beamline activity correlations are discussed more in 4.5.3.

4.4 Backgrounds for the Experiment

Based on measurements taken with P20, cosmic backgrounds are the dominant IBD-like signal as has been seen in the 20-liter prototype used at HFIR. Calculations based on expected levels of contaminants within the scintillator such as the Uranium and Thorium decay chain shows that internal radioactivity produces IBD-like signals at a rate that is an order of magnitude lower than the expected true IBD signal[1].

4.4.1 Cosmic Backgrounds

Cuts on IBD-like signals in a 20-liter test cell at HFIR show statistically insignificant difference between reactor-on and reactor-off backgrounds (see figure 4.5). This indicates that the reactor-correlated neutron and gamma backgrounds are insignificant after attenuation from the prototype shielding package and cuts on prompt and delay signals.

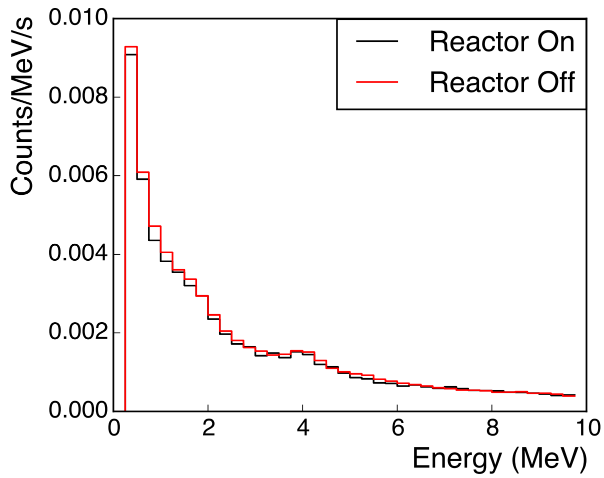

Figure 4.5: IBD-like backgrounds taken from a 20-liter test cell at HFIR, reactor-on in black, reactor-off in red[1].

Neutrons formed from cosmic ray showers can have energies up to 100 MeV, which is enough to punch through HFIR's overburden and the detector shield, creating showers of particles along the way which will interact in the detector. Secondary neutrons created from spallation can provide the delay signal after capturing in the scintillator, while gammas from the neutron interactions around the detector can provide the prompt signal[1]. These processes are well captured in a Geant4[59] simulation (see figure 4.6) of the prototype detector using LLNL's CRY generator for generating cosmic ray events[60].

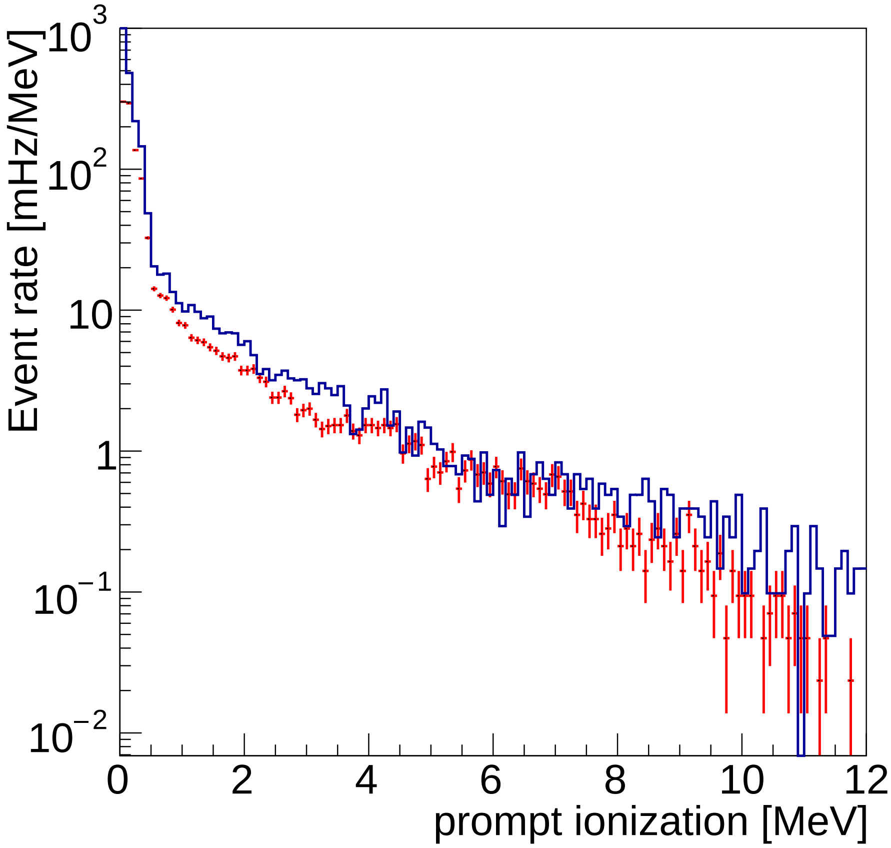

Figure 4.6: IBD-like backgrounds taken from a 20-liter test cell at HFIR during reactor-off. Data in red, simulation in blue[1].

4.4.2 Reactor Backgrounds

While the reactor backgrounds from the 20-liter prototype contributed a negligible amount of IBD-like background, they are still important to understand for the full experiment. The full experiment is planned to use less lead shielding on the sides of the detector relative to the prototype in order to maximize the active volume of the detector within the cost and weight constraints of the experiment. This means that impact from accidental coincidences with gammas from the reactor could be larger than in the prototype experiment. Additionally, spacial and time variations of the reactor-on background environment need to be taken into account for doing proper background subtraction for IBD candidate events, and given that the IBD signal is always present with the reactor correlated backgrounds, an independent measurement of the backgrounds insensitive to IBD events is required for proper simulation of the reactor-correlated IBD backgrounds.

The fissioning ^{235}U within HFIR's core will generally split into individual neutrons and two neutron rich fragments, which will then decay via beta decay or beta-delayed neutron decay. This means that in addition to photons and neutrinos escaping the core from the decaying nuclei there will also be a spectrum of neutrons escaping. Due to the large amount of material (mostly concrete) in between the core and the experiment hall, the neutrons have mostly thermalized (energies in the meV range). Due to boron's large neutron capture cross section, the borated polyethylene located at the inner layer of the PROSPECT passive shield (figure 4.2) will absorb the majority of thermal neutrons. Thus, the main reactor-correlated background that can cause IBD-like signals are gammas from neutron capture in materials around the detector. The gammas from the core which come from beta decaying nuclei and neutron capture on core components are largely attenuated by the intermediate concrete material, so provide a second order component to the reactor-correlated gamma spectrum seen by PROSPECT.

In addition to neutron activated material surrounding the experiment hall, there is also background from nearby experiments. The most prominent is a transport line that runs argon gas near the reactor core in order to cool an irradiation target, and circulates it back through the experiment hall about 4 meters above the floor down to a sampling complex located a couple of meters from where the PROSPECT detector will sit. This complex is called the Materials Irradiation Facility (MIF) [61], and while the experiment is running, gamma backgrounds from 0 to 1.294 MeV can increase as much as 100% depending on the location of measurement within the experiment hall. This is due to ^{41}Ar beta decaying as it is transported through the experiment hall. ^{41}Ar has a strong gamma line at 1.294 MeV. The MIF experiment is not set to run during the initial data taking for the full PROSPECT experiment, however it is possible that an experiment will be done at some reactor-on cycle coinciding with PROSPECT operation, and is important to characterize its effects on the backgrounds of the detector. Analysis and simulation of the MIF radiation is detailed in section 6.2.1. A gamma spectrum taken with a 2" x 4" x 16" NaI detector during a reactor-off period and during a reactor-on period with the MIF running is shown in figure 4.7.

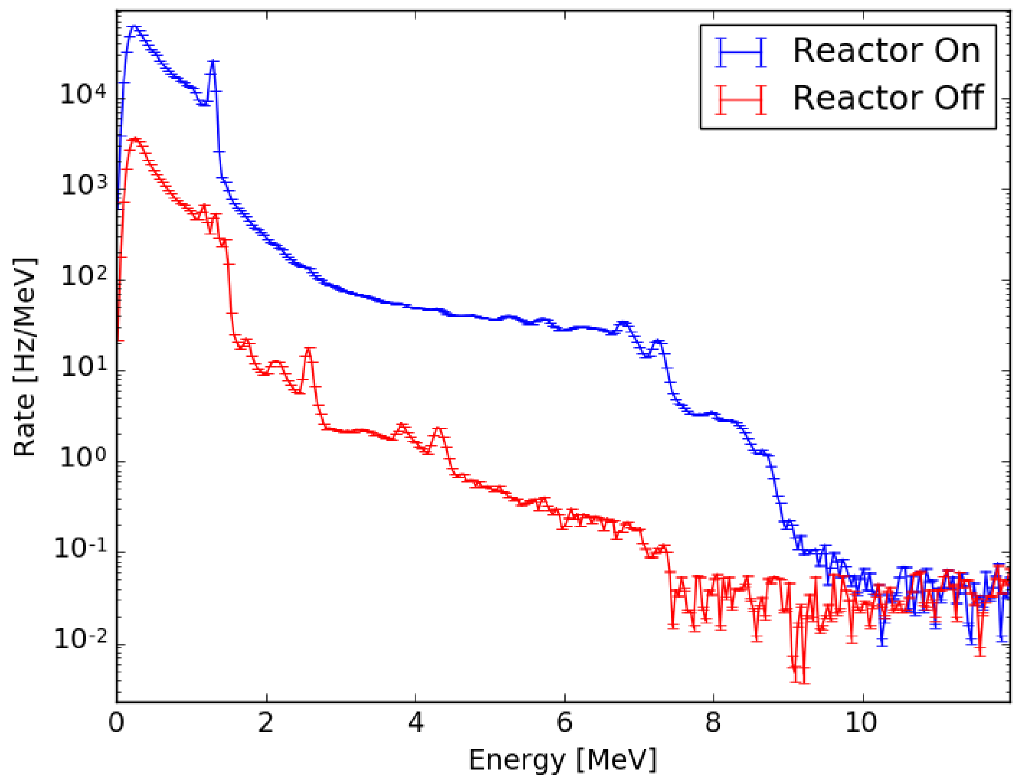

Figure 4.7: Calibrated gamma spectra taken with 2"x4"x16" NaI detector, one during a reactor-on cycle (blue) and one when the reactor was off (red). Error bars are from counting statistics for 40 keV bins. Photopeaks at 0.511 MeV from positron annihilation and 1.29 Mev from ^{41}Ar are visible in the reactor-on spectrum, along with several neutron capture gammas at higher energies. Photopeaks at 1.17 MeV and 1.33 MeV in the reactor-off spectra are from ^{60}Co from the neutron activation of ^{59}Co (stable). Other reactor-off features are typical room backgrounds, with a 1.46 MeV peak from ^{40}K, 2.61 MeV and 2.10 MeV from ^{208}Tl (photopeak and escape peak), and 1.76 MeV photopeak from ^{214}Bi.

In order to to characterize the gamma and neutron backgrounds, a number of different detector technologies including sodium-iodide and cerium-bromide for gammas, NE213 and EJ-315 for fast-neutrons, and ^{3}He for thermal neutrons was used. Here we refer the reader to chapter 3 for more information on these detectors and the electronics deployed for the background measurements.

4.5 Background Data

Data was obtained from a number of different campaigns for measuring the spacial and temporal variation of the gamma and neutron field throughout the experiment hall in order to understand the source of various background components when the reactor is both off and on. Knowledge of the temporal fluctuations in backgrounds due to changes in beamline operation below the experiment hall can be used to inform the "worst-case scenario" for gamma backgrounds that PROSPECT will be exposed to. Additionally, the knowledge of spacial backgrounds will inform the design of the local shield wall which will serve to attenuate the hot-spots measured throughout the proposed PROSPECT locations. This section will describe the data taken to understand these backgrounds, including data taken for an experiment named P2C, data taken with our 2 x 2 array of 2" x 4" x 16" NaI detectors, and data taken with DANG.

P2C was a campaign taken after the removal of P20 from its shielding package in July of 2015, in which a ^{3}He, a NaI, and two deuterated liquid scintillators (EJ-315) were placed inside the existing shielding package, along with an old 2-liter prototype cell. The purpose was to study the fluctuations in background over time with detectors that specialize in measuring gammas (NaI), fast neutrons (deuterated), and thermal neutrons (^{3}He). In addition, identical ^{3}He, NaI, and deuterated detectors were used in scans outside the prototype shielding to understand the shielding attenuation factor along with spacial variations around the detector setup. This data is presented in section 4.5.1.

A second campaign to understand the variation in backgrounds throughout the experiment hall was performed with a portable 2 x 2 array of 12" x 2" x 4" sodium-iodide detectors (see section 3.1.3 for more details). Most recently a larger array called DANG (see section 3.1.4) consisting of sodium iodide, NE-231, and ^{3}He tubes was built and deployed to measure the spacial variance of fast neutrons, gammas, and thermal neutrons throughout the volume of the future PROSPECT detector. Spacial variance in gamma and neutron rates is presented in section 4.5.2, while timing variation from these setups is contained in section 4.5.3.

4.5.1 P2C Data

After the 20 liter experiment (henceforth P20) was completed[1], the 20 liter cell was removed from its shielding package (see figure 3.1) and replaced with a 2" NaI detector, a 2" and 4" deuterated liquid detector, and a ^{3}He tube. More information about this setup can be viewed in section 3.1.1. The NaI detector was in a stable running mode for a 6 month period and a rate history can be seen below (figure 4.8). Additionally, the 2" deuterated detector provided good neutron discrimination and an analogous rate history for neutrons detected can be seen in figure 4.9.

These time series show that the gamma rates from 1 to 3 MeV inside the shielding package increase by 40% during periods where the reactor is on. In contrast, fast neutron rates from 0.2 MeVee to 10.0 MeVee are roughly constant between reactor-on and off cycles, with the exception of some spikes in rate that appear independent of reactor status. We know the spike in December is due to noise introduced in the electronics from scans with external connected to the DAQ. It is possible that the other spikes are due to noise, but we do not know for sure and thus further investigation of this phenomenon is required.

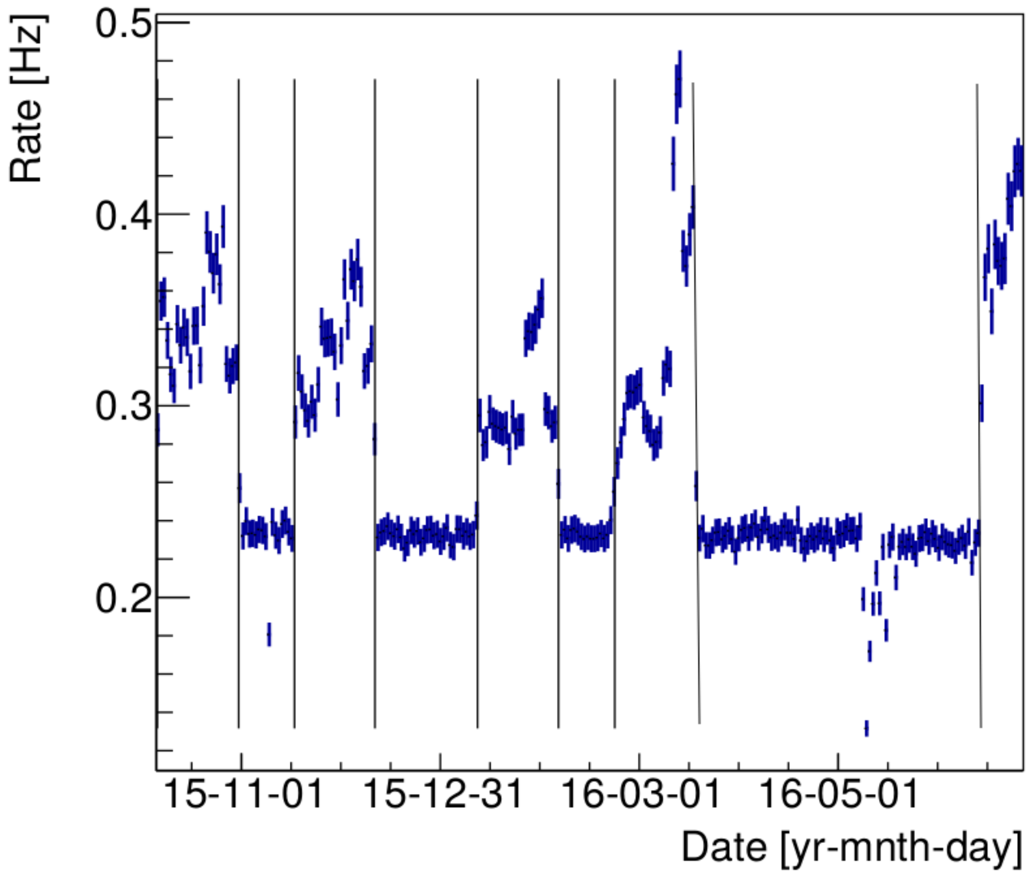

Figure 4.8: NaI gamma rates for energy depositions between 1 and 3 MeV for 2" detector inside P20 shielding over a 6 month period. Rates are binned in 24 hour increments. Black lines correspond to times that reactor is at 10% thermal power. Increases in rate at the end of the March cycle are due to testing of the MIF line. The MIF experiment started officially during the June cycle which accounts for the increase in rate during those times. Note the dip in rate during the last reactor-off cycle is due to problems with the DAQ and is not a real drop in rate.

In addition to long term trends, comparisons were done with identical 2" NaI and deuterated detectors which were deployed outside the shielding package while their counterparts inside the shield were taking data. A multiday run with detectors inside and outside the shielding (for both reactor-on and reactor-off) was done to understand the impact that the shielding has on gamma and neutron rates. This can be viewed in figures 4.10 and 4.11.

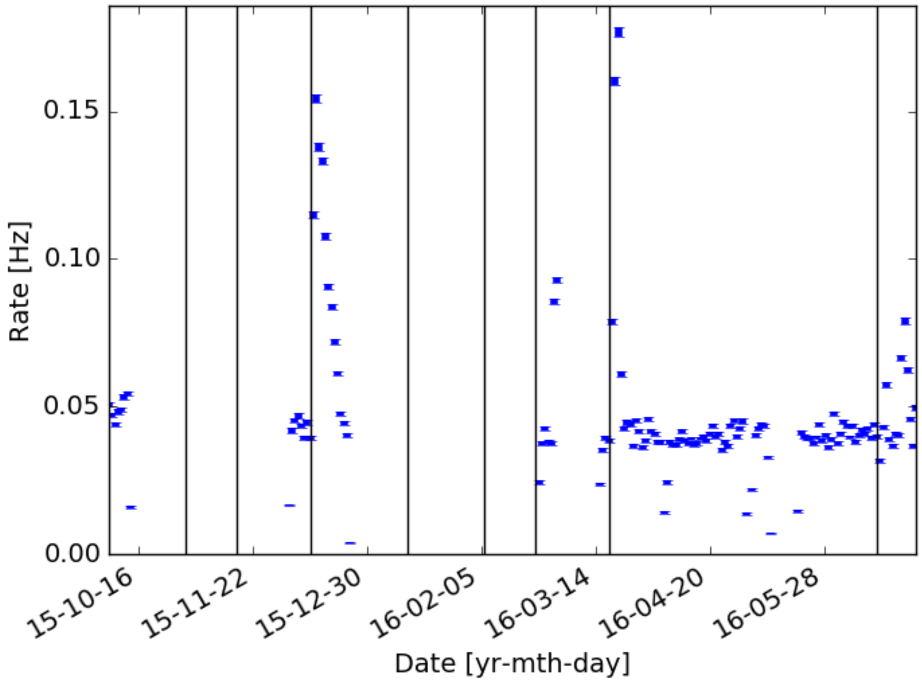

Figure 4.9: Deuterated detector singles rates for neutron-like energy depositions between 0.2 and 10 MeVee for 2" detector inside P20 shielding over a 6 month period. Black lines correspond to the times that reactor is at 10% thermal power. The first period shown is a reactor on cycle. Note periods with no rate are due to times when no data was taken for these detectors. Decreases in rate during the May reactor off cycle are due to data outages. Spike in rate during late December is due to noise shifting the gamma PSD into the neutron PSD band. Further investigation is required to see if other rate spikes are due to noise or if they are real events.

In addition to long term trends and shielding comparisons, scans at different positions outside the shielding package with identical 2" detectors (NaI and deuterated) were done in order to understand the spacial variation of neutron and gamma rates around the detector region. The result of these scans can be found in figures 4.12 and 4.13.

These results disagreed with our initial expectations, which was that the rates should decrease as one moves further from the reactor. The reason this is not the case is because of the beamlines that extend from the reactor core, and the various drainage pipes in between the experiment hall and the reactor core. In order to

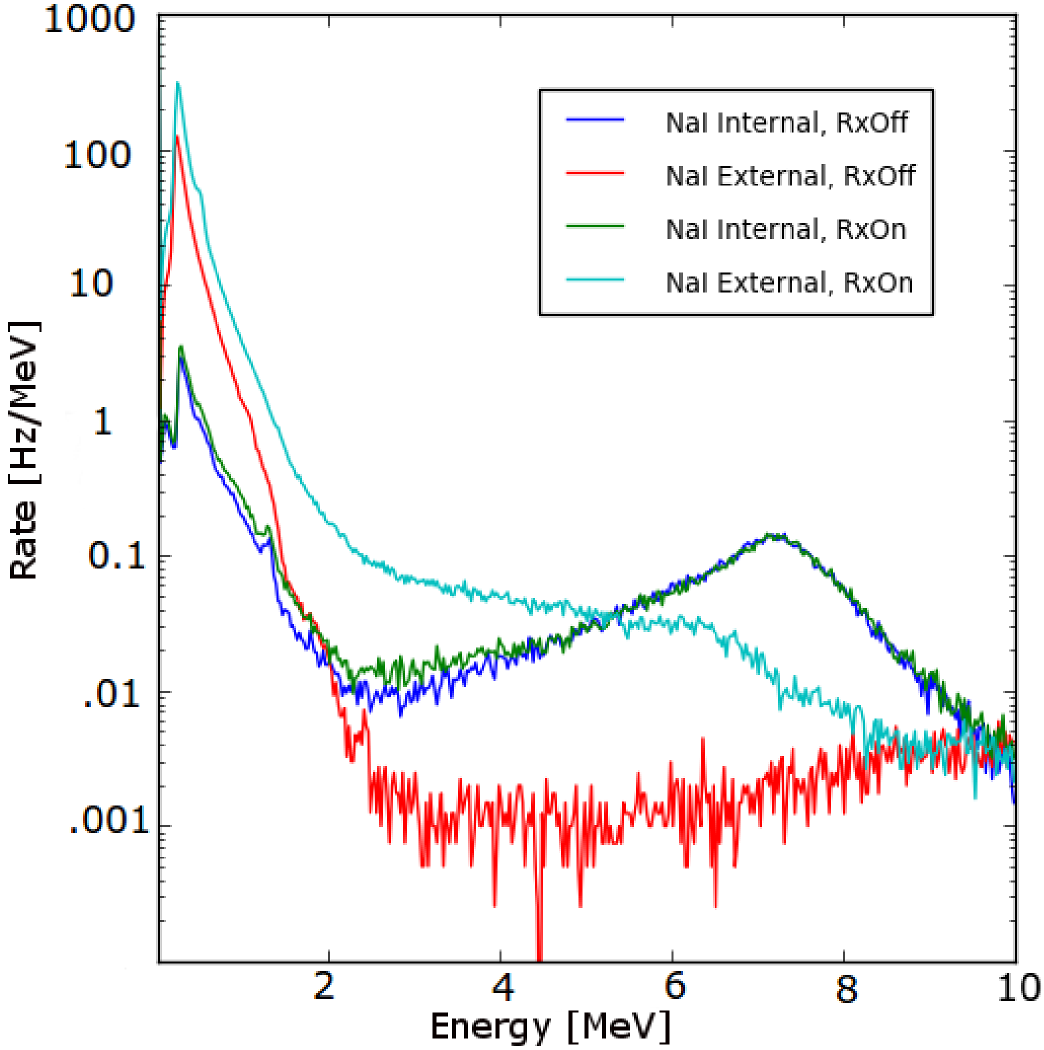

Figure 4.10: NaI gamma energy spectrum for both inside and outside detectors, reactor-on and off. Note the increase in radiation inside the the shielding above 2 MeV during reactor-off is due to interactions in the shielding with cosmic radiation. This component due to cosmics interacting in the shielding materials is roughly the same during reactor-on because cosmic radiation is independent of reactor operation.

better understand this spacial variation, several additional scans using NaI detectors were completed and are detailed in the following section.

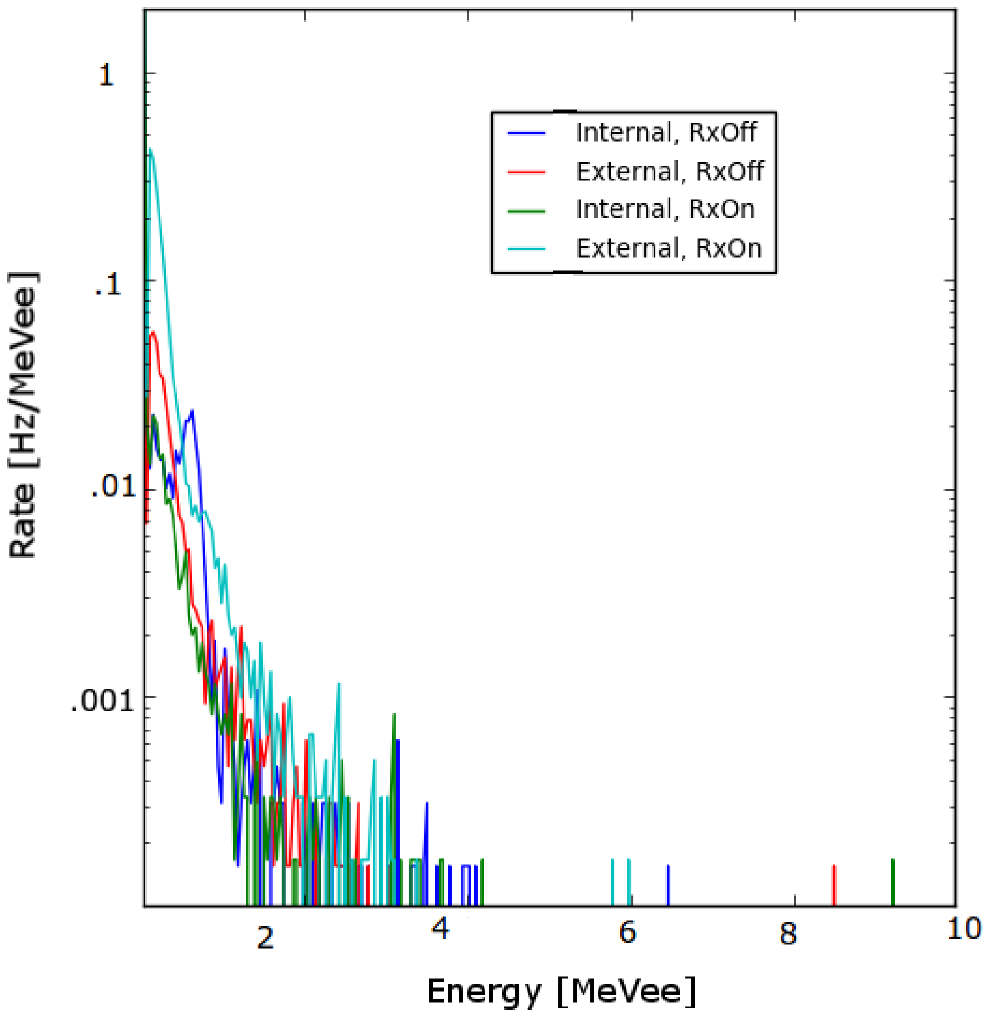

Figure 4.11: Deuterated neutron gated singles energy spectrum for both inside and outside detectors, reactor-on and off. Note the internal reactor off spectra has an artificial bump around 1 MeVee due to noise causing gamma recoils to bleed into the neutron band.

4.5.2 Room Scans with Background Monitors

A room scan was performed with a 2 x 2 array of 2" x 4" x 16" NaI detectors (see section 3.1.3). To visualize this, a bubble plot shown in figure 4.14 depicts gamma rates detected between 1 and 3 MeV at different positions throughout the room, overlayed on a blueprint of the experiment hall along with beamlines and reactor core below.

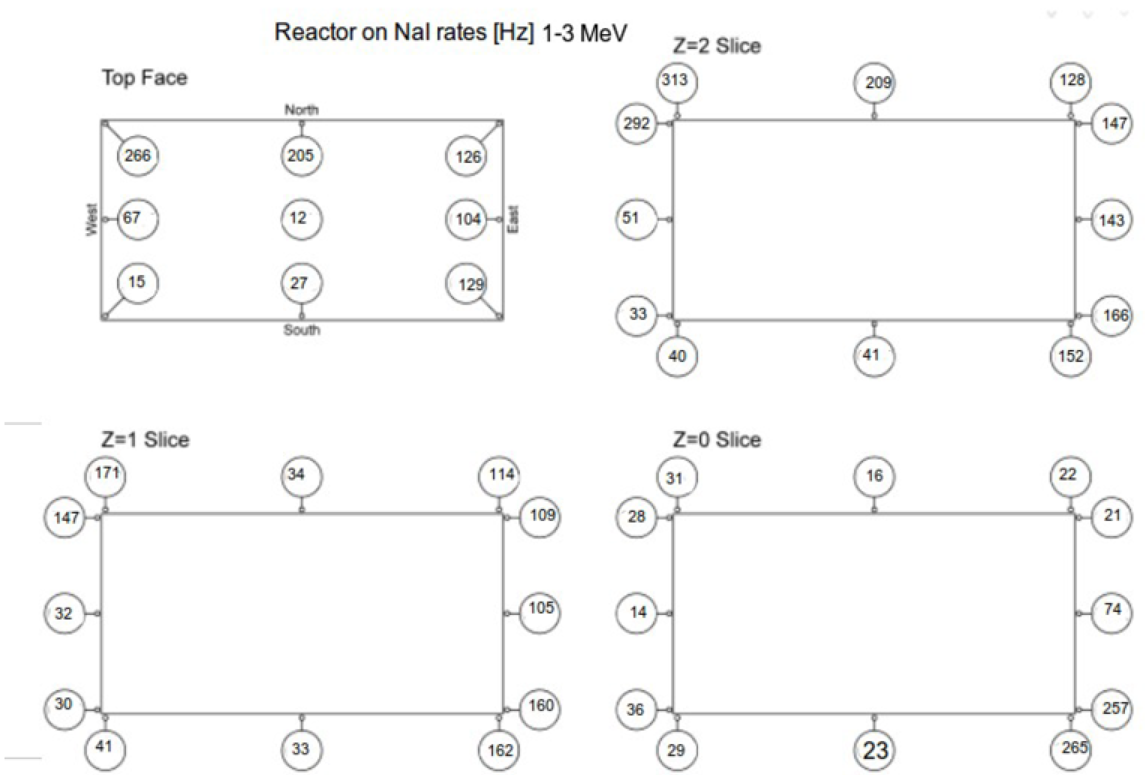

Figure 4.12: 2" NaI singles rates (Hz) for energy depositions between 1 and 3 MeV at different positions around the P20 shield during reactor-on. Cross sections at different heights are shown, Z = 0, 1, 2 corresponding to 0", 30", and 60" above the floor respectively.

Looking at rates between 1 and 3 MeV makes it easy to see the falloff due to the MIF argon line as one moves away from that source of radiation. This, however, makes it difficult to see what the background profile looks like from other sources throughout the room. A cut on energy from 3 to 5 MeV solves this problem, as ^{41}Ar emits gamma radiation only up to 1.29 MeV. This figure is shown in figure 4.15. Here we can see that there is a hot spot in radiation near the reactor wall where the MIF line connects. This hot spot is due to a drainage pipe in the floor that is located in that vicinity, giving neutron activated gammas less material to pass through before reaching the experiment hall. Other notable features are the increase in rate over beamline HB-4, which is due to neutron activated materials around the cold neutron beam.

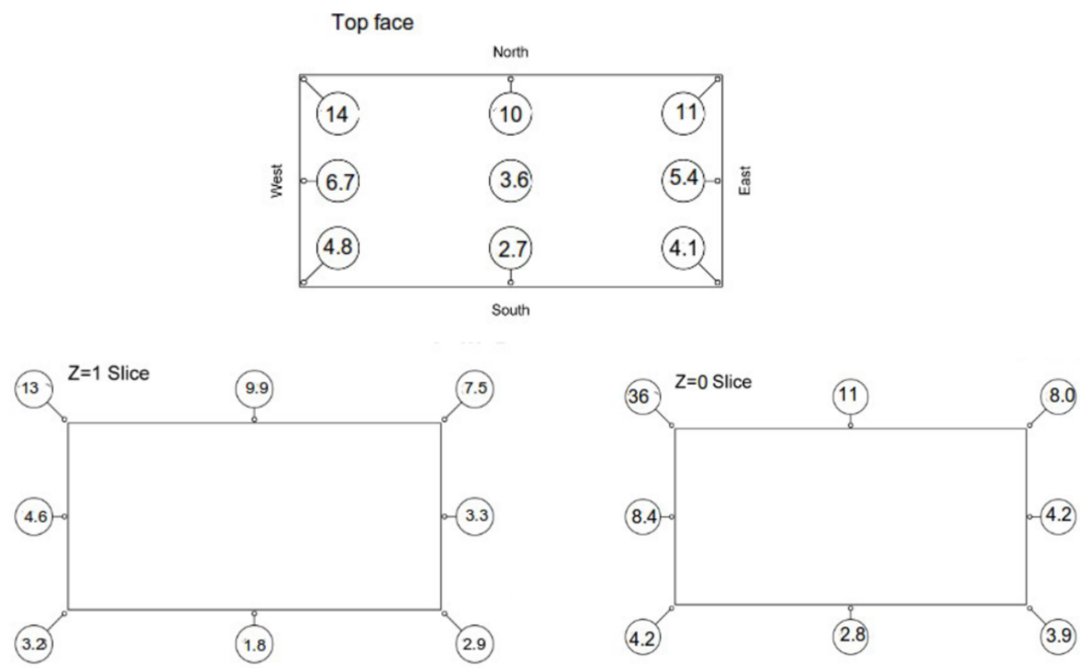

Figure 4.13: 2" NaI singles rates (Hz) for energy depositions between 1 and 3 MeV at different positions around the P20 shield during reactor-off.

After the 2 x 2 array was used for position scans, DANG was deployed for similar positions scans. Specifically, it was deployed within the volume of the future PROSPECT locations, both near (7 meters from reactor core) and far (12 meters from reactor core). A table summarizing results of this scan for reactor-on measurements can be viewed in table 4.1, and a figure to visualize the results is seen below in figure 4.16. Similarly, a table summarizing the reactor-off measurements can be found in Table 4.2. Additional position scan plots including reactor-off versions can be found in the appendix section B.

Table 4.1: Reactor-on Position Scan Gamma Rates (low, average, high)

Height [cm]	Front Position Rates [kHz]	Back Position Rates [kHz]
11	10.1, 15.5, 25.4	3.2, 5.5, 10.0
33	12.7, 19.5, 31.2	4.0, 6.8, 13.9
55	12.3, 20.5, 34.0	3.8, 6.7, 13.0
81	13.5, 21.5, 31.7	4.9, 7.3, 12.5

Table 4.2: Reactor-Off Position Scan Gamma Rates (low, average, high)

Height [cm]	Front Position Rates [kHz]	Back Position Rates [kHz]
11	0.62, 1.10, 3.10	0.11, 0.33, 0.49
33	0.71, 1.20, 3.50	0.13, 0.35, 0.51
55	0.62, 1.10, 1.90	0.06, 0.32, 0.53
81	0.59, 1.26, 2.70	0.16, 0.44, 0.59

For thermal neutrons during reactor-on we measured fluxes in the front position ranging from 0.08 to 0.11 Hz/cm^2 for the moderated detector and 0.15 to 0.25 Hz/cm^2 for the unmoderated detector. In the back position we found fluxes of 0.03 to 0.05 Hz/cm^2 for the moderated and 0.10 to 0.18 Hz/cm^2 for the unmoderated. This tells us that most of the neutrons entering the experiment room have thermalized because the unmoderated tends to show a higher rate during reactor-on. To visualize this, see figure 4.17. When the reactor is off, most neutrons are coming from cosmics and we see fluxes of 0.001 to 0.003 Hz/cm^2 for both unmoderated and moderated in the front position and only a slightly smaller 0.0001 to 0.002 Hz/cm^2 in the back position. The reactor-off plot thermal neutron position scan plot can be found in the appendix in figure B.4.

4.5.3 Rate Histories: Reactor-On Cycle and Reactor Shutdown Data

In addition to the spacial variation of the reactor correlated backgrounds, we would like to understand the variance throughout the duration of the reactor-on cycle. Beamline activities and reactor operation can both change background levels as has been seen in figure 4.8. Do we find similar patterns measuring gammas outside any shielding as we did inside the P20 shielding? It turns out that we do see periodic increases and decreases of gamma rates and thermal neutron rates as the reactor cycle progresses, as can be seen in figure 4.18.

More work is required to better correlate changes in rate with beamline activities, but an initial investigation finds correlations between the start and end of some HB-3 experiments and the timing of rate increases in the higher energy bins (2+ MeV). This is most likely due to beamline settings of HB-3 affecting the amount of neutrons scattered upwards toward the experiment hall, thus changing the rates of neutron capture gammas seen. This is corroborated by rates measured in our ^{3}He tubes which are sensitive to thermal neutrons (see figure 4.19). Fast neutron rates seem to be less sensitive to beamline operation, but we do find an increase between reactor-off where most fast neutrons are coming from cosmics, and reactor-on (see figure 4.20).

In addition to correlations with beamline activities, we also identified correlations with reactor operation, specifically the defueling after that occurs shortly after a reactor shutdown. This can be viewed in figure 4.21.

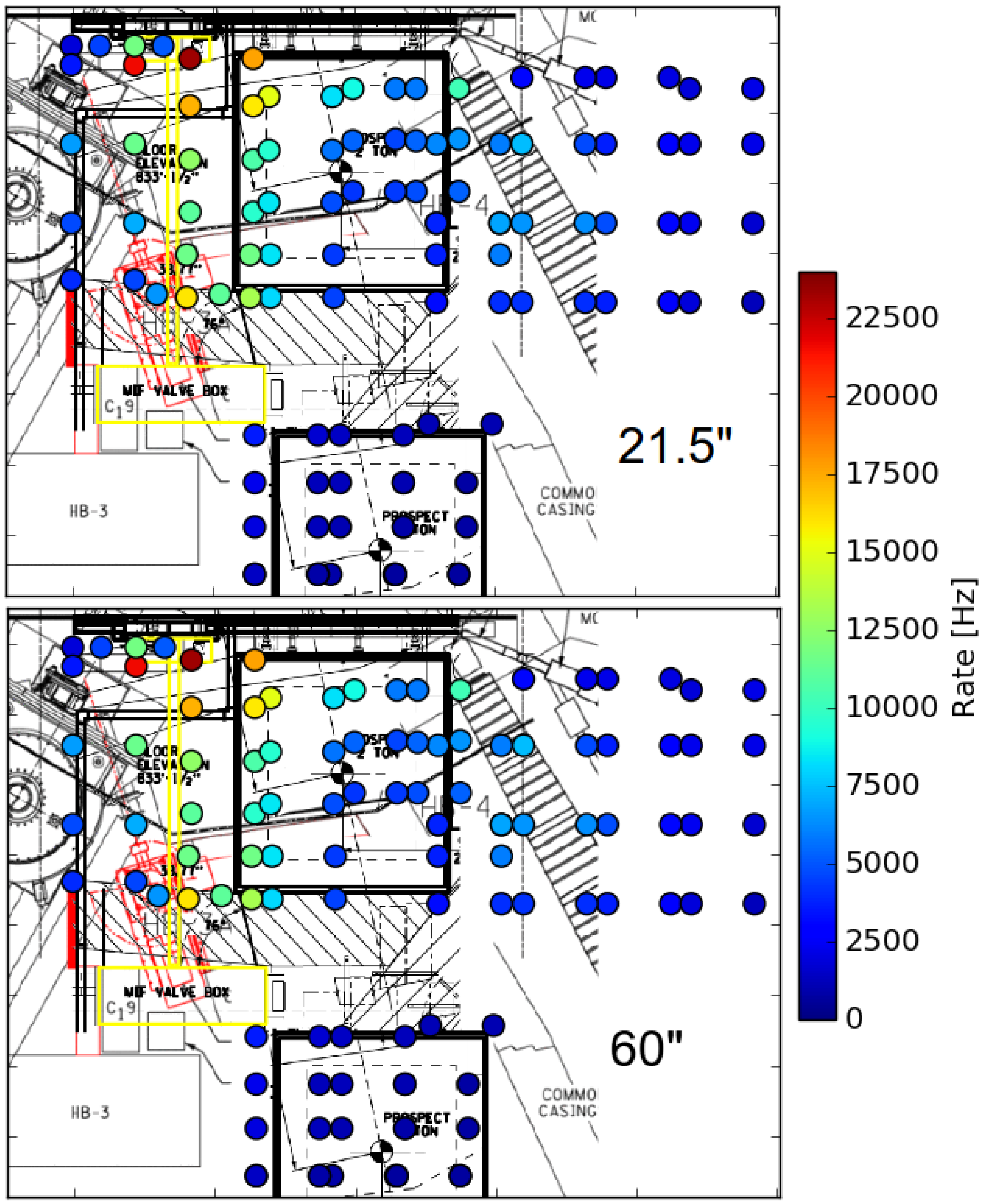

Figure 4.14: 2" x 4" x 16" NaI gamma rates (Hz) for energy depositions between 1 and 3 MeV at different positions throughout the experiment hall during reactor-on, top figure taken at 21.5" above the floor, bottom at 60". Rate bubbles are overlayed on a blueprint of the experiment hall, with the uppermost box corresponding to PROSPECT's near position, the lower box corresponding to the far position. If pictured, the reactor core would appear above the page.

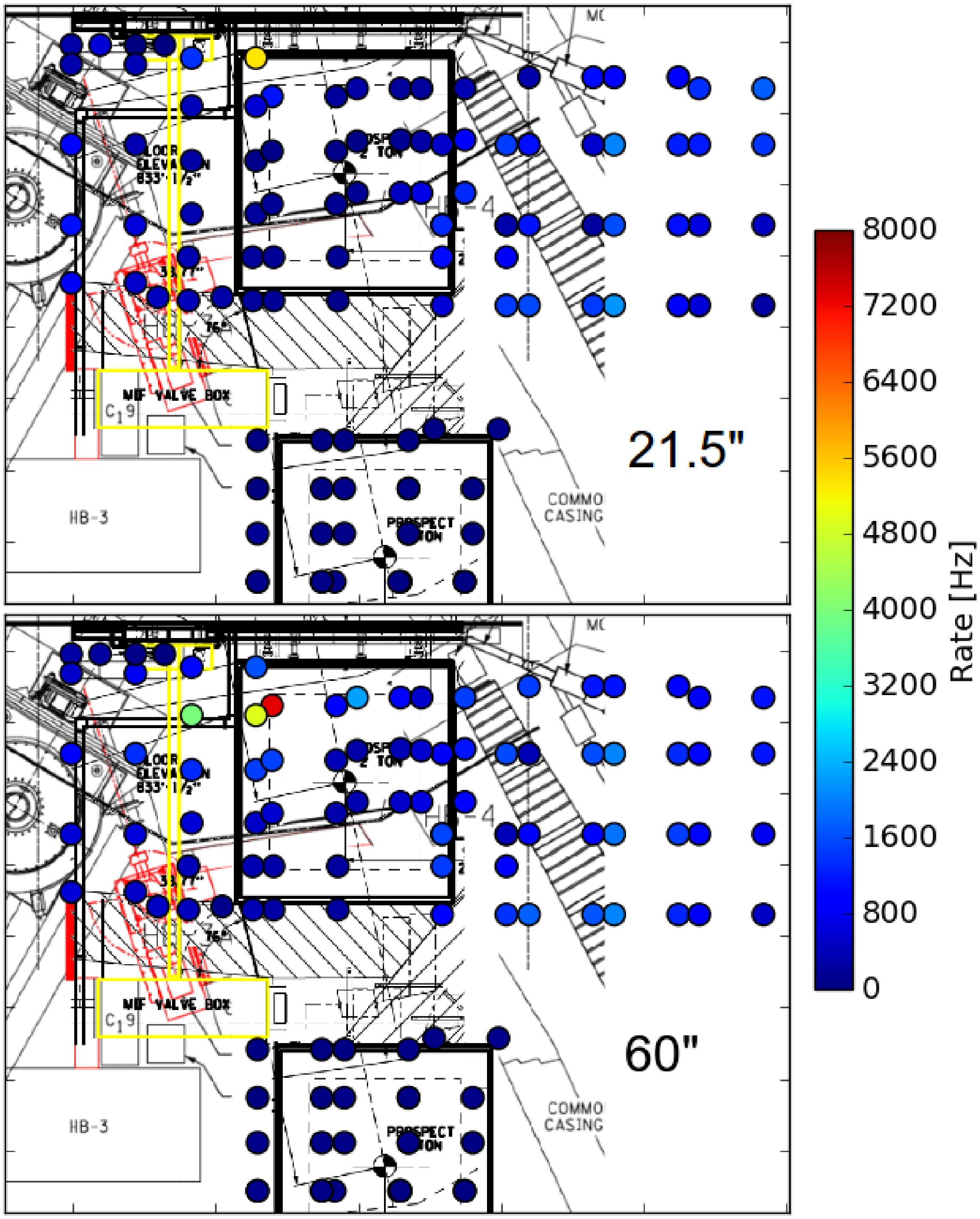

Figure 4.15: 2" x 4" x 16" NaI gamma rates (Hz) for energy depositions between 3 and 5 MeV at different positions throughout the experiment hall during reactor-on, top figure taken at 21.5" above the floor, bottom at 60". Color coded rates are overlayed on a blueprint of the experiment hall, with the upper box corresponding to the near position, and bottom box corresponding to the far position of PROSPECT.

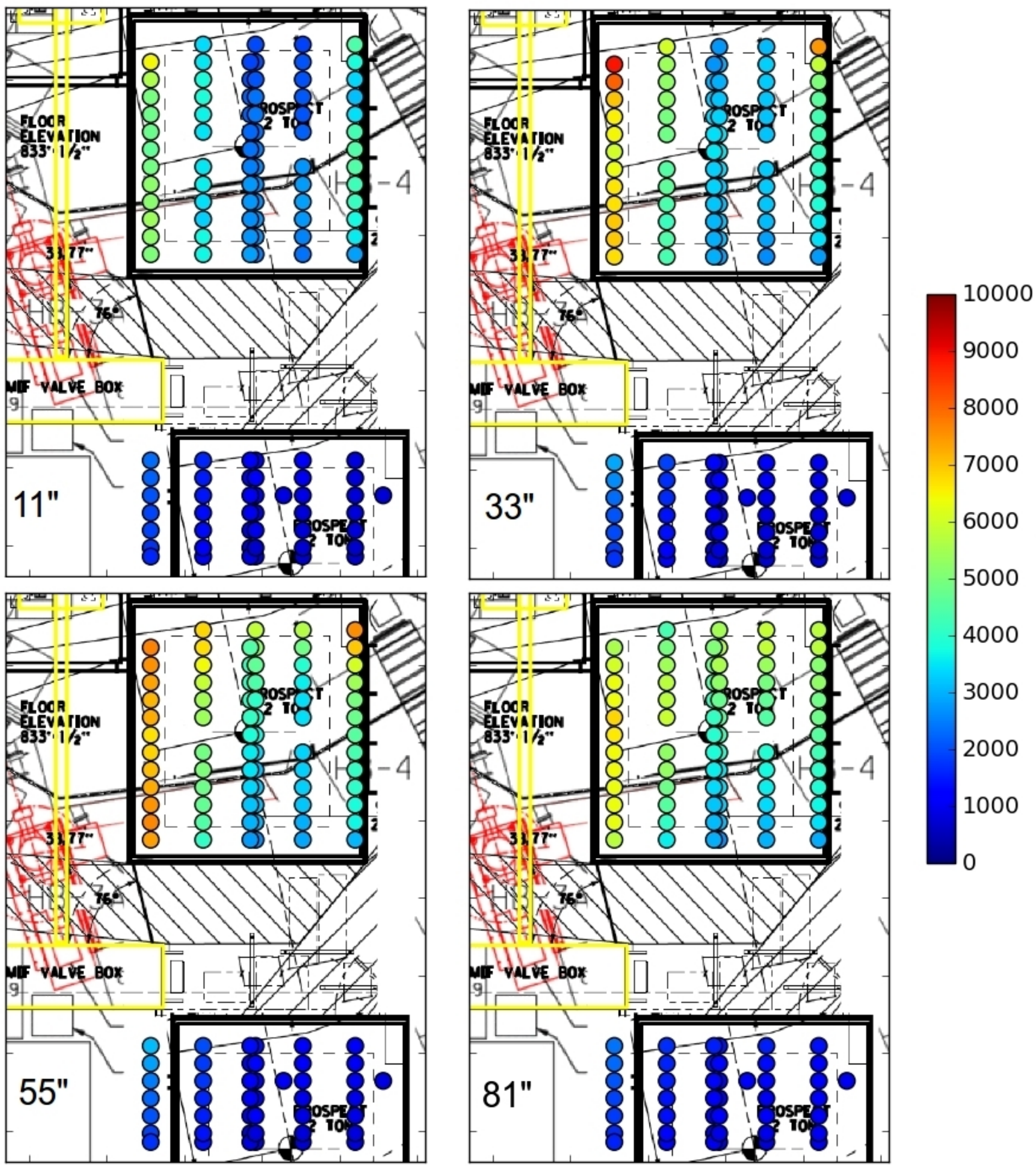

Figure 4.16: 2" x 4" x 16" NaI gamma rates (Hz) for energy depositions between 1 and 3 MeV at different positions throughout the planned near and far positions of PROSPECT during reactor-on. Displayed are rates at 4 different heights above the floor: 11" (top-left), 33" (top-right), 55" (bottom-left), and 81" (bottom-right).

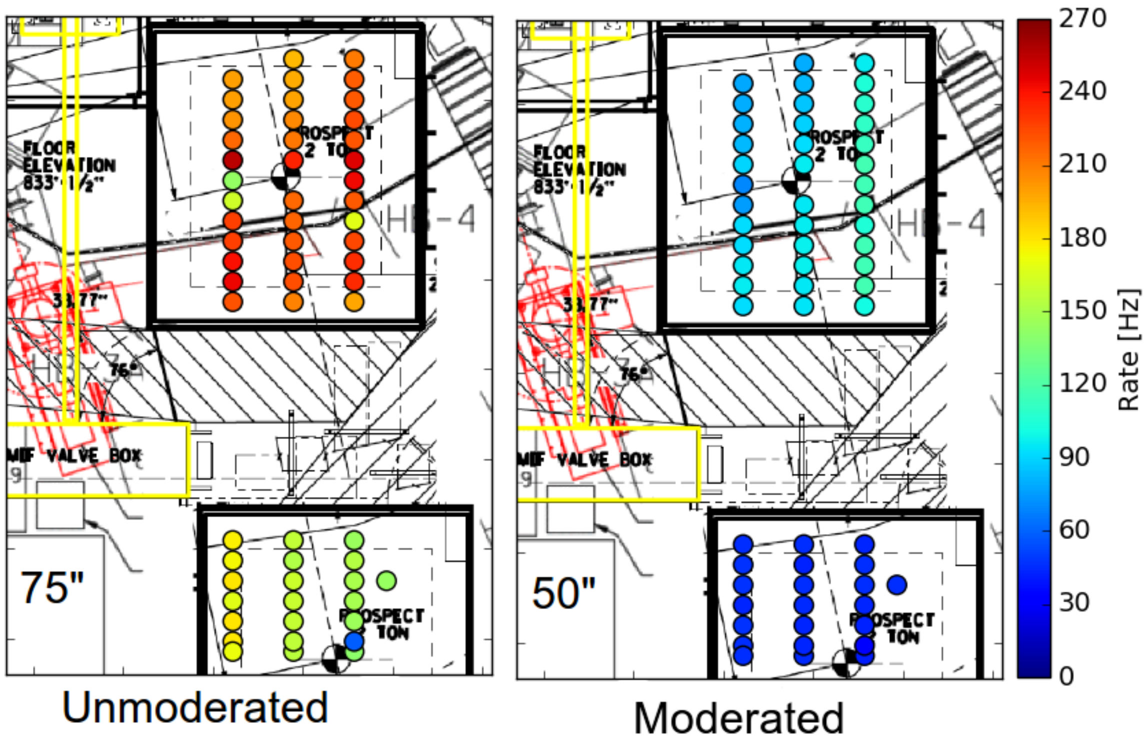

Figure 4.17: 2" ^{3}He thermal neutron rates at different positions throughout the planned near and far positions of PROSPECT during reactor-on. Left plot shows rates from the unmoderated detector 75" above the floor and right plot shows rates moderated by 1" of high-density polyethylene at 50" above the floor.

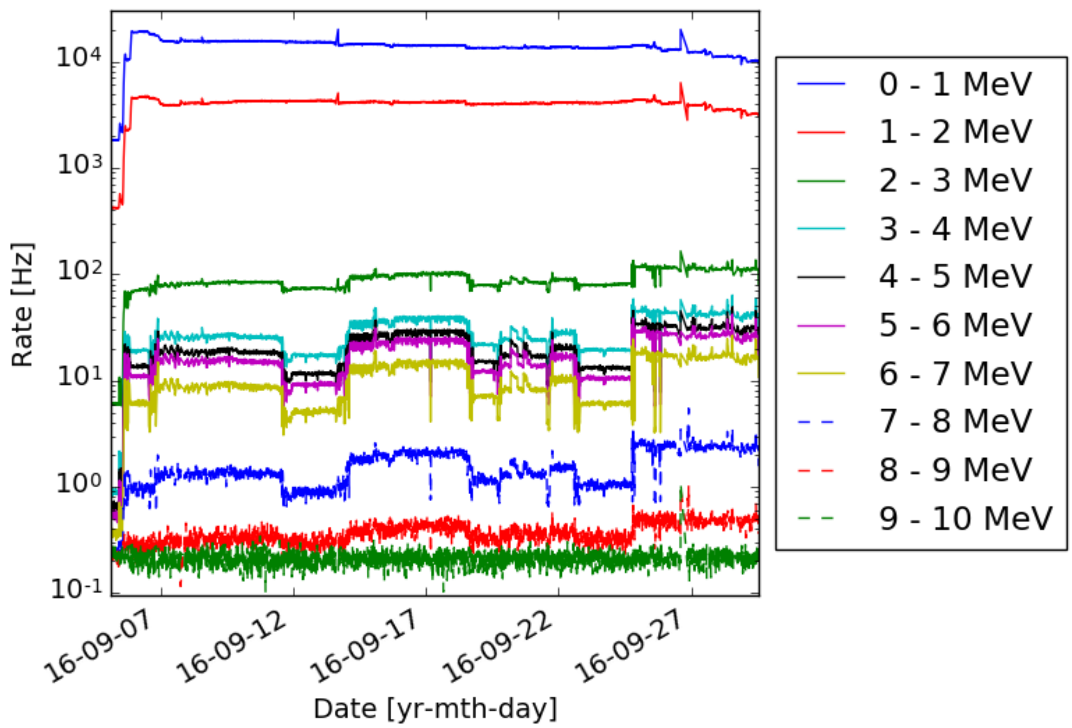

Figure 4.18: Rate history of 2" x 4" x 16" NaI detector gamma rates for various energy cuts during a reactor-on cycle. Note the first few points of data are during reactor-off which are shown to give the reader an idea for the difference in rate between time when the reactor is powered and unpowered. Preliminary investigation into the beam logs of HB-3 finds correlations between various experiments and rates in higher energy bins, presumably from beamline settings causing variations in the amount of neutrons scattered upwards towards the experiment room.

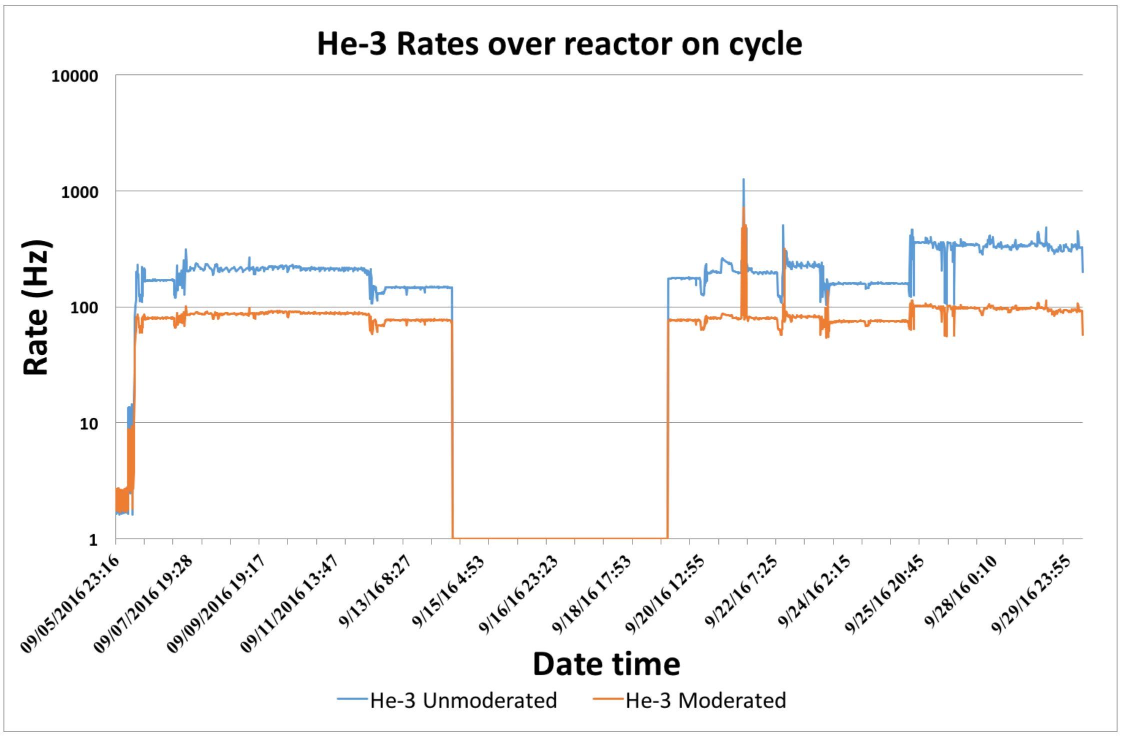

Figure 4.19: Rate history of 2" outer diameter x 24" ^{3}He tubes, one unmoderated at 75" above the floor, the other moderated at 50" above the floor. Moderator is 1" of high-density polyethylene.

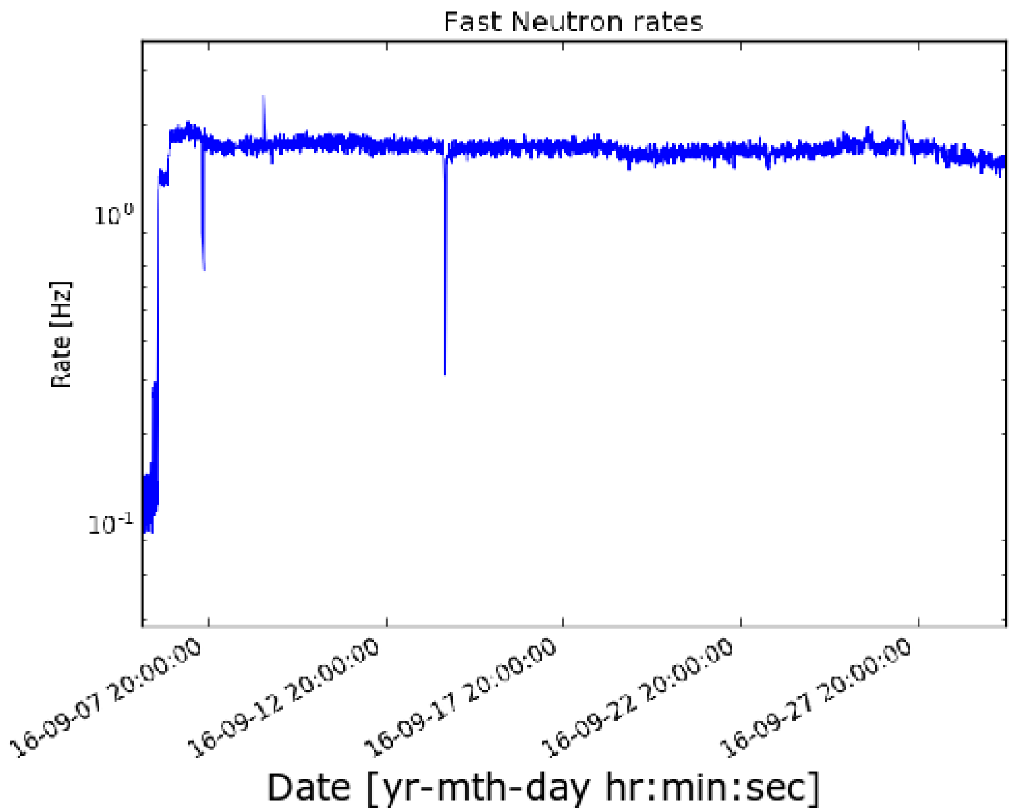

Figure 4.20: Fast neutrons detected from 0.3 to 6.0 MeVee by detectors filled with EJ-301[35] liquid scintillator. We see about an order of magnitude difference between reactor-off and on neutrons in this energy range.

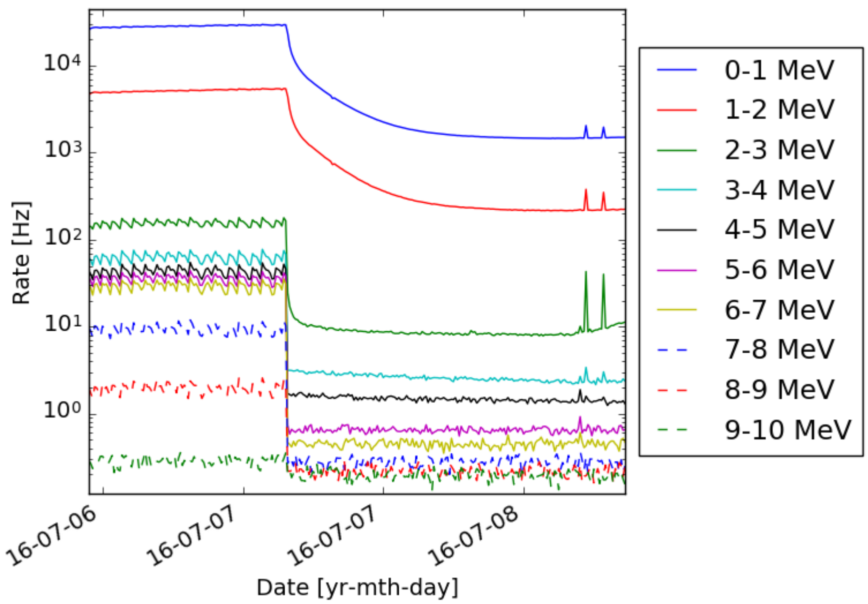

Figure 4.21: Rate history of 2" x 4" x 16" NaI detector gamma rates for various energy cuts during a reactor shutdown. Two spikes near the end of the measurement period correspond to removal of inner and outer fuel rings. Rate increase in low energy bins due to ^{24}Na being vented throughout the building.

Chapter 5

Data Analysis for HFIR Background Measurements

This chapter goes over the various types of analysis required for processing the measured background data. This includes calibration routines, energy resolution calculations and efficiency calculations for NaI, and pulse shape discrimination for the liquid scintillators. Note that much of the analysis involving the manipulation of histograms in this work was facilitated by ROOT - a C++ data analysis framework maintained by CERN[62].

5.1 NaI Analysis

In this section we review calibration routines used for any of the sodium iodide detectors. Additionally, we discuss the energy resolution and efficiency of the 2"x4"x16" detectors and the methods used for long term gain corrections.

5.1.1 Calibration

In order to map ADC integral to energy, sources emitting gammas of well known energy were placed at positions near the background detectors. A two minute data collection period with a source of 10 kBq is sufficient for acquiring enough statistics (1% per-bin uncertainty) with energy bins of 10 keV, as the sources tend to emit gammas in the 0.5 - 1.5 MeV range. A full energy peak will appear in a histogram of ADC integral value, with a Gaussian-like distribution around the most likely value assigned to a gamma interaction that deposits its full energy within the scintillator. It is named the full energy peak, or photopeak. The physics behind the distribution is discussed in section 3.2. The width of the distribution defines the energy resolution, σ, of the detector. σ comes from a Gaussian fit of the full energy peak, defined by $\exp -\frac{1}{2}\left(\frac{(x-x_0)}{\sigma}\right)^2$.

The center of this fit, x_0 provides the ADC channel number to be used in a least-squares regression relating channel number to energy (see figure 5.1). The least squares regression is performed weighting each point by the sigma of the peak. This linear mapping becomes worse at energies larger than the calibration energies where nonlinearities in light output are known to occur[63].

5.1.2 Calibration Sources

When calibrating the sodium iodide detectors, two calibration sources were available - ^{137}Cs, and , ^{60}Co. Additionally, for initial testing, a ^{207}Bi was used. Efficiency calibrations were done using ^{24}Na, ^{56}Mn, and ^{49}Ca. These sources were produced at HFIR and then measured at HFIR's neutron activation analysis lab for a measured activity within 5% uncertainty. These were then used to irradiate the large NaI detectors in order to obtain an estimate of the peak efficiency at energies up to 4 MeV.

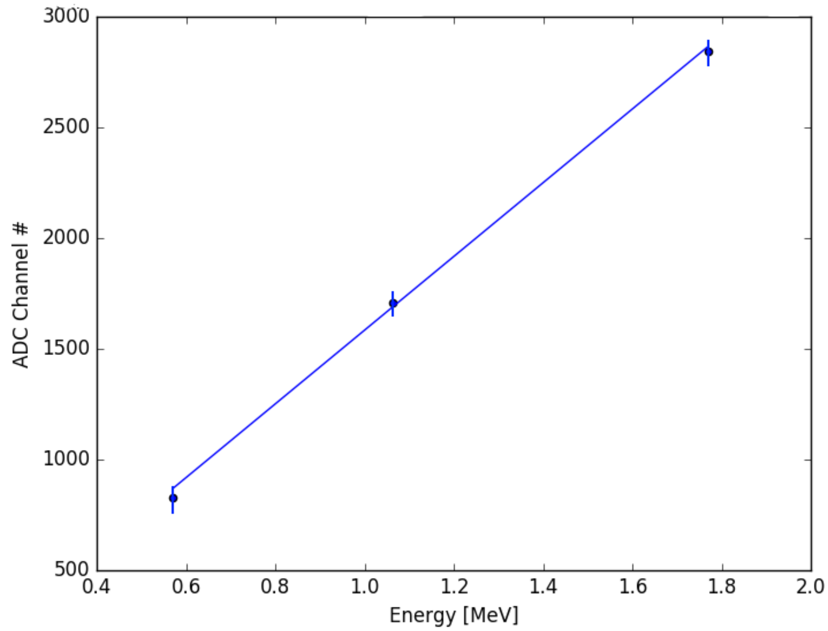

Figure 5.1: Calibration routine for NaI and $CeBr_3$ detectors. The peak energy is plotted along the x axis and the channel along the y axis. The linear regression is used to relate channel number to energy. In this example a ^{207}Bi (0.5697 MeV, 1.0637 MeV, and 1.7702 MeV) source was used for calibration which gives three points to set the linear regression which is weighted by the sigma of the photopeak.

5.1.3 Energy Resolution

After a Gaussian fit on a photopeak is performed, the sigma of the fit can be used to determine the width of the peak. For a Gaussian, the full width at half maximum (FWHM) is defined as $2\sqrt{2\ln 2}\sigma$. The energy resolution is then defined as the FWHM of the peak divided by the centroid of the peak.

We were able to get photopeaks up to 4 MeV using sources for our efficiency calibration in section 5.1.5. An energy resolution vs energy plot using the photopeaks from these efficiency measurements is shown below in figure 5.2.

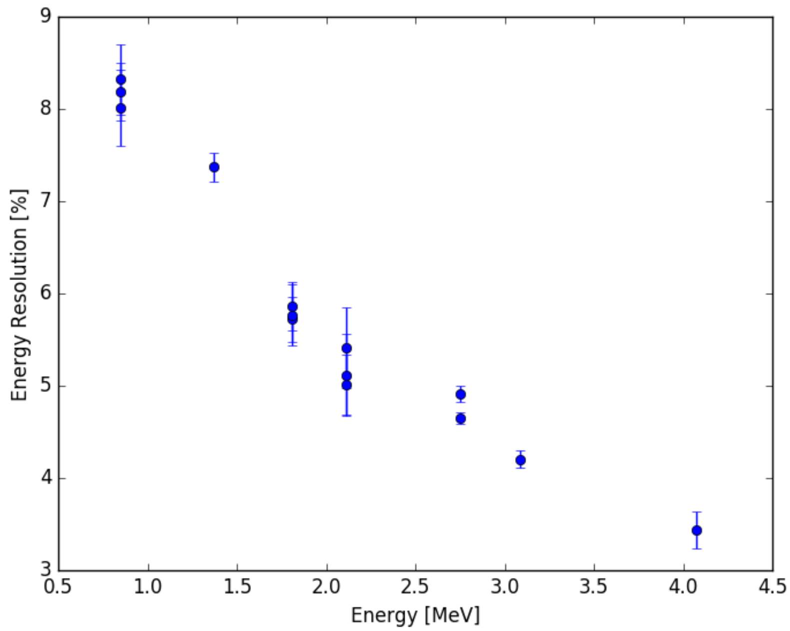

Figure 5.2: Energy resolution of one 2" x 4" x 16" NaI detector for the photopeaks of ^{24}Na, ^{49}Ca, and ^{56}Mn produced at HFIR. Multiple points at the same energy come from measurements taken on separate days with different background conditions.

5.1.4 Gain Corrections

When running over long periods of time, PMT gain drifts due to variation in environmental conditions and temperatures of internal components[64]. Changes in current draw on the PMT can also cause a change in gain, which is often an issue for background measurements taken in a high rate environment. Because these changes can vary on the percent level on day-long timescales, gain adjustments are required to prevent misidentification of features in the reactor background. For the long-term gamma and neutron monitoring discussed in section 3.1, gain adjustments were made using the features that are characteristic to the background during reactor-on and off (see figure 4.7) spectra. With overall count rates reaching tens of kHz for the large NaI brick during reactor on, the gain adjustments could be done using only 10 minutes of statistics, allowing for frequent gain corrections using peak finding and fitting algorithms (see figure 5.3 for gains used during reactor-on cycle 468 for the NaI detectors, and figure 5.4 for NE213 detectors).

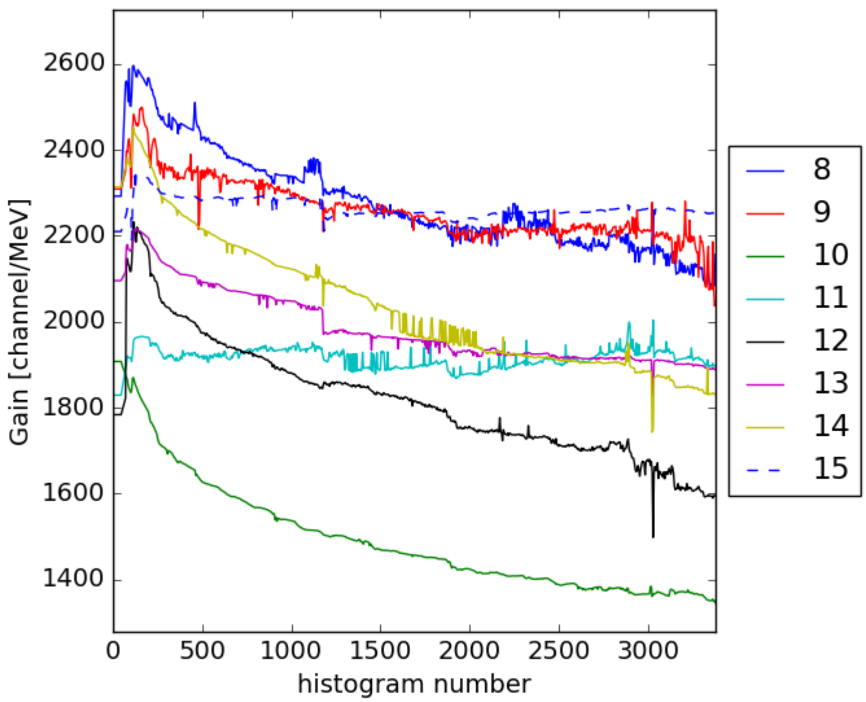

Figure 5.3: Plot of gain used to map ADC channel number to energy deposited. X axis is histogram number, each spanning 10 minutes. Detectors are labeled by logical channel number assigned to the digitizer. Note the first few histograms are taken at the end of a reactor-off cycle, and the first initial jump in gain pictured is due to the increase in rate from the reactor turning on. The increase in event rate causes a large current draw on the PMT which changes the baseline of the signal and creates an increase in the gain. After rates stabilize to normal reactor-on conditions (histogram 75 and onward), the gain fluctuations seen are due to changing environmental conditions.

5.1.5 NaI Efficiency

For our purposes there are two types of efficiency of interest: intrinsic and photopeak efficiency. Photopeak efficiency is defined as the percentage of incident gammas that deposit their full energy within the scintillator. The intrinsic efficiency is defined as

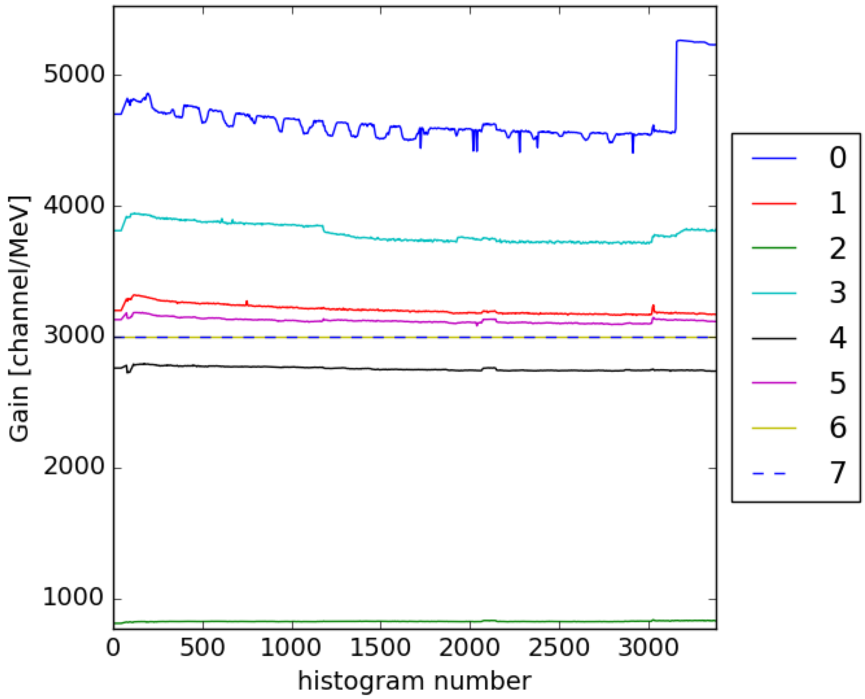

Figure 5.4: Plot of gain used to map ADC channel number to energy deposited. X axis is histogram number, each spanning 10 minutes. This data is from the same time period plotted in figure 5.3 but for the NE213 detectors.

the percentage of incident photons that deposit any energy within the detector. These are both energy dependent quantities, as the likelihood of photoelectric absorption, Compton scattering, and pair production all are energy dependent. For this reason we chose gamma sources with energies up to 4.07 MeV (^{49}Ca) so that we could measure the efficiency across an energy range that covers the bulk of the reactor gamma background spectra.

The procedure consisted of irradiation of a sample material near the reactor core while the reactor was at full power. The neutron activated material was then cooled by allowing the sample to sit in a shielded area for enough time to let the neutron activated contaminants decay off. In general this meant waiting about an hour for the activated aluminum which contained the source material to decay off. The sample was then measured using well characterized germanium detectors at the Neutron Activation and Analysis lab within HFIR. This provides us with a known activity with about 3% uncertainty at a known time. The sample was then brought to four locations near DANG, each location being equidistant to two of the NaI detectors. A ten minute acquisition run was then taken to acquire sufficient statistics for a Gaussian fit on the photopeaks of the radioactive material. Given the knowledge of the source position, one can perform a solid angle correction to know the expected fraction of outgoing radiation incident on the detector assuming a uniform distribution in any given direction from the source. With knowledge of the material's activity at a given time and its half life, one can then calculate the activity at the time of acquisition and multiply by the solid angle fraction covered by the detector to get an expected incident activity. Using knowledge of the gamma branching ratios for each isotope, one can then calculate the photopeak efficiency using the area of the peak found in the energy spectrum.

In order to calculate the number of events in the detector and in each photopeak, the spectrum taken is calibrated and divided by the live time of acquisition. Then, a background run which was taken moments before the source was brought to the detector is calibrated and rate normalized, and this background run is subtracted from the source spectrum. An example of this background subtraction is shown in figure 5.5.

When doing these efficiency measurements we noticed that the efficiency also depended on the overall trigger rate of the detector. An example of photopeak efficiency as a function of rate at different energies is given below in figure 5.6.

It should be noted that for all DANG NaI measurements presented in this work there was a drop in efficiency at rates higher than 10 kHz resulting from an issue with ORCHID, the DAQ used by DANG[65]. This issue has since been corrected.

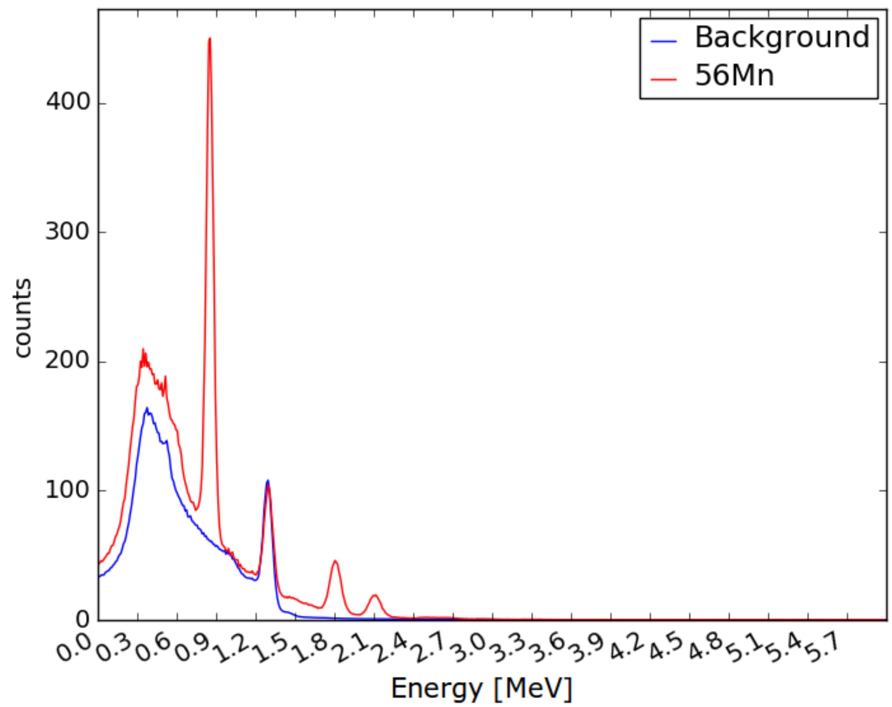

Figure 5.5: Calibrated spectrum of ^{56}Mn along with background used for subtraction.

5.1.6 Peak Finding Algorithms

Because a large number of detectors were deployed and gain drifts were an issue, an automated peak searching algorithm was developed to identify peaks and correctly match identified peaks to source energies.

Using ROOT's TSpectrum class[66], a background subtraction is performed on a histogram which is intended to subtract out flat backgrounds and the Compton edges of peaks within the spectrum. An example of this background subtraction is in figure 5.7.

The background subtracted spectrum is then run through a peak finding algorithm that first finds all local maxima then filters these based on distance from the largest maxima found assuming an energy resolution of 4%, which is the narrowest peak we would expect based on experience with these detectors (see figure 5.2). These maxima

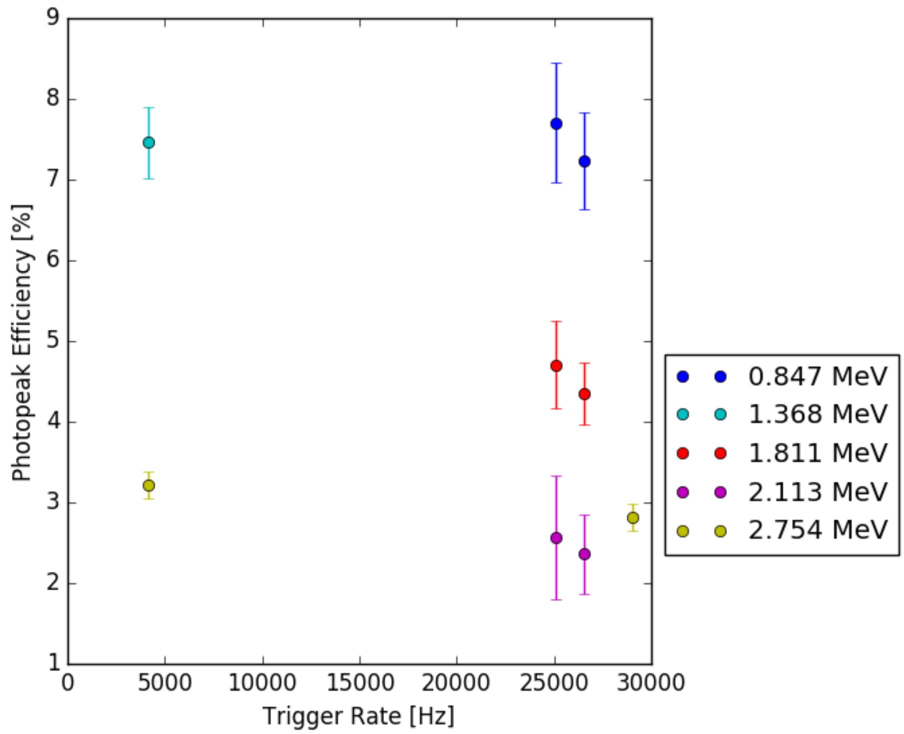

Figure 5.6: Photopeak efficiency vs trigger rate for ^{24}Na and ^{56}Mn measurements.Uncertainties shown are a combination of systematic uncertainties in the source activity, source position and background subtraction, and statistical uncertainties in the peak area. Note that for these efficiency measurements, there was an additional drop in efficiency due to an issue with the DAQ being used that has since been resolved[65].

are then filtered based on a threshold that is set as a percentage of the amplitude of the largest maxima found. This threshold would be set depending on the relative exposure to various sources that are being used for the calibration. For example, if one wishes to find the two ^{60}Co peaks, a threshold of 10% is fine to identify them, as the two primary gamma transition strengths are 99.98% and 99.85%. For gain correcting the reactor-on spectra, on the other hand, a much lower threshold of .5% was often used in order to find both the 511 keV peak from annihilation gammas which showed up at a far lower rate than the 1.294 MeV gamma coming from the ^{41}Ar decay in the MIF.

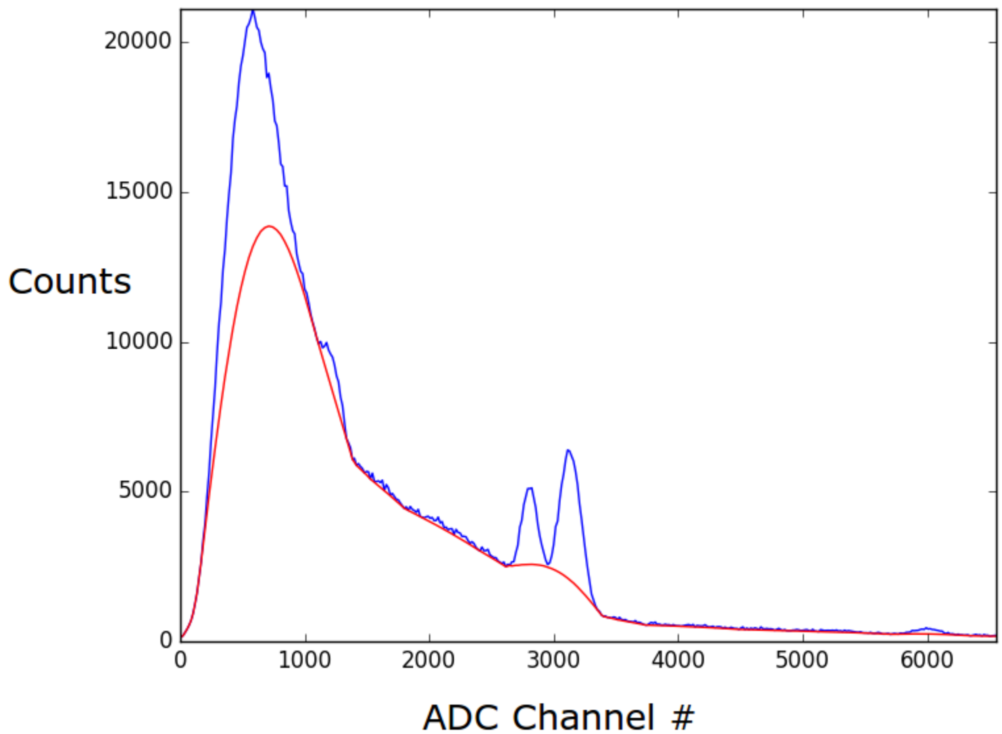

Figure 5.7: Background subtraction using ROOT's TSpectrum. Pictured in this example is a ^{60}Co source. Data in blue, background subtraction in red.

Once a list of maxima is chosen, Gaussian are fit to each peak, obtaining the peak position, sigma, height, and area. Then, all unordered combinations with length n, where n is the number of expected peaks, are found and their relative positions are calculated and compared with the relative positions of the source peaks. A chi squared value is calculated using the peak width as the sigma of the peak position in order to determine which set of peaks best matches the expected set. If the minimum chi squared value for this peak search is exceeded, then the peak finding threshold is lowered or various parameters in the background subtraction are altered and the algorithm is repeated until a set of peaks are found which falls beneath the chi-squared threshold. This was done so that gain corrections for large datasets do not have to be done by hand, and it is how figures such as figure 5.3 were produced.

5.2 Liquid Scintillator Analysis

In this section calibration routines for the NE213 and deuterated detectors are reviewed. This includes mapping between ADC channel number and light output from electron-like recoils and pulse shape discrimination routines for separating neutron and gamma recoils.

5.2.1 Liquid Scintillator Calibration

For the liquid scintillators used such as NE213 or EJ-309, the efficiency of detection for gamma rays is much lower, and thus to calibrate gamma-like recoils the Compton edge of a calibration source energy distribution must be fit (see figure 5.8). This is done with a least squares fit of a complementary error function plus a constant. The complementary error function, erfc, is defined by $\mathrm{erfc}(z) = \frac{2}{\sqrt{\pi}} \int_z^\infty e^{-t^2} dt$. The resulting z of the fit is then used as the channel number of the Compton edge. Note that the Compton edge $E_{Compton}$ of a gamma with energy E is defined by the relation $E_{Compton} = E\left(1 - \frac{1}{1+\frac{2E}{m_e c^2}}\right)$, where m_e is the mass of the electron and c is the speed of light. The location of this edge in channels can be used to get an approximate relationship between channel and energy deposited for gamma and electron recoils. Due to light output quenching[67] in heavier particles, other methods must be used to get energy information for neutron, alpha, and compound nuclei. For the NE213 detectors, because neutron energy comes from scattering on protons, neutron energy can only be obtained via time of flight measurements. However, with the EJ-315 deuterated liquid, the ^{2}H neutron recoil cross section has a peak at 180 degree backscatters, which allows for a neutron energy mapping between light output in electron-equivalent calibrated energy and neutron energy deposited[68].

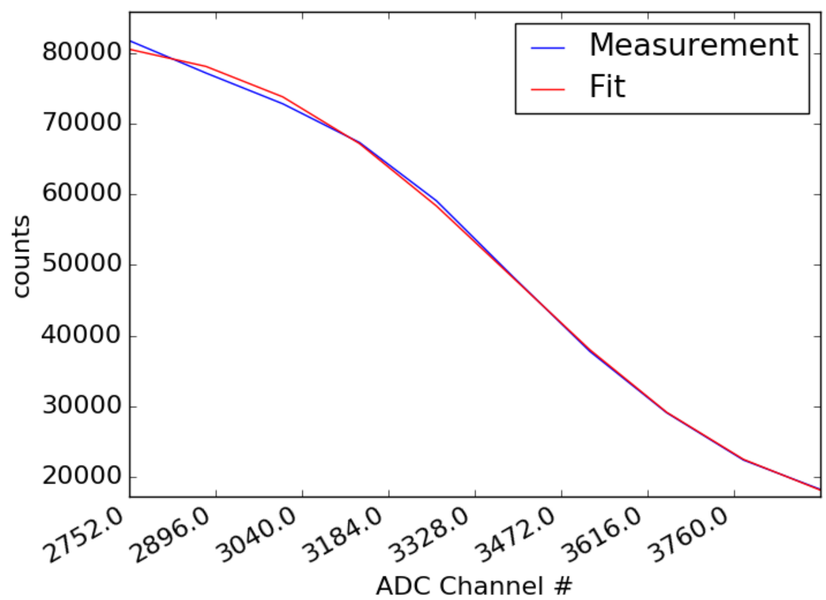

Figure 5.8: Calibration routine for liquid scintillator detectors. Pictured is zoomed in on the edge of the spectrum (blue) with the Compton fit overlayed (red). The Compton edge is fit using a complementary error function plus a constant.

5.2.2 Pulse Shape Discrimination

Due to the differing mechanisms by which particles deposit energy, the time structure of the pulse recorded by a PMT can be used to distinguish between particle types. This is particularly useful for the liquid scintillators because it allows discrimination between neutrons and gammas. The simplest method of pulse shape discrimination (PSD) is the tail-fraction method, in which the integral of the tail of the pulse divided by the full integral is histogrammed for each pulse while taking data from a neutron source, generally a ^{252}Cf source which is useful for its spectrum of neutron emission after spontaneous fission. Figure 5.9 is an example of such a plot. The cutoff point for determining where the tail begins was varied and a metric that quantifies the degree of separation between neutron and gamma PSD distribution was recorded for each cutoff point. The cutoff point maximizing the separation between neutrons and gammas for each detector was used in the analysis to generate PSD values.

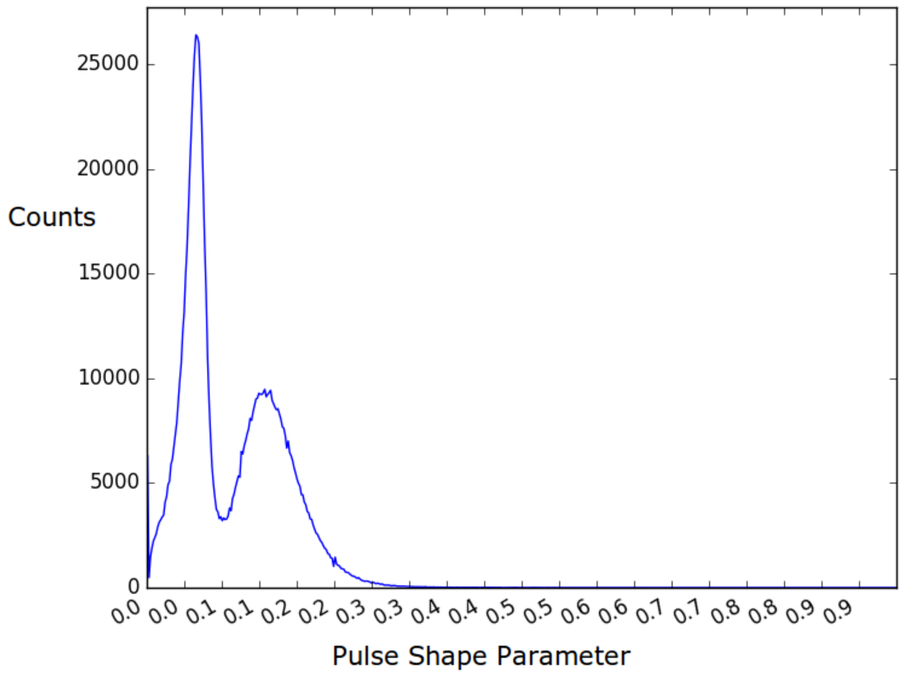

Figure 5.9: Histogram of PSD for events taken with a ^{252}Cf source near an NE213 cell. The two Gaussian distributions result from the variance in fraction of the slow component of electron deexcitation between neutrons and gammas, with neutrons tending to deposit more energy through the slower channels relative to gammas.

5.2.3 Neutron Recoil Cuts

Neutron recoils were selected using measured ^{252}Cf, which spontaneously fissions and is therefor a good source for a wide range of neutrons in the fast energy range (MeV scale). A visual cut is performed on the PSD vs Energy histogram, which is first calibrated to units of MeV electron-equivalent (MeVee) by using a gamma source and fitting its Compton edge. The cut set can then be used on any calibrated histogram taken with the same detector, assuming the parameters used to calculate PSD do not change. Both the NE213 detectors and the deuterated detectors would see clipping of the signal set in at a given energy range, and thus cuts were set across detectors so that the maximum neutron energies included were just below the lowest energy in which clipping sets in across detectors. For example, the NE213 cuts were set from 0.3 MeVee to 6.0 MeVee because one of the detectors saw clipping as low as 6.0 MeVee. An example of this cut is seen in figure 5.10.

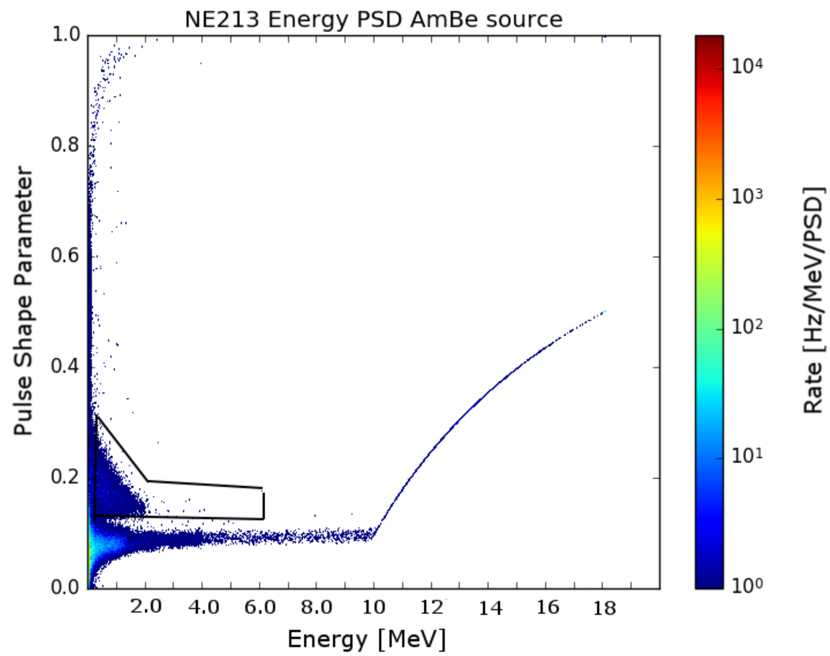

Figure 5.10: Histogram of background events taken with an AmBe source used to set the neutron cut (black lines).

5.3 ^{3}He Analysis

The ^{3}He tubes output a signal with a very long time constant compared to the liquid scintillators and the sodium iodide detectors (see figure 5.11). In order to integrate these detectors into the same DAQ, a shaping amplifier is used which converts the 120 μs long pulse into a 20 μs wide Gaussian which is then fed into the digitizer. This shaped pulse must exceed a voltage threshold is set so that we are insensitive to electronic noise within the tube. The cross section for gamma interactions in these tubes is very low compared to neutron interaction, and thus we can get a reasonable handle on thermal neutron rates by simply looking at the rate of triggers in the tube. To ensure that gamma radiation does not contaminate, an intense gamma source was brought near the tubes. This source which would produce tens of kHz in the large NaI detectors only raised the count rate by 0.5 Hz in the helium tubes, leading us to believe that they are fairly insensitive to gammas.

In order to get proper energy information on the energy deposited in these tubes, one would need to record the trace of the outgoing signal to find the pulse height and rise time of the event. This would allow for discrimination between electron and neutron depositions. However, since our DAQ is not setup to record traces as this is a very storage intensive procedure in such a high rate environment, we decided to simply record the integral of the pulse which cannot be used for energy, but can at least tell us that a neutron probably interacted.

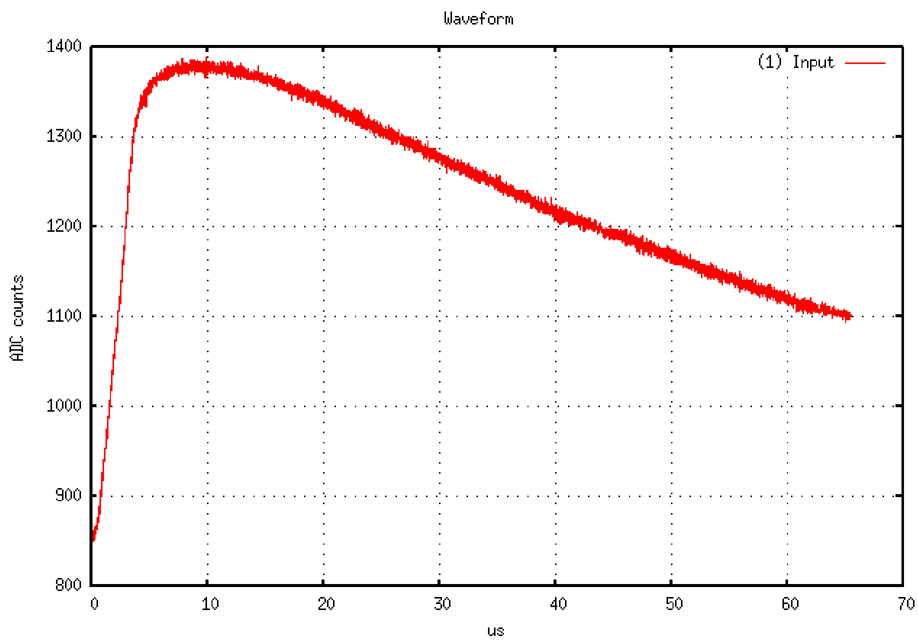

Figure 5.11: Standard pulse from ^{3}He tube.

Chapter 6

Simulation of HFIR Backgrounds

Simulation work done has mostly been focused on understanding the gamma backgrounds. We have simulated the 2 x 2 array of NaI bricks, and performed simulations of radioactive source data to tune the detector response via energy dependent Gaussian smearing. This understanding of the NaI detectors allows us to reconstruct the incident gamma energy of a measured spectrum which can then be fed back into the simulation of the full PROSPECT detector to determine the impact of the measured gamma field on IBD-like backgrounds.

6.1 NaI Detector Response

In order to interpret the data from our gamma detectors, we simulated the detector geometry and electromagnetic physics for NaI in Geant4[59]. Simulation was focused on the large NaI bricks because they provided the best full energy peak efficiency. The geometry of the NaI crystal along with the stainless steel exterior shell was simulated and gammas of energies ranging from 0.1 to 12.0 MeV in 20 keV increments were simulated at random positions outside of the detector with an isotropic distribution of momenta directed into the active volume. The histogrammed energy depositions from each energy simulated were then used to reconstruct the measured spectra in terms of the detector response.

6.1.1 Radioactive Source Validation

In order to validate that the simulation was working as intended, we first simulated the energy spectra for ^{137}Cs, ^{60}Co, and ^{137}Bi (figures 6.1, C.2, C.1). The simulation was compared with a background subtracted source run. The low energy portion of the spectrum was not properly simulated as this requires a simulation of the voltage amplification and pulse height thresholds and is not very important for reconstructing energy spectra when MeV scale energies are interesting.

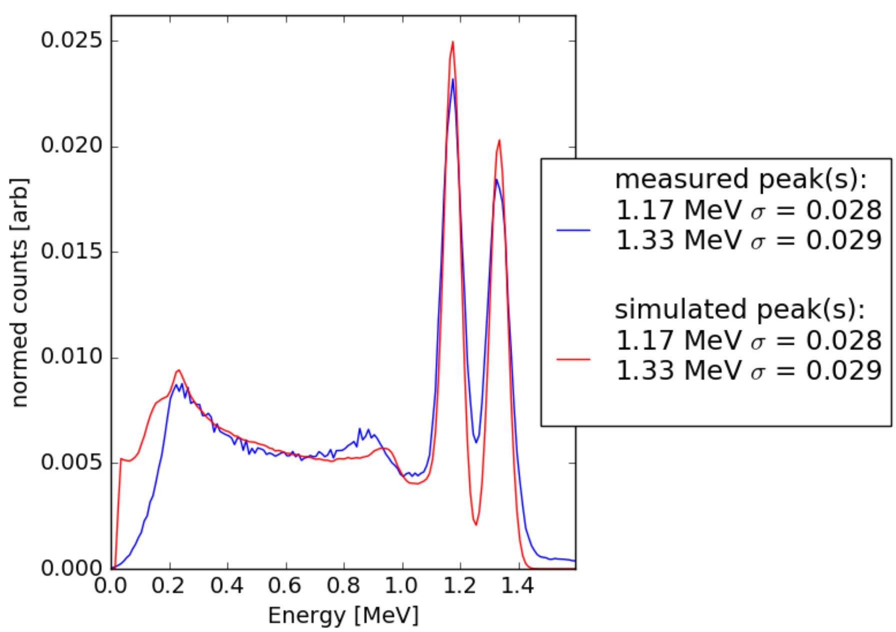

Figure 6.1: ^{60}Co simulation and data. Note data is background subtracting using ambient spectrum collected moments before source run. Note source spectrum is not properly calibrated hence the offset relative to simulated spectrum. Simulated spectrum shows a slightly better energy resolution indicating needed improvements to the resolution smearing function.

These figures indicate a need for an improved energy resolution smearing function as guided by source measurements in section 5.1.5.

6.1.2 Unfolding a Spectrum

When unfolding a spectrum, we wish to find the weights w_j to solve the problem

$$S_{meas}(E_i) = \sum_j w_j S^j_{sim}(E_i), \tag{6.1}$$

where $S_{meas}(E_i)$ is the measured energy spectrum at energy bin i, $S^j_{sim}(E_i)$ is the simulated energy spectrum for incident gammas of energy E_j at energy bin i. The simulated incident gamma spectra are constructed by sending an isotropic distribution of gammas in energy increments of 20 keV between 0.1 MeV and 12.0 MeV into the simulated geometry of the large NaI detectors. An example of this is given in figure 6.2. Using the simulation output of the energy deposited in the scintillator, one then uses Gaussian smearing based on the energy resolution measured for the NaI detectors in order to obtain a more realistic spectrum (see figure 6.3). Because we cannot find an exact solution to equation 6.1, a "stripping algorithm" is used to approximate the proper weights. This is done by starting at the uppermost bin E_f of a measured energy spectrum, $S_{meas}(E_f)$, using the content of this bin to scale the simulated incident gamma spectrum S^f_{sim} so that the photopeak of the simulated spectrum matches the bin height of the measured spectrum, providing the weight w_f. This scaled simulated spectrum is then subtracted from the original spectrum. This is done in 40 keV increments down the spectrum, 40 being chosen due to its proximity to the detector resolution σ in this energy range. See figure 6.4 for an example of this reconstruction. The reconstructed incident gamma energy histogram is then the weights w_i used in the subtraction for each energy bin E_i multiplied by the integral of the simulated response and divided by the intrinsic efficiency of the detector at that energy. The intrinsic efficiency at energy E_i is defined as the total number of detected events divided by the total number of gammas of energy E_i that passed through the active detector volume. Note that for this work an intrinsic efficiency of 50% was used for all energy bins. In reality this will decrease with increasing incident gamma energy, and a simulation of the efficiency measurements described in section 5.1.5 can be performed to construct an intrinsic efficiency vs energy curve for each detector.

The resulting reconstructed histogram can then be fed back into the simulation to simulate gamma recoil rates from room backgrounds within the full PROSPECT detector. Both reactor-on and reactor-off unfolded spectra are shown in figure 6.5.

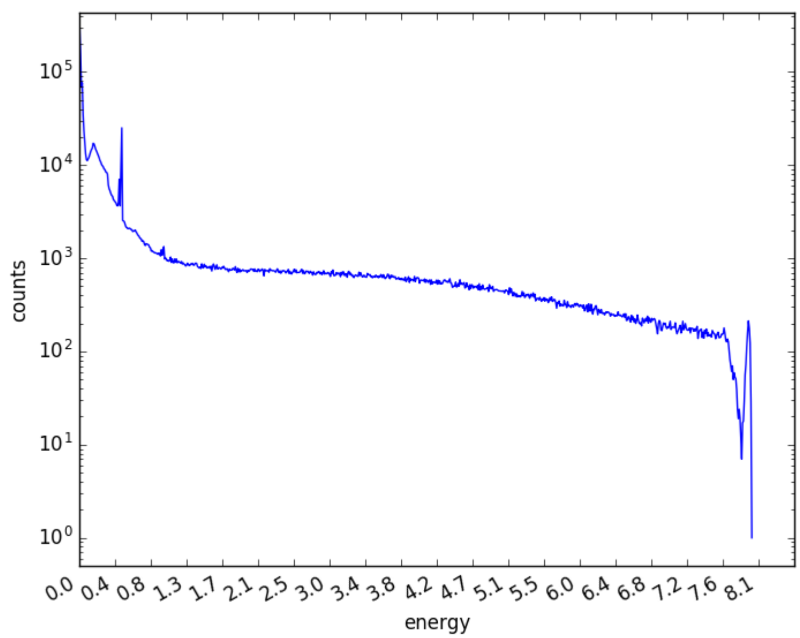

Figure 6.2: Histogram of Geant4's energy deposition output for a monoenergetic flux of 8 MeV gammas incident on a large NaI brick. Displayed is a histogram of all ionizations recorded by the simulation.

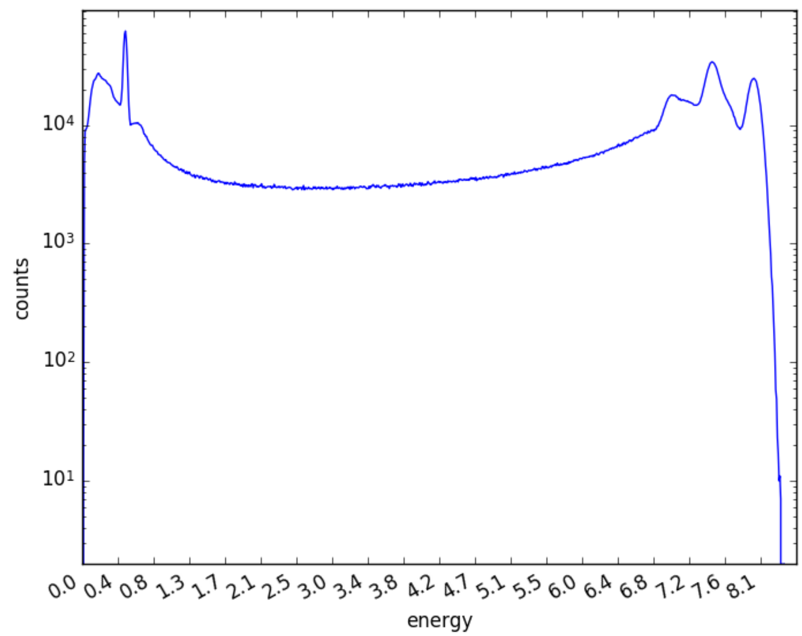

Figure 6.3: This histogram was produced with events displayed in figure 6.2. Energy depositions close together in time (tens of nanoseconds) are combined into single detected events then smeared using Gaussian smearing to approximate the energy detected by the PMT. Note the single escape peak at 7.49 MeV and the double escape peak at 6.98 MeV.

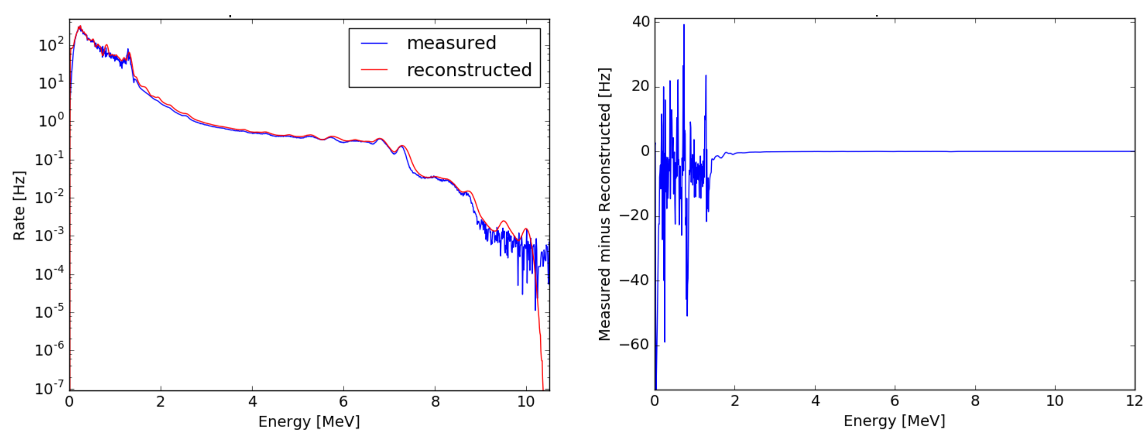

Figure 6.4: Left: Reactor-on spectrum plus reconstructed spectrum. Right: Measured minus reconstructed. Note this reactor-on spectrum was measured while the MIF was in operation, and the MIF component was subtracted using a method detailed in section 6.2.1. For this reconstruction, $\frac{\sum_i |R_i^{meas} - R_i^{reconst}|}{\sum_i R_i^{meas}} = 0.11$, where R_i is the rate at energy bin i.

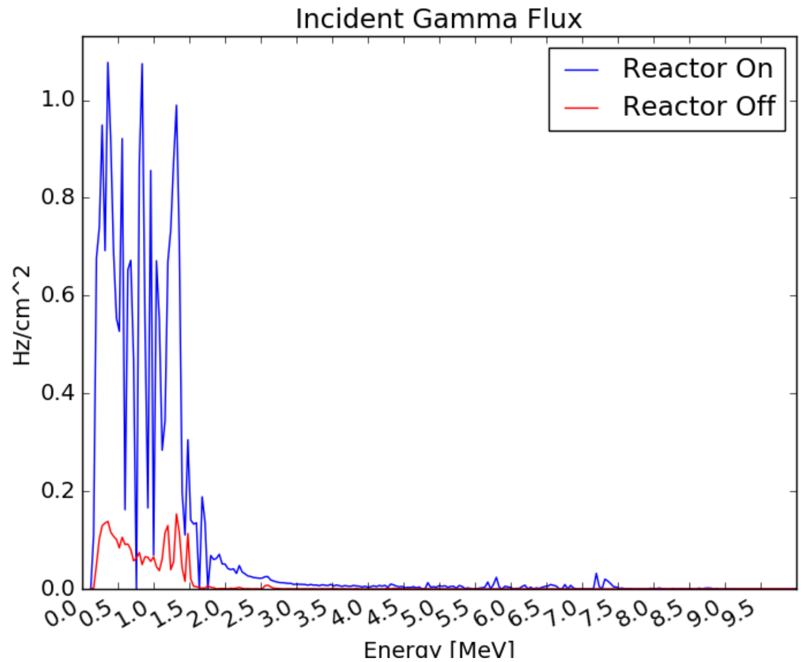

Figure 6.5: Incident gamma flux recorded during a reactor-on and reactor-off period. Spectra were obtained by unfolding the muon subtracted measured spectra (see figures 6.4 and C.3) using simulated detector response of incident gammas in 20 keV increments.

6.2 Components of Gamma Backgrounds at HFIR

Gamma backgrounds at the experiment site at HFIR can be broken up into three main components: the reactor-off component, the reactor-on component, and the MIF component (see figure 4.7). The reactor-off component is mostly typical room backgrounds with noticeable lines from the uranium and thorium decay series (see figure 4.7), while also containing some long lived neutron activated material, most notably ^{60}Co. This comes from the steel used for structural integrity throughout the building, given its proximity in mass and proton number to iron, cobalt tends to exist in commercial grade steel.

When the reactor is operating the experiment hall is mostly shielded from gammas coming from beta decaying isotopes in the core. Instead neutron capture gammas are detected from the thermalized neutrons reaching materials in and around the experiment hall (see figure 4.7). This background is time varying due to the proximity of beamlines 3 and 4 to the experiment hall. While the component from beamline 4 is fairly constant after a short equilibration time after the reactor starts up, the component from beamline 3 can show marked differences as the angle of the beam is changed for experimental purposes. The reason the site of PROSPECT is more sensitive to beamline 3 changes is due to the fact that spectrometers of beamline 3 are located just a few meters west on the floor below, whereas the instrumentation of beamline 4 exists tens of meters away from the experiment hall (see figure 4.4). Time variation of the backgrounds at the PROSPECT experiment location can be seen in section 4.5.3.

The MIF is an experiment that is sometimes active during a reactor-on cycle in which argon gas is circulated via pipe to the reactor core and back through a drywall junction box at the north end of the experiment hall to the south wall of the experiment hall for sampling and analysis. Given the large flux of neutrons close to the core, a fraction of the argon gas captures neutrons and becomes ^{41}Ar, which has a gamma line at 1.294 MeV. The argon transfer line is shielded with lead, but radiation from it still accounts for roughly half of the radiation received in the 0.1 to 1.29 MeV range during a reactor-on period, and thus is important to consider in simulations of the room gammas. However, since it is not always running during reactor-on cycles, it is also useful to separate this component from the normal reactor-on radiation.

6.2.1 MIF Validation

While the MIF experiment does not occur every reactor-on cycle, it has been present since we have started deploying our NaI bricks to measure the reactor-on background. This means that we had to use the reactor shutdown period to isolate the MIF component from typical reactor-on radiation. This was done by examining rates of various energy ranges of the gamma spectrum after the reactor shutdown (see figure 4.21). The component in the 1.2-1.4 MeV range is dominated by the ^{41}Ar decay which has a half life of 110 minutes[69]. Most of the neutron activated materials have half lives that are much shorter, on the order of minutes such as ^{61}Fe which has a half life of 6 minutes[69], or much longer such as ^{63}Ni with a half life of 100 years[69]. By cutting on the spectrum in time about 4 ^{41}Ar half lives after the reactor shutdown, there is still enough radiation from the MIF to see its component above the reactor-off background, and most of the reactor-on component has decayed away (see figure 6.6). The resulting spectrum along with the reactor-off subtraction can be seen in figure 6.7. This spectrum was then unfolded using a stripping algorithm as shown in figure C.5, and rescaled by a constant factor to match the reactor-on plus MIF spectrum. This number was verified by looking at the binned value of the unfolded reactor-on plus MIF spectrum at 1.29 MeV, and the binned value of the MIF component at 1.29 MeV to find the proper rescaling (see figure 6.8 for result of this scaling). The MIF component can then be subtracted from the measured reactor-on spectrum, which was then unfolded to find the ambient reactor-on gamma flux (figure 6.5). Note that the detector response from cosmic muons was simulated using CRY[60] and subtracted from each spectra before the unfolding since this is the largest non-gamma background present in the NaI detectors.

While the directionality of the gamma field is complicated, the radiation coming from the MIF is easier to characterize because the physical location of the MIF transport line is known. In Geant4 we simulated this line by throwing the MIF energy spectrum from the location of the pipe at the 2 x 2 NaI detector array (section 3.1.3). To obtain the proper rate used in our simulation, the transport line was approximated as three line segments, ignoring the segment that moves down into the reactor core because it is well shielded by the monolith. A solid angle correction was then applied to the measured MIF spectrum (see figure 6.8). The energy spectra were then compared for each detector (see figure 6.9). This check shows that our choice for the location

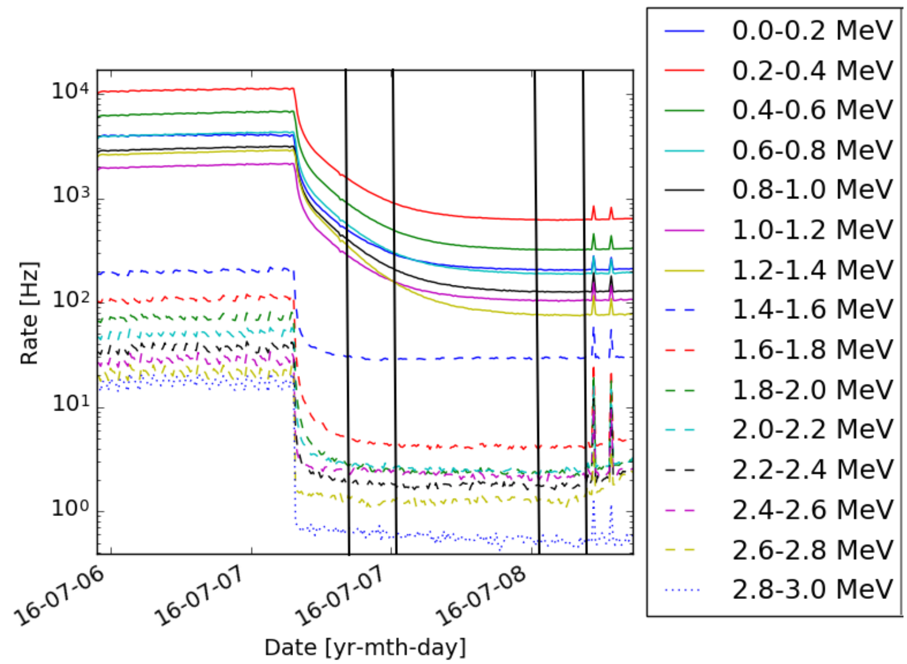

Figure 6.6: Reactor shutdown period, detected gamma energy rates in 0.2 MeV increments, from 0 to 3 MeV. This energy width was chosen to show the various components of the reactor-on background decaying out, with the 1.2 to 1.4 MeV rate dominated by the ^{41}Ar decaying in the MIF line. Cut region on the left is used as the reactor-off plus MIF spectrum, and cut on the right (about 10 ^{41}Ar half-lives later) is the spectrum used for subtraction (see figure 6.7).

from which to throw gamma events is oversimplified and could be improved by implementing a more realistic geometry based on HFIR blueprints of the MIF. Given that the results are within 20%, we decided to go ahead and use this generator to get an estimate of the MIF's impact on the full PROSPECT 3 ton detector.

6.3 AD-1 Simulation

Simulation of the full AD-1 detector design has been carried out in order to understand the impact of the ambient gamma field on accidental gamma neutron coincidences which can provide background for the IBD signal. The simulations detailed here are a rough first pass in order to ensure that the HFIR gamma field does not adversely

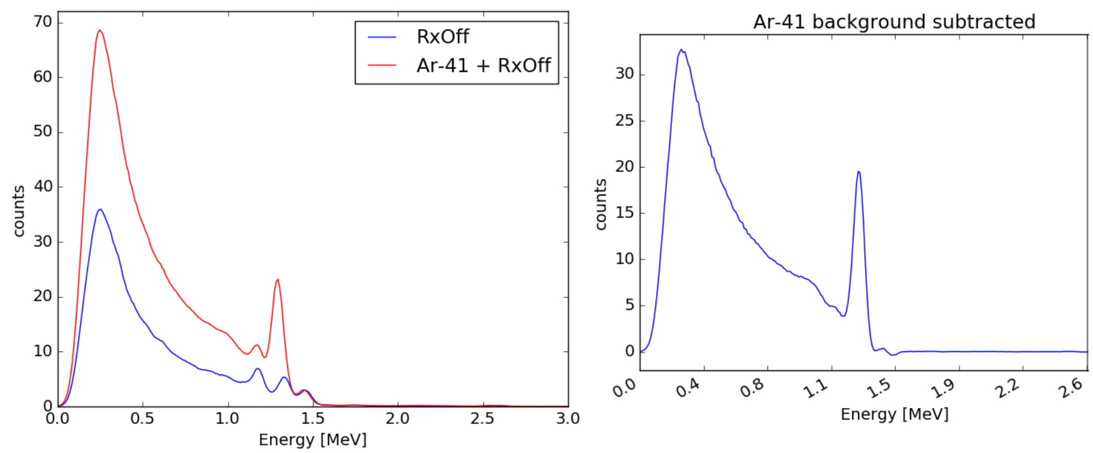

Figure 6.7: Left: Energy spectra from cuts used in figure 6.6, right: background subtracted spectrum. This is the MIF spectrum that is scaled to match reactor-on levels then reconstructed in incident gamma energy for MIF simulation (see figure C.4).

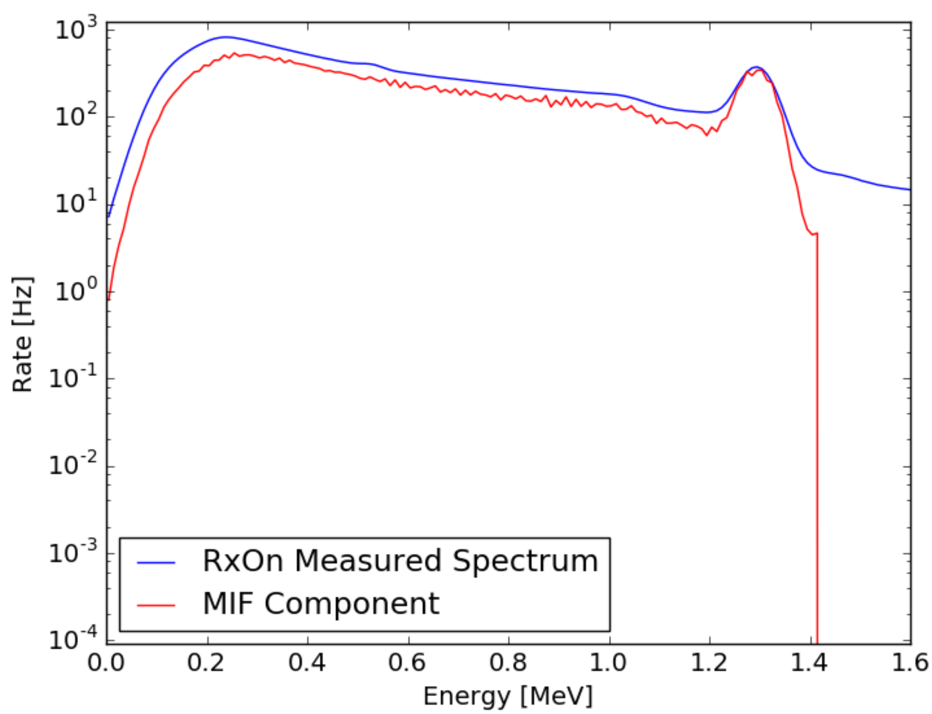

Figure 6.8: Measured reactor-on spectrum (blue) plus estimated contribution from the MIF ^{41}Ar decay (red).

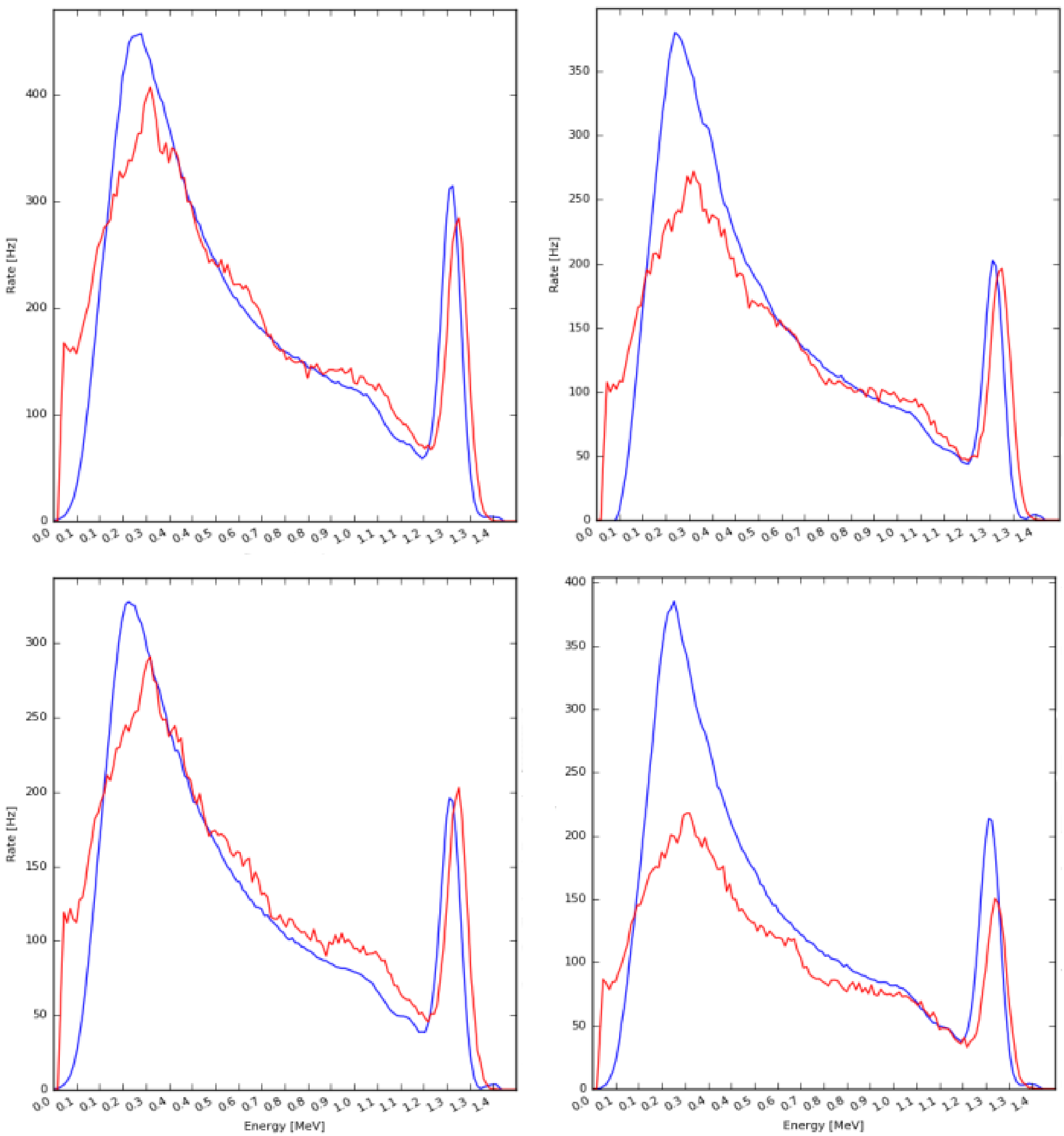

Figure 6.9: MIF simulation (red) vs measurement (blue) for each of the detectors on the 2 x 2 array. Gamma events were generated by randomly selecting a point along the MIF transport line with an energy spectrum shown in figure C.5.

impact our signal to background with the reduced gamma shielding that is proposed for AD-1 (see figure 4.2). Particularly, the edges of AD-1 design only has 1 inch of lead versus 3 inches used for P20. It is also worth noting that the MIF was not on for the P20 experiment, so this simulation can inform if the MIF line will require additional shielding when it is active concurrent with PROSPECT data taking.

6.3.1 Singles Rates

The singles spectrum is simply the energy histogram for each event occurring within the full detector. In order to construct this spectrum from simulation, one must take the energy deposited during an ionization event and convert this to a quenched energy corresponding to the average light output of that particle at that energy relative to the light output of an electron depositing the same amount of energy. Quenched energy is then $e_0 * \frac{LO_{particle}}{LO_{electron}}$, where e_0 is the energy deposited by the particle, and LO stands for light output in photons produced.

After the quenched energies are tallied, they are smeared out by Gaussian smearing and position dependent light attenuation to simulate the photons detected by PMTs on either ends of the cell. This step is required because a full optical photon transport model is not implemented for the purpose of this study. Event positions and timing are then reconstructed using this simulated detector response output which are then used for correlating possible neutron capture signals with positron-like energy depositions to determine the IBD signal (see section 6.3.2). Singles rates for the reactor-on and MIF components of the gamma background are shown below. Note that the directionality of the reactor-on component was not taken into account; in the simulation we assumed an isotropic distribution of events entering the detector shielding.

6.3.2 Time Correlated Events

The gamma backgrounds by themselves will not provide an IBD-like signal because gamma energy depositions rarely bleed into the neutron capture PSD box. Because

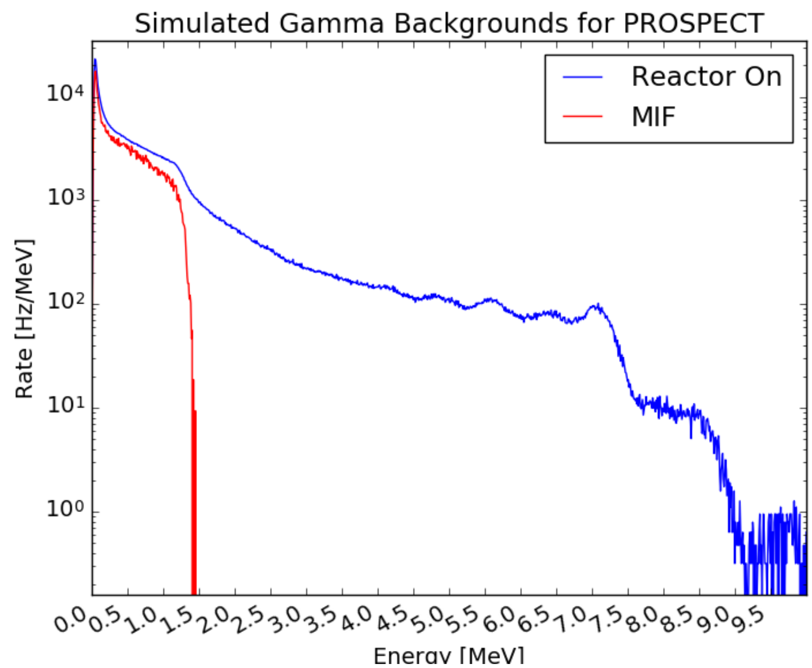

Figure 6.10: Simulated gamma backgrounds for the full AD-1 design, summed over all 158 detector segments. Events in red were simulated using the same MIF generator used to construct figure 6.9. Events in blue were simulated using reactor-on incident gamma spectrum assuming an isotropic distribution incident on the surface of the AD-1 shielding.

IBD candidates are selected from time correlated pairs of energy depositions, where a positron-like signal is detected less than 100 μs before a neutron capture-like signal, we must combine the gamma simulation with the cosmic background simulation and look for coincidences between gamma depositions and particle depositions that fall in the neutron capture window. In order for the event to be positron-like, it must fall within the gamma band. A second order effect not considered is the room neutron background, however shielding is expected to mitigate neutron rates from the room to a level that is orders of magnitude below cosmic background levels. For this reason the room neutron background was not simulated for this first simulation.

The main components of the cosmic background simulation are a neutron and a muon simulation. Both use LLNL's CRY generator[60] for simulating realistic particle momenta and rates. The 2D energy PSD histogram for all depositions

Table 6.1: PROSPECT simulated IBD backgrounds

Simulation	Total IBD Rate [mHz]	Uncertainty [mHz]
Cosmic neutron	4.98	0.26
Cosmic muon	0.82	0.24
Muon accidentals	3.71	0.16
RxOn gamma accidentals	0.01	0.01

from this simulation is shown in figure C.6. Once this simulation is completed, the gamma simulation is combined by doing a time correlation analysis between gamma depositions and the neutron background simulation. Specifically, gamma events that occur within 100 μs before a neutron capture event are tagged as potential IBD candidates. These candidates then go through a series of cuts before they are accepted as an IBD event. The first cut is a shower veto in which events with large multiplicities of gamma depositions in coincidence are rejected as this is a signature of a cosmic ray producing several secondaries which then deposit energy in various parts of detector. The second cut is a topology cut in which events that occur far from the neutron capture are rejected, since positrons tend to deposit their energy within microns of their production point in this liquid scintillator. Finally, a fiducial cut is employed which rejects events occurring in the outer detector layer. The results of these cuts on the reactor-on gamma simulation events coincident with simulated cosmic neutron events can be seen in figure 6.11. See figure C.8 for the same set of cuts applied to the cosmic neutron simulation.

Additionally, the time correlation analysis is done between the cosmic neutron and muon simulations which determines the correlated IBD-like signal rates coming from multiple interactions of the high energy incident cosmic neutron's decay products. The final IBD-like rates from both room gamma coincidences with cosmic backgrounds and correlated signals is shown in table 6.1.

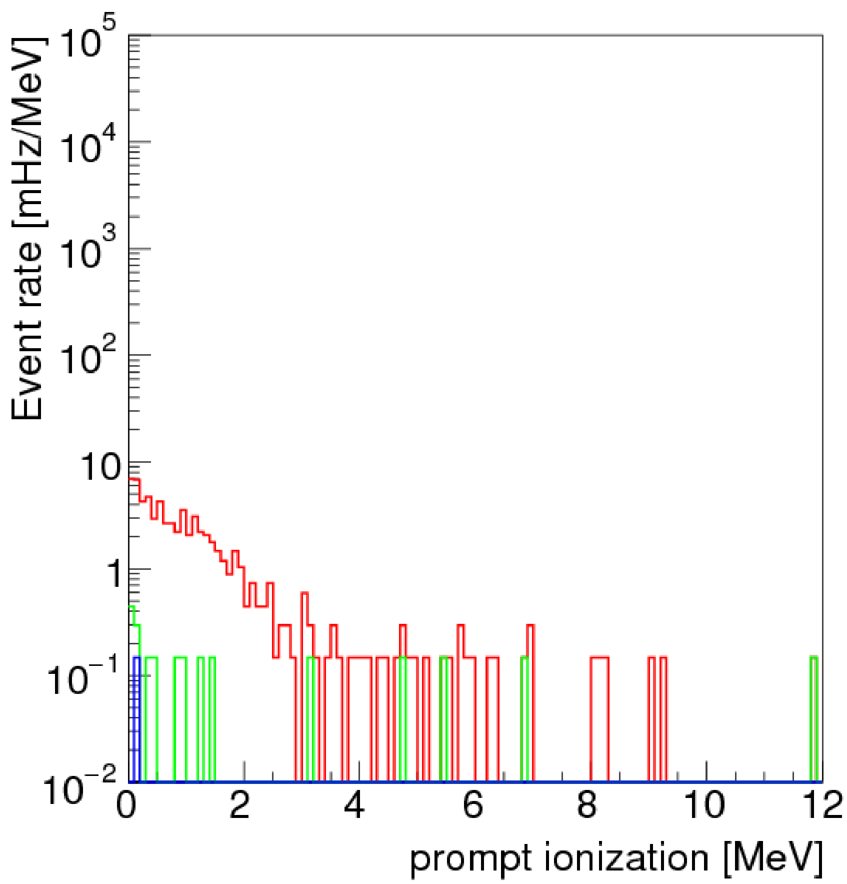

Figure 6.11: Prompt energy spectra for IBD-like events from reactor-on gamma simulation coincident with cosmic neutron simulated events for AD-1. Red are events that pass the shower cut, green are events that pass the shower and topology cut, and blue are events that pass all cuts including the final fiducial cut.

Chapter 7

Conclusions and Future Work

In this chapter we present a short summary of results from the preceding chapters. This includes measured variation of spacial and temporal backgrounds for gammas, fast neutrons, and thermal neutrons at the near and far positions of the PROSPECT AD-1 detector. It also details simulated IBD-like backgrounds in PROSPECT resulting from measured gamma backgrounds. Conclusions based on these studies are drawn and a section detailing future work to improve our modeling of the reactor-correlated backgrounds is given.

7.1 Summary of Results

From our spacial gamma surveys we found that gamma rates vary in a complex fashion throughout the experiment hall depending on the geometry of the monolith, beamlines, and various pipes beneath the room. We found variation in gamma rates between 0.1 MeV and 12.0 MeV of 50% to 175% of the average for the PROSPECT near position while the reactor is on. Similarly, variation between 50% and 210% of the average far position gamma rate between 0.1 MeV and 12.0 MeV were measured during reactor-on. Average reactor-off gamma rates for this energy range were 5% of the average while the reactor is on for the far position and 19% of the average in the near position. Thermal neutrons were also measured across these regions during a reactor-on cycle, finding moderated fluxes of 0.08 to 0.11 Hz/cm^2 in the near position and unmoderated fluxes between 0.15 and 0.25 Hz/cm^2 in the same position. Thermal neutron rates in the far position during reactor-on were between 0.03 and 0.05 Hz/cm^2 moderated and between 0.10 and 0.18 Hz/cm^2 unmoderated.

We found that the gamma rates will vary at a given location in the experiment hall throughout the reactor-on cycle depending on the beam shutter position and spectrometer settings of the beamlines on the floor below the experiment hall. These variations tend to oscillate the rate around 10% of the reactor-on average in the 0.2 to 2.0 MeV range, with as much as a 25% variation around the average for energies greater than 2 MeV. We believe this is attributed to a larger or smaller fraction of neutrons scattering up into the experiment hall depending on beamline HB-3 settings. This is corroborated by large fluctuations in thermal neutron rates seen over the same time period, with variations between 50% and 200% of the average rate measured at a given location.

Simulation of the proposed PROSPECT detector plus shielding package using measured gamma backgrounds during reactor-on conditions without the MIF experiment running finds an IBD-like event 500 times smaller than the event rate from simulated cosmic backgrounds. This confirms that the proposed shielding design will mitigate reactor-correlated backgrounds to acceptable levels.

7.2 Future Work

More work must be done in order to determine the impact of the MIF experiment on the IBD signal, especially since it has a specific directionality to it. This will require a coincidence analysis of MIF gamma produced events with neutron events from the cosmic simulation, as was done for the reactor-on gamma field in section 6.3.2. In the same vein, it should be checked if the directionality of the reactor-correlated gamma background changes the accidental gamma rate.

While directionality is already encoded in our MIF simulation, the directionality of the reactor-on gamma component of the room backgrounds will need to be further studied. If a very detailed simulation of the directionality of room backgrounds is needed, the following procedure can be used to obtain a realistic gamma field in the Geant4 simulation: First, the geometry of the materials surrounding the experiment hall must be encoded in the simulation, focusing on meter-scale structures such as the monolith, large drainage pipes, beamlines, floors, and steel supports. Next, thermal neutron events can be simulated using the measurements shown in figure 4.17. Geant4 will then produce gammas from neutron capture and (n, γ) reactions, and the angular distribution of these gammas entering the experiment hall can then be recorded at discrete segments of the boundaries of the near and far positions. The resulting gamma field can then be simulated positioning the DANG array at the various locations used in the position scans detailed in section 4.5.2, the data from which can be used to validate the directional gamma simulation. Once the directional gamma field has been validated it can then be used to generate events for the simulated PROSPECT detector geometry in order to estimate the reactor-correlated gamma response at a cell-by-cell level.

In order to improve the detector response of the simulated backgrounds, one can use the resolution measurements described in section 5.1.3 to construct distributions of energy resolution vs energy for each detector which can then be fed into the energy smearing portion of the simulation. The current simulation tends to overestimate resolution in lower energy bins and underestimate resolution in higher energy bins, and it also uses the same energy resolution for each detector.

The current "stripping method" used to reconstruct an energy histogram in terms of the simulated gamma responses at incident gamma energies in 20 keV increments can be improved by using any number of chi-squared minimization techniques such as the maximum entropy algorithm used for interpreting sodium iodide spectra as described by J.L. Tain and D. Cano-Ott[70].

In order to further improve the simulation to account for detector dependent efficiencies and resolutions, the efficiency measurements described in section 5.1.5 can be simulated. With efficiency measurements of energies up to 4 MeV, one can use the expected detector responses of the measured gammas to create a curve that approximates the intrinsic efficiency as a function of incident gamma energy for each detector in the array, extrapolating to higher energies that we have no measured efficiencies for. This would be used to correct the reconstructed incident gamma energies for any given measured energy spectrum.

Finally, a more in depth analysis of beam logs given by experimenters using beamline HB-3 and HB-3A needs to be done in order to precisely correlate the jumps in rate seen in the gamma spectra presented in section 4.5.3. Once correlations between beamline activities and rate fluctuations are established, the combination of settings that would produce the largest expected rate in the experiment hall can be requested and measured. Similarly, the combination of settings that would produce the smallest rates can also be requested and measured, establishing limits on the range of gamma and neutron rates achievable at a given location. This would allow for a more precise time-dependent background characterization throughout the duration of PROSPECT's deployment.

7.3 Concluding Remarks

The simulations we have described in this work were done in an approximate manner in order to get a rough estimate of the IBD-like signals that PROSPECT expects from reactor-correlated gamma backgrounds. While more detailed simulation should be done to confirm that the directionality of the gamma field does not dramatically increase the expected background rate from reactor-correlated gammas, our preliminary simulation predicts that this component of the IBD background will be negligible compared to the background induced by cosmic rays. After the construction of the local shield wall and the subsequent decrease in the reactor-correlated gamma rates, it may be that we will not need to subtract out the simulated IBD response from reactor backgrounds as they will fall well below our IBD detection sensitivity.

The position scan data given in this report will inform the design of the local shield wall so as to mitigate the hotspots visible in the data. As the shield wall is constructed, the position scans can be repeated to ensure that these backgrounds are reduced to acceptable levels.

Our characterization and simulation of the nearby MIF experiment in combination with knowledge of typical rate fluctuations throughout a reactor cycle has allowed us to simulate the conditions of the largest reactor backgrounds to which PROSPECT will be exposed throughout its deployment. From this knowledge we have determined that reactor backgrounds can be mitigated to acceptable levels with our current strategy consisting of the construction of a local shield wall within the experiment hall and the assembly of a passive shield wall directly surrounding the active neutrino detecting volume.

Bibliography

[46] (2016). *2M2/2 Bicron Tubes*. http://www.tedss.com/2099001326. 16

[51] (2016a). *76mm (3) tubes*. http://www.isuzuoptics.com.tw/data/product/photonis/pmt/76mm-2.pdf. 19

[37] (2016a). CAEN Electronic Instrumentation Website. 14

[38] (2016b). CAEN V1720 Waveform Digitizer. 14

[39] (2016c). CAEN V1730 Waveform Digitizer. 14

[35] (2016a). Eljen EJ-301 Liquid Scintillator. http://www.eljentechnology.com/products/liquid-scintillators/ej-301-ej-309. Accessed:2016-12-4. 10, 17, 19, 47

[57] (2016b). *Eljen EJ-309 Liquid Scintillator*. http://www.eljentechnology.com/index.php/products/liquid-scintillators/73-ej-309. 23

[34] (2016c). *Eljen EJ-315 Liquid Scintillator*. http://www.eljentechnology.com/products/liquid-scintillators/ej-315. 9, 17, 18

[44] (2016a). *ET Enterprises 9266B series data sheet*. https://my.et-enterprises.com/pdf/9266B.pdf. 16

[47] (2016b). *ET Enterprises 9807B series data sheet*. https://my.et-enterprises.com/pdf/9807B.pdf. 17

[48] (2016c). *ET Enterprises 9821B series data sheet*. https://my.et-enterprises.com/pdf/9821B.pdf. 17

[61] (2016). *Materials Irradiation Facility (MIF) for Materials and Fuels Irradiations*. https://www.ornl.gov/division/rnsd/projects/materials-irradiation-facility-mif-materials-and-fuels-irradiations. 29

[50] (2016). *Model 2006 Proportional Counter Preamplifier*. Accessed:2016-12-4. 18

[45] (2016). *Model 276L*. http://ortec-online.com/download/276L-MNL.pdf. 16

[43] (2016). NaI(Tl) and Polyscin NaI(Tl) Sodium Iodide Scintillation Material . 16

[66] (2016). ROOT TSpectrum Manual. https://root.cern.ch/root/htmldoc/guides/spectrum/Spectrum.pdf. Accessed:2016-12-4. 56

[52] (2016b). *Voltage dividers*. http://www.isuzuoptics.com.tw/data/product/photonis/pmt/voltagedividers.pdf. 19

[56] (2016). *WaterBrick International*. http://www.waterbrick.org. 21

[14] Abazajian, K. N., Acero, M. A., Agarwalla, S. K., Aguilar-Arevalo, A. A., Albright, C. H., Antusch, S., Arguelles, C. A., Balantekin, A. B., Barenboim, G., Barger, V., Bernardini, P., Bezrukov, F., Bjaelde, O. E., Bogacz, S. A., Bowden, N. S., Boyarsky, A., Bravar, A., Bravo Berguno, D., Brice, S. J., Bross, A. D., Caccianiga, B., Cavanna, F., Chun, E. J., Cleveland, B. T., Collin, A. P., Coloma, P., Conrad, J. M., Cribier, M., Cucoanes, A. S., D'Olivo, J. C., Das, S., de Gouvea, A., Derbin, A. V., Dharmapalan, R., Diaz, J. S., Ding, X. J., Djurcic, Z., Donini, A., Duchesneau, D., Ejiri, H., Elliott, S. R., Ernst, D. J., Esmaili, A., Evans, J. J., Fernandez-Martinez, E., Figueroa-Feliciano, E., Fleming, B. T., Formaggio, J. A., Franco, D., Gaffiot, J., Gandhi, R., Gao, Y., Garvey, G. T., Gavrin, V. N., Ghoshal, P., Gibin, D., Giunti, C., Gninenko, S. N., Gorbachev, V. V., Gorbunov, D. S., Guenette, R., Guglielmi, A., Halzen, F., Hamann, J., Hannestad, S., Haxton, W., Heeger, K. M., Henning, R., Hernandez, P., Huber, P., Huelsnitz, W., Ianni, A., Ibragimova, T. V., Karadzhov, Y., Karagiorgi, G., Keefer,

G., Kim, Y. D., Kopp, J., Kornoukhov, V. N., Kusenko, A., Kyberd, P., Langacker, P., Lasserre, T., Laveder, M., Letourneau, A., Lhuillier, D., Li, Y. F., Lindner, M., Link, J. M., Littlejohn, B. L., Lombardi, P., Long, K., Lopez-Pavon, J., Louis, W. C., Ludhova, L., Lykken, J. D., Machado, P. A. N., Maltoni, M., Mann, W. A., Marfatia, D., Mariani, C., Matveev, V. A., Mavromatos, N. E., Melchiorri, A., Meloni, D., Mena, O., Mention, G., Merle, A., Meroni, E., Mezzetto, M., Mills, G. B., Minic, D., Miramonti, L., Mohapatra, D., Mohapatra, R. N., Montanari, C., Mori, Y., Mueller, T. A., Mumm, H. P., Muratova, V., Nelson, A. E., Nico, J. S., Noah, E., Nowak, J., Smirnov, O. Y., Obolensky, M., Pakvasa, S., Palamara, O., Pallavicini, M., Pascoli, S., Patrizii, L., Pavlovic, Z., Peres, O. L. G., Pessard, H., Pietropaolo, F., Pitt, M. L., Popovic, M., Pradler, J., Ranucci, G., Ray, H., Razzaque, S., Rebel, B., Robertson, R. G. H., Rodejohann, W., Rountree, S. D., Rubbia, C., Ruchayskiy, O., Sala, P. R., Scholberg, K., Schwetz, T., Shaevitz, M. H., Shaposhnikov, M., Shrock, R., Simone, S., Skorokhvatov, M., Sorel, M., Sousa, A., Spergel, D. N., Spitz, J., Stanco, L., Stancu, I., Suzuki, A., Takeuchi, T., Tamborra, I., Tang, J., Testera, G., Tian, X. C., Tonazzo, A., Tunnell, C. D., Van de Water, R. G., Verde, L., Veretenkin, E. P., Vignoli, C., Vivier, M., Vogelaar, R. B., Wascko, M. O., Wilkerson, J. F., Winter, W., Wong, Y. Y. Y., Yanagida, T. T., Yasuda, O., Yeh, M., Yermia, F., Yokley, Z. W., Zeller, G. P., Zhan, L., and Zhang, H. (2012). Light Sterile Neutrinos: A White Paper. *ArXiv e-prints*. 2

[23] Abdurashitov, J. N., Veretenkin, E. P., Vermul, V. M., Gavrin, V. N., Girin, S. V., Gorbachev, V. V., Gurkina, P. P., Zatsepin, G. T., Ibragimova, T. V., Kalikhov, A. V., Knodel, T. V., Mirmov, I. N., Khairnasov, N. G., Shikhin, A. A., Yants, V. E., Bowles, T. J., Teasdale, W. A., Nico, J. S., Wilkerson, J. F., Cleveland, B. T., Elliott, S. R., and SAGE Collaboration (2002). Solar neutrino flux measurements by the Soviet-American gallium experiment (SAGE) for half the 22-year solar cycle. *Soviet Journal of Experimental and Theoretical Physics*, 95:181–193. 5

[6] Abe, Y., Aberle, C., Akiri, T., dos Anjos, J. C., Ardellier, F., Barbosa, A. F., Baxter, A., Bergevin, M., Bernstein, A., Bezerra, T. J. C., Bezrukhov, L., Blucher, E., Bongrand, M., Bowden, N. S., Buck, C., Busenitz, J., Cabrera, A., Caden, E., Camilleri, L., Carr, R., Cerrada, M., Chang, P.-J., Chimenti, P., Classen, T., Collin, A. P., Conover, E., Conrad, J. M., Cormon, S., Crespo-Anadón, J. I., Cribier, M., Crum, K., Cucoanes, A., D'Agostino, M. V., Damon, E., Dawson, J. V., Dazeley, S., Dierckxsens, M., Dietrich, D., Djurcic, Z., Dracos, M., Durand, V., Efremenko, Y., Elnimr, M., Endo, Y., Etenko, A., Falk, E., Fallot, M., Fechner, M., von Feilitzsch, F., Felde, J., Fernandes, S. M., Franco, D., Franke, A. J., Franke, M., Furuta, H., Gama, R., Gil-Botella, I., Giot, L., Göger-Neff, M., Gonzalez, L. F. G., Goodman, M. C., Goon, J. T., Greiner, D., Guillon, B., Haag, N., Hagner, C., Hara, T., Hartmann, F. X., Hartnell, J., Haruna, T., Haser, J., Hatzikoutelis, A., Hayakawa, T., Hofmann, M., Horton-Smith, G. A., Ishitsuka, M., Jochum, J., Jollet, C., Jones, C. L., Kaether, F., Kalousis, L., Kamyshkov, Y., Kaplan, D. M., Kawasaki, T., Keefer, G., Kemp, E., de Kerret, H., Kibe, Y., Konno, T., Kryn, D., Kuze, M., Lachenmaier, T., Lane, C. E., Langbrandtner, C., Lasserre, T., Letourneau, A., Lhuillier, D., Lima, Jr., H. P., Lindner, M., Liu, Y., López-Castanõ, J. M., LoSecco, J. M., Lubsandorzhiev, B. K., Lucht, S., McKee, D., Maeda, J., Maesano, C. N., Mariani, C., Maricic, J., Martino, J., Matsubara, T., Mention, G., Meregaglia, A., Miletic, T., Milincic, R., Milzstajn, A., Miyata, H., Motta, D., Mueller, T. A., Nagasaka, Y., Nakajima, K., Novella, P., Obolensky, M., Oberauer, L., Onillon, A., Osborn, A., Ostrovskiy, I., Palomares, C., Peeters, S. J. M., Pepe, I. M., Perasso, S., Perrin, P., Pfahler, P., Porta, A., Potzel, W., Queval, R., Reichenbacher, J., Reinhold, B., Remoto, A., Reyna, D., Röhling, M., Roth, S., Rubin, H. A., Sakamoto, Y., Santorelli, R., Sato, F., Schönert, S., Schoppmann, S., Schwan, U., Schwetz, T., Shaevitz, M. H., Shrestha, D., Sida, J.-L., Sinev, V., Skorokhvatov, M., Smith, E., Spitz, J., Stahl, A., Stancu, I., Strait, M., Stüken, A., Suekane, F., Sukhotin, S., Sumiyoshi, T., Sun, Y., Sun, Z., Svoboda, R., Tabata, H., Tamura, N., Terao, K., Tonazzo, A., Toups, M., Trinh

Thi, H. H., Veyssiere, C., Wagner, S., Watanabe, H., White, B., Wiebusch, C., Winslow, L., Worcester, M., Wurm, M., Yanovitch, E., Yermia, F., Zbiri, K., and Zimmer, V. (2012). Indication of Reactor ν_e Disappearance in the Double Chooz Experiment. *Physical Review Letters*, 108(13):131801. 2, 6

[32] Achkar, B., Aleksan, R., Avenier, M., Bagieu, G., Bouchez, J., Brissot, R., Cavaignac, J.-F., Collot, J., Cousinou, M.-C., Cussonneau, J. P., Declais, Y., Dufour, Y., Favier, J., Garciaz, F., Kajfasz, E., de Kerret, H., Koang, D. H., Lefièvre, B., Lesquoy, E., Mallet, J., Metref, A., Nagy, E., Pessard, H., Pierre, F., Obolensky, M., Stutz, A., and Wuthrick, J. P. (1995). Search for neutrino oscillations at 15, 40 and 95 meters from a nuclear power reactor at Bugey. *Nuclear Physics B*, 434:503–532. 6

[19] Adam, T., Agafonova, N., Aleksandrov, A., Altinok, O., Alvarez Sanchez, P., Anokhina, A., Aoki, S., Ariga, A., Ariga, T., Autiero, D., Badertscher, A., Ben Dhahbi, A., Bertolin, A., Bozza, C., Brugière, T., Brugnera, R., Brunet, F., Brunetti, G., Buontempo, S., Carlus, B., Cavanna, F., Cazes, A., Chaussard, L., Chernyavsky, M., Chiarella, V., Chukanov, A., Colosimo, G., Crespi, M., D'Ambrosio, N., De Lellis, G., De Serio, M., Déclais, Y., del Amo Sanchez, P., Di Capua, F., Di Crescenzo, A., Di Ferdinando, D., Di Marco, N., Dmitrievsky, S., Dracos, M., Duchesneau, D., Dusini, S., Dzhatdoev, T., Ebert, J., Efthymiopoulos, I., Egorov, O., Ereditato, A., Esposito, L. S., Favier, J., Ferber, T., Fini, R. A., Fukuda, T., Garfagnini, A., Giacomelli, G., Giorgini, M., Giovannozzi, M., Girerd, C., Goldberg, J., Göllnitz, C., Golubkov, D., Goncharova, L., Gornushkin, Y., Grella, G., Grianti, F., Gschwendtner, E., Guerin, C., Guler, A. M., Gustavino, C., Hagner, C., Hamada, K., Hara, T., Enikeev, R., Hierholzer, M., Hollnagel, A., Ieva, M., Ishida, H., Ishiguro, K., Jakovcic, K., Jollet, C., Jones, M., Juget, F., Kamiscioglu, M., Kawada, J., Kim, S. H., Kimura, M., Kiritsis, E., Kitagawa, N., Klicek, B., Knuesel, J., Kodama, K., Komatsu, M., Kose, U., Kreslo, I., Lazzaro, C., Lenkeit, J., Ljubicic, A., Longhin, A., Malgin, A., Mandrioli, G., Marteau,

J., Matsuo, T., Matveev, V., Mauri, N., Mazzoni, A., Medinaceli, E., Meisel, F., Meregaglia, A., Migliozzi, P., Mikado, S., Missiaen, D., Monacelli, P., Morishima, K., Moser, U., Muciaccia, M. T., Naganawa, N., Naka, T., Nakamura, M., Nakano, T., Nakatsuka, Y., Naumov, D., Nikitina, V., Nitti, F., Ogawa, S., Okateva, N., Olchevsky, A., Palamara, O., Paoloni, A., Park, B. D., Park, I. G., Pastore, A., Patrizii, L., Pennacchio, E., Pessard, H., Pistillo, C., Polukhina, N., Pozzato, M., Pretzl, K., Pupilli, F., Rescigno, R., Riguzzi, F., Roganova, T., Rokujo, H., Rosa, G., Rostovtseva, I., Rubbia, A., Russo, A., Ryasny, V., Ryazhskaya, O., Sato, O., Sato, Y., Sahnoun, Z., Schembri, A., Schuler, J., Scotto Lavina, L., Serrano, J., Shakiryanova, I., Sheshukov, A., Shibuya, H., Shoziyoev, G., Simone, S., Sioli, M., Sirignano, C., Sirri, G., Song, J. S., Spinetti, M., Stanco, L., Starkov, N., Stellacci, S., Stipcevic, M., Strauss, T., Takahashi, S., Tenti, M., Terranova, F., Tezuka, I., Tioukov, V., Tolun, P., Trani, N. T., Tufanli, S., Vilain, P., Vladimirov, M., Votano, L., Vuilleumier, J.-L., Wilquet, G., Wonsak, B., Wurtz, J., Yakushev, V., Yoon, C. S., Yoshida, J., Zaitsev, Y., Zemskova, S., and Zghiche, A. (2012). Measurement of the neutrino velocity with the OPERA detector in the CNGS beam. *Journal of High Energy Physics*, 10:93. 5

[59] Agostinelli, S. et al. (2003). GEANT4: A Simulation toolkit. *Nuclear Instruments and Methods*, A506:250–303. 27, 64

[5] Ahn, J. K., Chebotaryov, S., Choi, J. H., Choi, S., Choi, W., Choi, Y., Jang, H. I., Jang, J. S., Jeon, E. J., Jeong, I. S., Joo, K. K., Kim, B. R., Kim, B. C., Kim, H. S., Kim, J. Y., Kim, S. B., Kim, S. H., Kim, S. Y., Kim, W., Kim, Y. D., Lee, J., Lee, J. K., Lim, I. T., Ma, K. J., Pac, M. Y., Park, I. G., Park, J. S., Park, K. S., Shin, J. W., Siyeon, K., Yang, B. S., Yeo, I. S., Yi, S. H., and Yu, I. (2012). Observation of Reactor Electron Antineutrinos Disappearance in the RENO Experiment. *Physical Review Letters*, 108(19):191802. 2, 6

[18] Alspector, J., Kalbfleisch, G. R., Baggett, N., Fowler, E. C., Barish, B. C., Bodek, A., Buchholz, D., Sciulli, F. J., Siskind, E. J., Stutte, L., Fisk, H. E., Krafczyk,

G., Nease, D. L., and Fackler, O. D. (1976). Experimental Comparison of Neutrino and Muon Velocities. *Physical Review Letters*, 36:837–840. 5

[54] An, F., An, G., An, Q., Antonelli, V., Baussan, E., Beacom, J., Bezrukov, L., Blyth, S., Brugnera, R., Buizza Avanzini, M., Busto, J., Cabrera, A., Cai, H., Cai, X., Cammi, A., Cao, G., Cao, J., Chang, Y., Chen, S., Chen, S., Chen, Y., Chiesa, D., Clemenza, M., Clerbaux, B., Conrad, J., D'Angelo, D., De Kerret, H., Deng, Z., Deng, Z., Ding, Y., Djurcic, Z., Dornic, D., Dracos, M., Drapier, O., Dusini, S., Dye, S., Enqvist, T., Fan, D., Fang, J., Favart, L., Ford, R., Göger-Neff, M., Gan, H., Garfagnini, A., Giammarchi, M., Gonchar, M., Gong, G., Gong, H., Gonin, M., Grassi, M., Grewing, C., Guan, M., Guarino, V., Guo, G., Guo, W., Guo, X.-H., Hagner, C., Han, R., He, M., Heng, Y., Hsiung, Y., Hu, J., Hu, S., Hu, T., Huang, H., Huang, X., Huo, L., Ioannisian, A., Jeitler, M., Ji, X., Jiang, X., Jollet, C., Kang, L., Karagounis, M., Kazarian, N., Krumshteyn, Z., Kruth, A., Kuusiniemi, P., Lachenmaier, T., Leitner, R., Li, C., Li, J., Li, W., Li, W., Li, X., Li, X., Li, Y., Li, Y., Li, Z.-B., Liang, H., Lin, G.-L., Lin, T., Lin, Y.-H., Ling, J., Lippi, I., Liu, D., Liu, H., Liu, H., Liu, J., Liu, J., Liu, J., Liu, Q., Liu, S., Liu, S., Lombardi, P., Long, Y., Lu, H., Lu, J., Lu, J., Lu, J., Lubsandorzhiev, B., Ludhova, L., Luo, S., Lyashuk, V., Möllenberg, R., Ma, X., Mantovani, F., Mao, Y., Mari, S. M., McDonough, W. F., Meng, G., Meregaglia, A., Meroni, E., Mezzetto, M., Miramonti, L., Mueller, T., Naumov, D., Oberauer, L., Ochoa-Ricoux, J. P., Olshevskiy, A., Ortica, F., Paoloni, A., Peng, H., Peng, J.-C., Previtali, E., Qi, M., Qian, S., Qian, X., Qian, Y., Qin, Z., Raffelt, G., Ranucci, G., Ricci, B., Robens, M., Romani, A., Ruan, X., Ruan, X., Salamanna, G., Shaevitz, M., Sinev, V., Sirignano, C., Sisti, M., Smirnov, O., Soiron, M., Stahl, A., Stanco, L., Steinmann, J., Sun, X., Sun, Y., Taichenachev, D., Tang, J., Tkachev, I., Trzaska, W., van Waasen, S., Volpe, C., Vorobel, V., Votano, L., Wang, C.-H., Wang, G., Wang, H., Wang, M., Wang, R., Wang, S., Wang, W., Wang, Y., Wang, Y., Wang, Y., Wang, Z., Wang, Z., Wang, Z., Wang, Z., Wei, W., Wen, L., Wiebusch, C., Wonsak, B.,

Wu, Q., Wulz, C.-E., Wurm, M., Xi, Y., Xia, D., Xie, Y., Xing, Z.-z., Xu, J., Yan, B., Yang, C., Yang, C., Yang, G., Yang, L., Yang, Y., Yao, Y., Yegin, U., Yermia, F., You, Z., Yu, B., Yu, C., Yu, Z., Zavatarelli, S., Zhan, L., Zhang, C., Zhang, H.-H., Zhang, J., Zhang, J., Zhang, Q., Zhang, Y.-M., Zhang, Z., Zhao, Z., Zheng, Y., Zhong, W., Zhou, G., Zhou, J., Zhou, L., Zhou, R., Zhou, S., Zhou, W., Zhou, X., Zhou, Y., Zhou, Y., and Zou, J. (2016). Neutrino physics with JUNO. *Journal of Physics G Nuclear Physics*, 43(3):030401. 20

[4] An, F. P., Bai, J. Z., Balantekin, A. B., Band, H. R., Beavis, D., Beriguete, W., Bishai, M., Blyth, S., Boddy, K., Brown, R. L., and et al. (2012). Observation of Electron-Antineutrino Disappearance at Daya Bay. *Physical Review Letters*, 108(17):171803. 2, 6

[42] Anger, H. O. and Davis, D. H. (1964). Gamma-Ray Detection Efficiency and Image Resolution in Sodium Iodide. *Review of Scientific Instruments*, 35:693–697. 15

[3] Ashenfelter, J., Balantekin, B., Baldenegro, C. X., Band, H. R., Barclay, G., Bass, C. D., Berish, D., Bowden, N. S., Bryan, C. D., Cherwinka, J. J., Chu, R., Classen, T., Davee, D., Dean, D., Deichert, G., Dolinski, M. J., Dolph, J., Dwyer, D. A., Fan, S., Gaison, J. K., Galindo-Uribarri, A., Gilje, K., Glenn, A., Green, M., Han, K., Hans, S., Heeger, K. M., Heffron, B., Jaffe, D. E., Kettell, S., Langford, T. J., Littlejohn, B. R., Martinez, D., McKeown, R. D., Morrell, S., Mueller, P. E., Mumm, H. P., Napolitano, J., Norcini, D., Pushin, D., Romero, E., Rosero, R., Saldana, L., Seilhan, B. S., Sharma, R., Stemen, N. T., Surukuchi, P. T., Thompson, S. J., Varner, R. L., Wang, W., Watson, S. M., White, B., White, C., Wilhelmi, J., Williams, C., Wise, T., Yao, H., Yeh, M., Yen, Y.-R., Zhang, C., and Zhang, X. (2016). Background radiation measurements at high power research reactors. *Nuclear Instruments and Methods in Physics Research A*, 806:401–419. 1, 25

[33] Ashenfelter, J., Balantekin, B., Band, H., Barclay, G., Bass, C., Berish, D., Bowden, N., Bowes, A., Brodsky, J., Bryan, C., Cherwinka, J., Chu, R., Classen, T., Commeford, K., Davee, D., Dean, D., Deichert, G., Diwan, M., Dolinski, M., Dolph, J., Dwyer, D., Gaison, J., Galindo-Uribarri, A., Gilje, K., Glenn, A., Goddard, B., Green, M., Han, K., Hans, S., Heeger, K., Heffron, B., Jaffe, D., Langford, T., Littlejohn, B., Caicedo, D. M., McKeown, R., Mendenhall, M., Mueller, P., Mumm, H., Napolitano, J., Neilson, R., Norcini, D., Pushin, D., Qian, X., Romero, E., Rosero, R., Saldana, L., Seilhan, B., Sharma, R., Sheets, S., Stemen, N., Surukuchi, P., Varner, R., Viren, B., Wang, W., White, B., White, C., Wilhelmi, J., Williams, C., Wise, T., Yao, H., Yeh, M., Yen, Y., Zangakis, G., Zhang, C., and Zhang, X. (2015). Light collection and pulse-shape discrimination in elongated scintillator cells for the PROSPECT reactor antineutrino experiment. *Journal of Instrumentation*, 10(11):P11004. 9, 13

[1] Ashenfelter, J. et al. (2016). The PROSPECT Physics Program. *J. Phys.*, G43(11):113001. xii, xiv, 1, 8, 20, 22, 23, 24, 26, 27, 28, 32, 99, 100

[62] Brun, R. and Rademakers, F. (1997). ROOT - An Object Oriented Data Analysis Framework. *Nuclear Instrumentation Methods*, A389:81 – 86. 49

[69] Chadwick, M., Herman, M., Obložinský, P., Dunn, M., Danon, Y., Kahler, A., Smith, D., Pritychenko, B., Arbanas, G., Arcilla, R., Brewer, R., Brown, D., Capote, R., Carlson, A., Cho, Y., Derrien, H., Guber, K., Hale, G., Hoblit, S., Holloway, S., Johnson, T., Kawano, T., Kiedrowski, B., Kim, H., Kunieda, S., Larson, N., Leal, L., Lestone, J., Little, R., McCutchan, E., MacFarlane, R., MacInnes, M., Mattoon, C., McKnight, R., Mughabghab, S., Nobre, G., Palmiotti, G., Palumbo, A., Pigni, M., Pronyaev, V., Sayer, R., Sonzogni, A., Summers, N., Talou, P., Thompson, I., Trkov, A., Vogt, R., van der Marck, S., Wallner, A., White, M., Wiarda, D., and Young, P. (2011). ENDF/B-VII.1 nuclear data for science and technology: Cross sections, covariances, fission product yields and

decay data. *Nuclear Data Sheets*, 112(12):2887 – 2996. Special Issue on ENDF/B-VII.1 Library. 71

[20] Davis, R., Harmer, D. S., and Hoffman, K. C. (1968). Search for Neutrinos from the Sun. *Physical Review Letters*, 20:1205–1209. 5

[29] Derbin, A. I., Chernyĭ, A. V., Popeko, L. A., Muratova, V. N., Shishkina, G. A., and Bakhlanov, S. I. (1993). Experiment on antineutrino scattering by electrons at a reactor of the Rovno nuclear power plant. *Soviet Journal of Experimental and Theoretical Physics Letters*, 57:768. 6

[68] Febbraro, M., Lawrence, C. C., Zhu, H., Pierson, B., Torres-Isea, R. O., Becchetti, F. D., Kolata, J. J., and Riggins, J. (2015). Deuterated scintillators and their application to neutron spectroscopy. *Nuclear Instruments and Methods in Physics Research A*, 784:184–188. 59

[58] Fisher, B. M., Abdurashitov, J. N., Coakley, K. J., Gavrin, V. N., Gilliam, D. M., Nico, J. S., Shikhin, A. A., Thompson, A. K., Vecchia, D. F., and Yants, V. E. (2011). Fast neutron detection with ^{6}Li-loaded liquid scintillator. *Nuclear Instruments and Methods in Physics Research A*, 646:126–134. 23

[13] Giunti, C. (2016). Precise Determination of the U-235 Reactor Antineutrino Cross Section per Fission. *ArXiv e-prints*. 2

[31] Greenwood, Z. D., Kropp, W. R., Mandelkern, M. A., Nakamura, S., Pasierb-Love, E. L., Price, L. R., Reines, F., Riley, S. P., Sobel, H. W., Baumann, N., and Gurr, H. S. (1996). Results of a two-position reactor neutrino-oscillation experiment. , 53:6054–6064. 6

[36] Grupen, C. and Buvat, I. (2012). *Handbook of Particle Detection and Imaging*. Springer. 13, 15

[10] Haag, N., Gelletly, W., von Feilitzsch, F., Oberauer, L., Potzel, W., Schreckenbach, K., and Sonzogni, A. A. (2014). Re-publication of the data from

the BILL magnetic spectrometer: The cumulative β spectra of the fission products of ^{235}U, ^{239}Pu, and ^{241}Pu. *ArXiv e-prints*. 2

[60] Hagmann, C., Lange, D., and Wright, D. (2007). Cosmic-ray shower generator (CRY) for Monte Carlo transport codes. In *Nuclear Science Symposium Conference Record*, volume 2, pages 1143–1146. IEEE. 27, 71, 76

[22] Hampel, W., Handt, J., Heusser, G., Kiko, J., Kirsten, T., Laubenstein, M., Pernicka, E., Rau, W., Wojcik, M., Zakharov, Y., von Ammon, R., Ebert, K. H., Fritsch, T., Heidt, D., Henrich, E., Stieglitz, L., Weirich, F., Balata, M., Sann, M., Hartmann, F. X., Bellotti, E., Cattadori, C., Cremonesi, O., Ferrari, N., Fiorini, E., Zanotti, L., Altmann, M., von Feilitzsch, F., Mössbauer, R., Wanninger, S., Berthomieu, G., Schatzman, E., Carmi, I., Dostrovsky, I., Bacci, C., Belli, P., Bernabei, R., D'Angelo, S., Paoluzi, L., Cribier, M., Rich, J., Spiro, M., Tao, C., Vignaud, D., Boger, J., Hahn, R. L., Rowley, J. K., Stoenner, R. W., and Weneser, J. (1999). GALLEX solar neutrino observations: results for GALLEX IV. *Physics Letters B*, 447:127–133. 5

[11] Hayes, A. C., Friar, J. L., Garvey, G. T., Ibeling, D., Jungman, G., Kawano, T., and Mills, R. W. (2015). Possible origins and implications of the shoulder in reactor neutrino spectra. , 92(3):033015. 2, 6

[26] Hayes, A. C. and Vogel, P. (2016). Reactor Neutrino Spectra. *ArXiv e-prints*. 6

[55] Hélaine, V. (2016). Sterile neutrino search at the ILL nuclear reactor: the STEREO experiment. *ArXiv e-prints*. 20

[21] Hirata, K. S., Kajita, T., Kifune, K., Kihara, K., and Nakahata, M. (1989). Observation of B-8 solar neutrinos in the Kamiokande-II detector. *Physical Review Letters*, 63:16–19. 5

[27] Huber, P. (2011). Determination of antineutrino spectra from nuclear reactors. , 84(2):024617. 6

[12] Huber, P. (2016). The 5 MeV bump - a nuclear whodunit mystery. *ArXiv e-prints*. 2

[40] Karny, M., Rykaczewski, K. P., Fijałkowska, A., Rasco, B. C., Wolińska-Cichocka, M., Grzywacz, R. K., Goetz, K. C., Miller, D., and Zganjar, E. F. (2016). Modular total absorption spectrometer. *Nuclear Instruments and Methods in Physics Research A*, 836:83–90. 15

[67] Knoll, G. F. (2000). *Radiation detection and measurement*. Wiley. 59

[53] Ko, Y. J., Kim, B. R., Kim, J. Y., Han, B. Y., Jang, C. H., Jeon, E. J., Joo, K. K., Kim, H. J., Kim, H. S., Kim, Y. D., Lee, J., Lee, J. Y., Lee, M. H., Oh, Y. M., Park, H. K., Park, H. S., Park, K. S., Seo, K. M., Siyeon, K., and Sun, G. M. (2016). A sterile neutrino search at NEOS Experiment. *ArXiv e-prints*. 20

[15] Kopp, J., Machado, P. A. N., Maltoni, M., and Schwetz, T. (2013). Sterile neutrino oscillations: the global picture. *Journal of High Energy Physics*, 5:50. 2, 6

[64] Liu, Y., Li, H., Wang, Y., Xing, T., Xie, S., Uribe, J., Baghaei, H., Ramirez, R., Kim, S., and Wong, W.-H. (2004). A Gain-Programmable Transit-Time-Stable and Temperature-Stable PMT Voltage Divider. *IEEE Transactions on Nuclear Science*, 51:2558–2562. 52

[30] Martemyanov, V. P., Mikaelyan, L. A., Sinev, V. V., Kopeikin, V. I., and Kozlov, Y. V. (2003). The Kr2Det project: Search for mass-3 state contribution —U_{e3}——^{2} to the electron neutrino using a one-reactor-two-detector oscillation experiment at the krasnoyarsk underground site. *Physics of Atomic Nuclei*, 66:1934–1939. 6

[65] Matta, J. T. (2016). DAQ ORCHID. private communication. 55, 57

[49] Mazed, D., Mameri, S., and Ciolini, R. (2012). Design parameters and technology optimization of 3he-filled proportional counters for thermal neutron detection and spectrometry applications. *Radiation Measurements*, 47(8):577 – 587. 18

[8] Mention, G., Fechner, M., Lasserre, T., Mueller, T. A., Lhuillier, D., Cribier, M., and Letourneau, A. (2011). Reactor antineutrino anomaly. , 83(7):073006. 2, 6

[25] Metcalf, W. J. (1996). Evidence for Neutrino Oscillations from the LSND Experiment. In *APS Southeastern Section Meeting Abstracts*. 5

[7] Mueller, T. A., Lhuillier, D., Fallot, M., Letourneau, A., Cormon, S., Fechner, M., Giot, L., Lasserre, T., Martino, J., Mention, G., Porta, A., and Yermia, F. (2011). Improved predictions of reactor antineutrino spectra. , 83(5):054615. 2, 6

[2] Oak Ridge National Laboratory (2016). The High-Flux Isotope Reactor at ORNL. 1, 25

[16] Palazzo, A. (2016). Sterile Neutrinos. *Journal of Physics Conference Series*, 718(2):022015. 2

[63] Pringle, R. W. and Standil, S. (1950). The gamma-rays from neutron-activated gold. *Physical Review*, 80:762–763. 50

[17] Reines, F. and Cowan, C. L. (1953). Detection of the Free Neutrino. *Physical Review*, 92:830–831. 5

[41] Sabharwal, S., Kathuria, S., and Ghosh, B. (1985). Thermoluminescence in gamma-irradiated nai(tl) crystal. *Nuclear Tracks and Radiation Measurements (1982)*, 10(1):107 – 110. 15

[24] Schechter, J. and Valle, J. W. F. (1980). Neutrino masses in SU(2) $\otimes U(1) theories., 22 : 2227 - -2235.$ 5

[9] Schreckenbach, K., Faust, H. R., von Feilitzsch, F., Hahn, A. A., Hawerkamp, K., and Vuilleumier, J. L. (1981). Absolute measurement of the beta spectrum from ^{235}U fission as a basis for reactor antineutrino experiments. *Physics Letters B*, 99:251–256. 2, 6

[70] Tain, J. and Cano-Ott, D. (2007). Algorithms for the analysis of -decay total absorption spectra. *Nuclear Instruments and Methods in Physics Research Section A: Accelerators, Spectrometers, Detectors and Associated Equipment*, 571(3):728 – 738. 82

[28] Zacek, G., Feilitzsch, F. V., Mössbauer, R. L., Oberauer, L., Zacek, A. V., Boehm, F., Fisher, P. H., Gimlett, J. L., Hahn, A. A., Henrikson, H. E., Kwon, H., Vuilleumier, J. L., and Gabathuler, K. (1986). Neutrino-oscillation experiments at the Gösgen nuclear power reactor. , 34:2621–2636. 6

Appendix

Appendix A

PROSPECT Sensitivity

Below are sensitivity curves based on projected baseline coverage for the AD-1 design of PROSPECT. These were produced assuming the center of the near position at 7 meters from the core, the center of the far position at 12 meters from the core, and a position resolution of the width of a single cell (each cell is 14.6 cm x 14.6 cm).

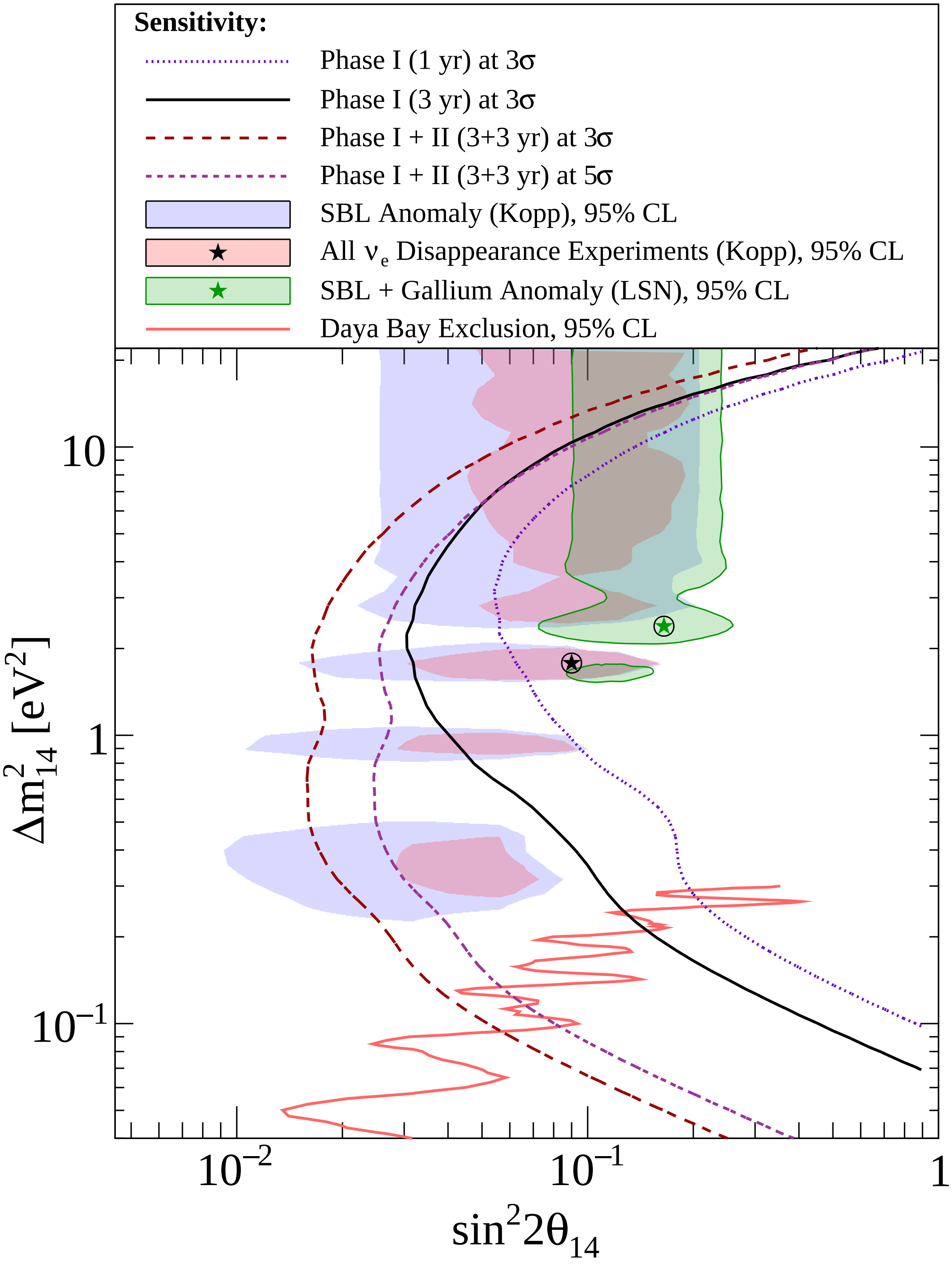

Figure A.1: PROSPECT's sensitivity to $\sin^2 2\theta_{14}$, Δm^2_{14} for both phase I and phase II at different levels of statistics[1].

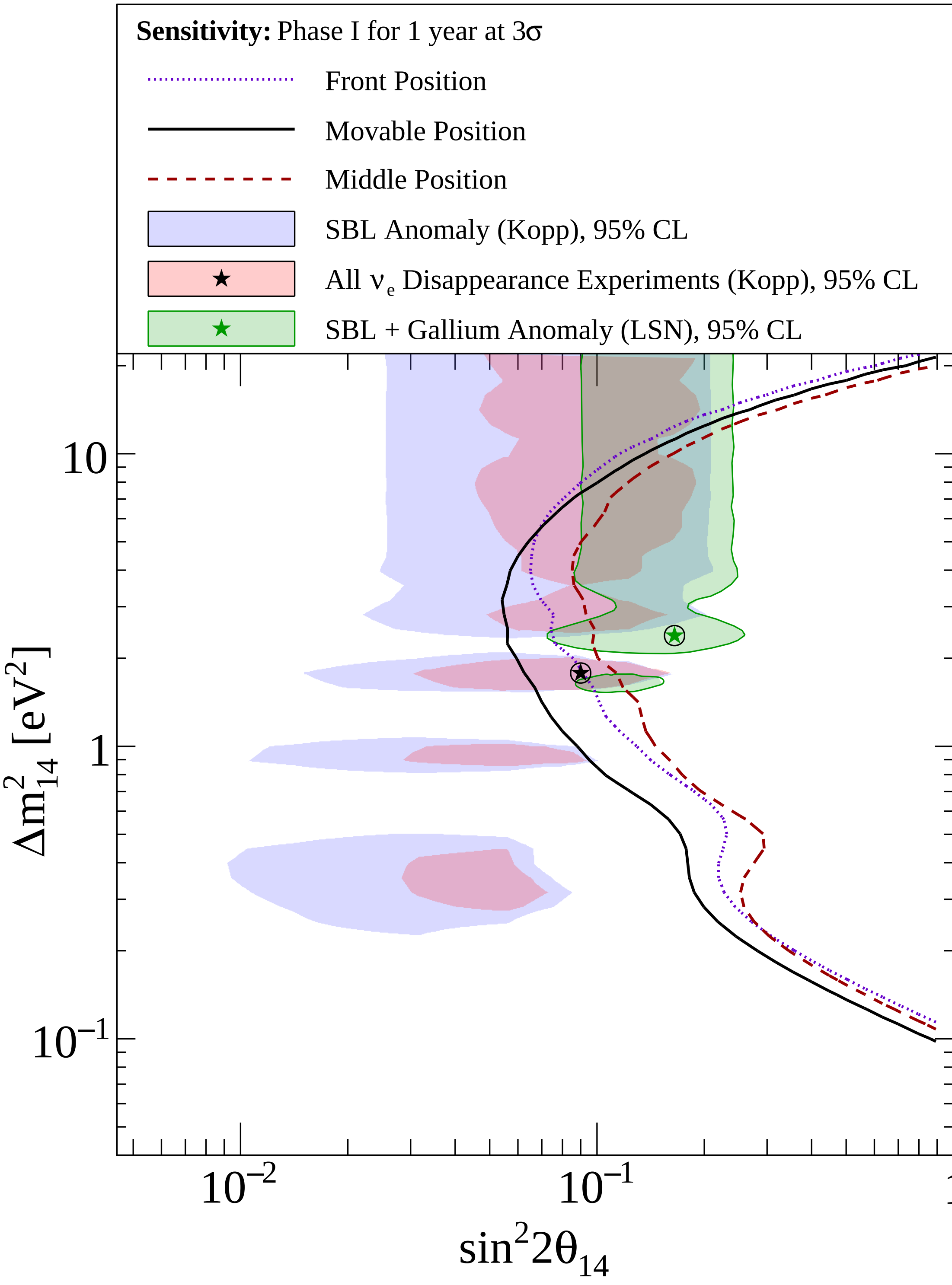

Figure A.2: PROSPECT's sensitivity to $\sin^2 2\theta_{14}$, Δm^2_{14} for phase I at different position options, including a movable option which splits time in both front and middle position[1].

Appendix B

Additional Position Scan Figures

This chapter includes additional figures for the position scans performed with DANG. This includes the reactor-on position scan for energies between 3 and 5 MeV which is useful for visualizing the contribution from the beamlines below, as the 1 to 3 MeV plots are dominated by the MIF. Also included are reactor-off gammas between 1 and 3 MeV, reactor-off gammas between 3 and 5 MeV, and reactor-off thermal neutrons.

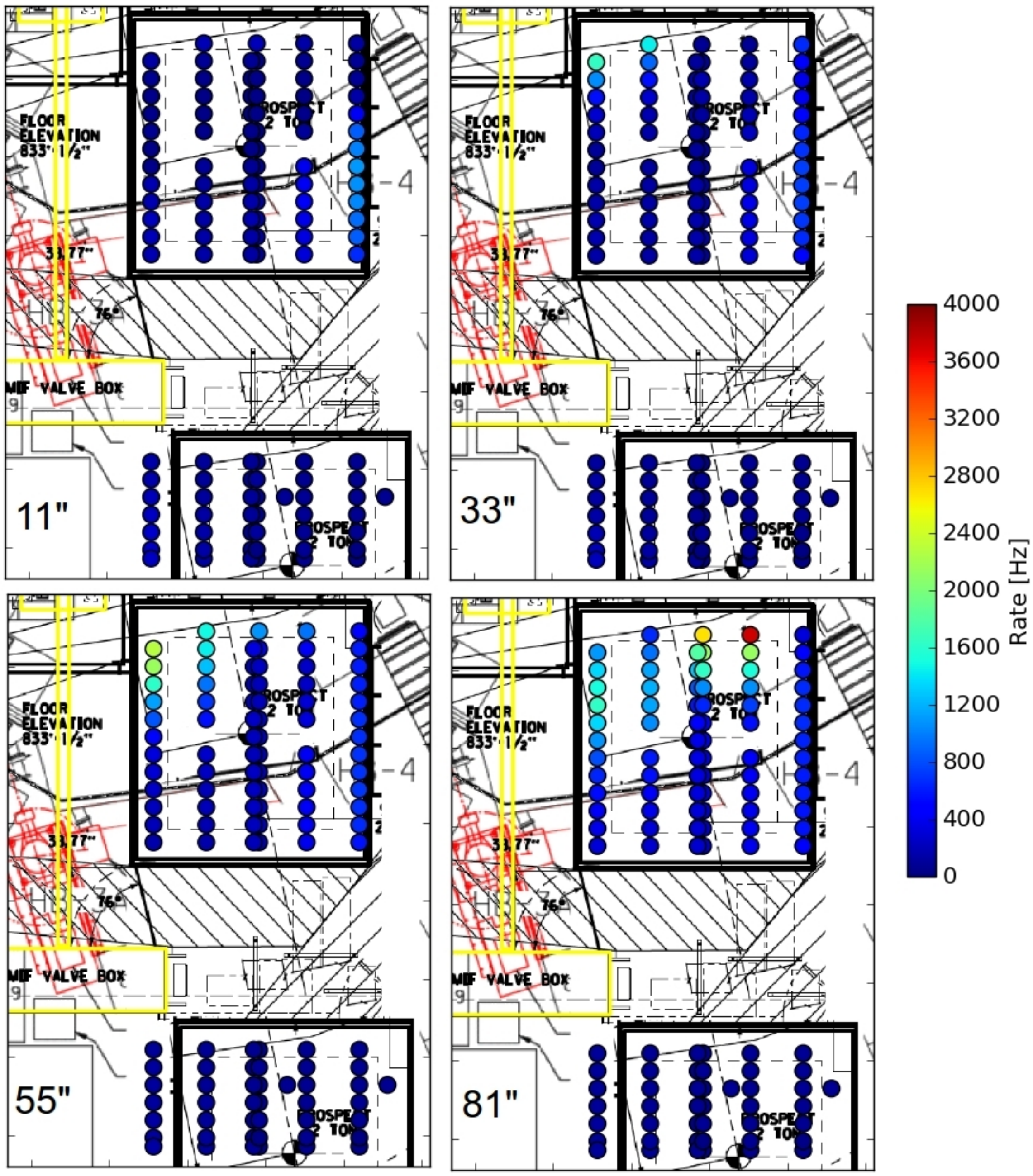

Figure B.1: 2" x 4" x 16" NaI gamma rates (Hz) for energy depositions between 3 and 5 MeV at different positions throughout the planned near and far positions of PROSPECT during reactor-on. Displayed are rates at 4 different heights above the floor: 11" (top-left), 33" (top-right), 55" (bottom-left), and 81" (bottom-right).

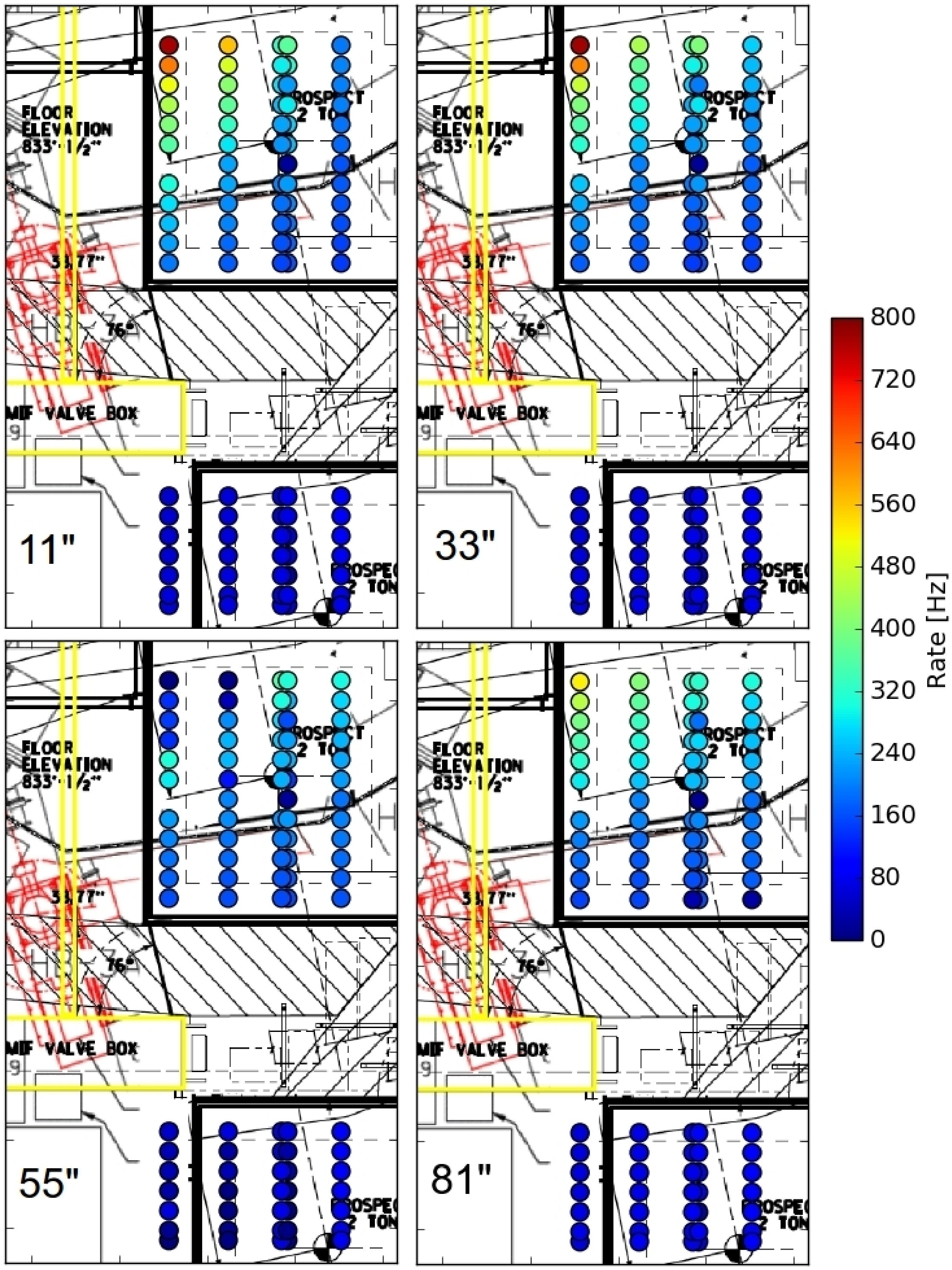

Figure B.2: 2" x 4" x 16" NaI gamma rates (Hz) for energy depositions between 1 and 3 MeV at different positions throughout the planned near and far positions of PROSPECT during reactor-off. Displayed are rates at 4 different heights above the floor: 11" (top-left), 33" (top-right), 55" (bottom-left), and 81" (bottom-right).

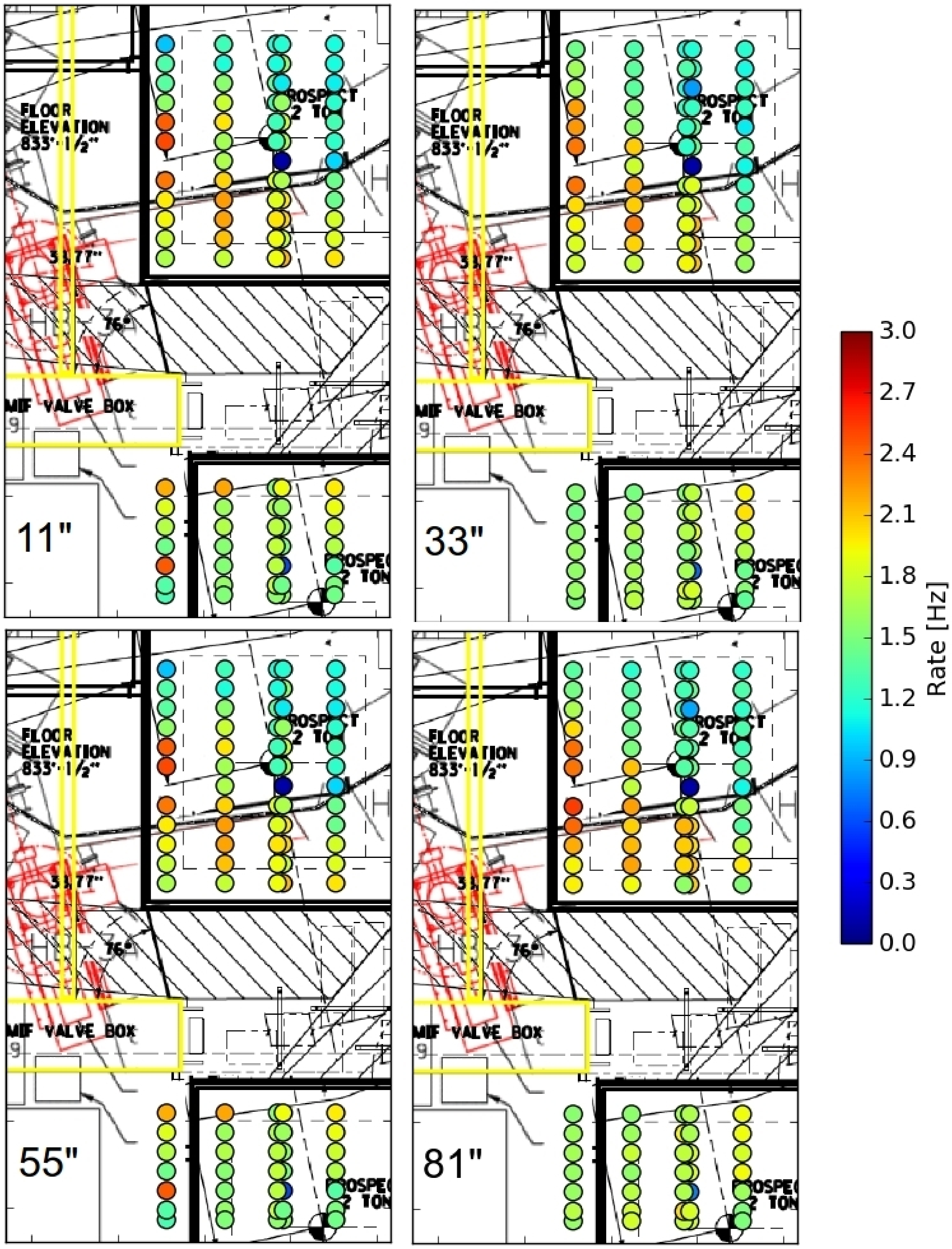

Figure B.3: 2" x 4" x 16" NaI gamma rates (Hz) for energy depositions between 3 and 5 MeV at different positions throughout the planned near and far positions of PROSPECT during reactor-off. Displayed are rates at 4 different heights above the floor: 11" (top-left), 33" (top-right), 55" (bottom-left), and 81" (bottom-right).

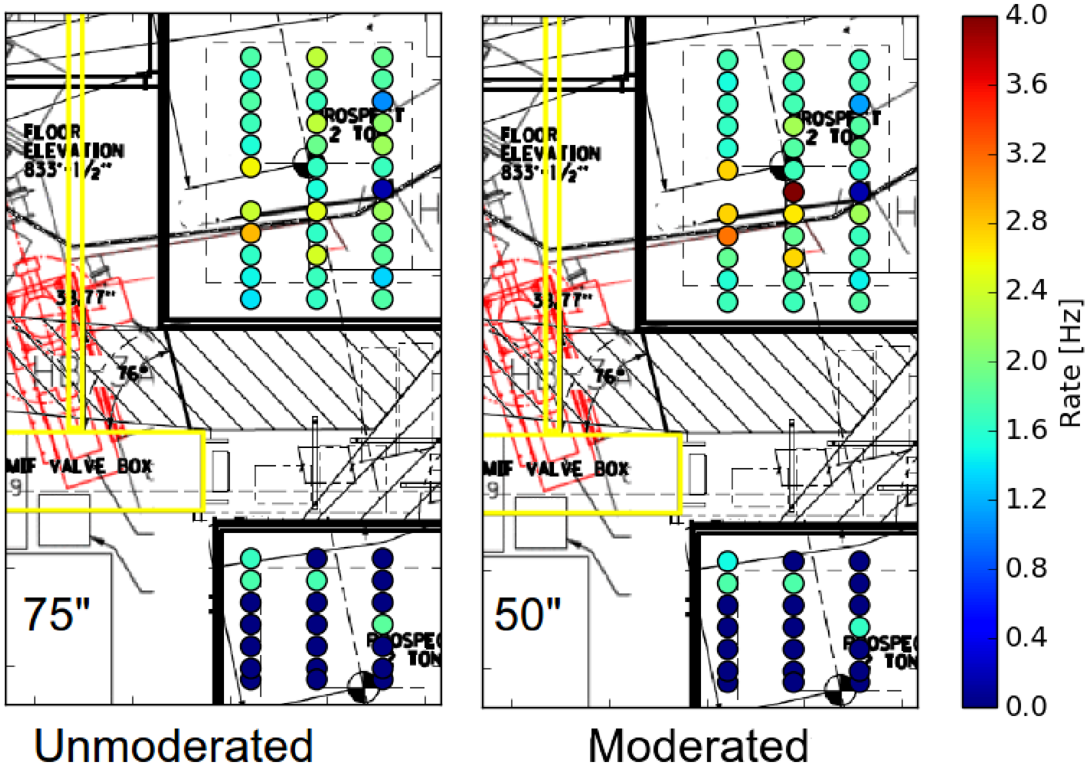

Figure B.4: 2" ^{3}He thermal neutron rates at different positions throughout the planned near and far positions of PROSPECT during reactor-off. Left plot shows rates from the unmoderated detector 75" above the floor and right plot shows rates moderated by 1" of high-density polyethylene at 50" above the floor.

Appendix C

Additional Background Simulation Figures

This chapter includes additional figures relevant to the simulation work described in chapter 6. This includes the simulation of the radioactive source calibrations with ^{137}Cs and ^{207}Bi, the reactor-off and MIF reconstructed histograms in terms of incident gamma energies, and additional AD-1 detector simulations.

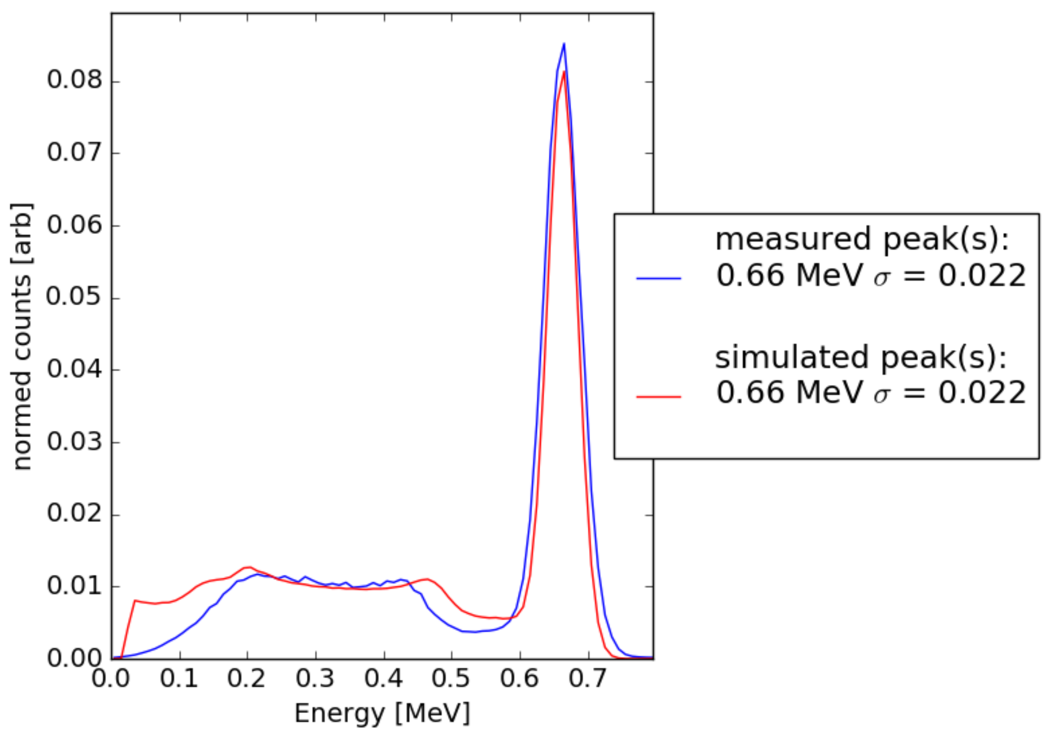

Figure C.1: Simulation of a ^{137}Cs source capsule located 6" from the surface of a large NaI detector. Data was taken for 5 minutes with an hour of background used for background subtraction.

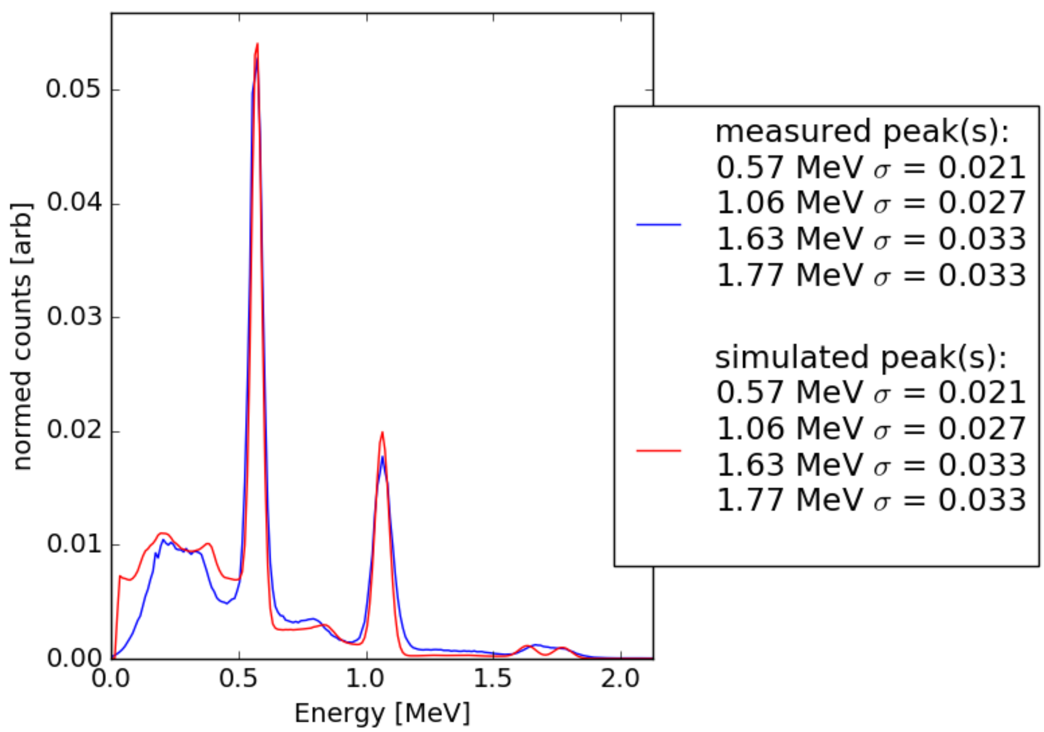

Figure C.2: Simulation of a ^{207}Bi source capsule located 6" from the surface of a large NaI detector.

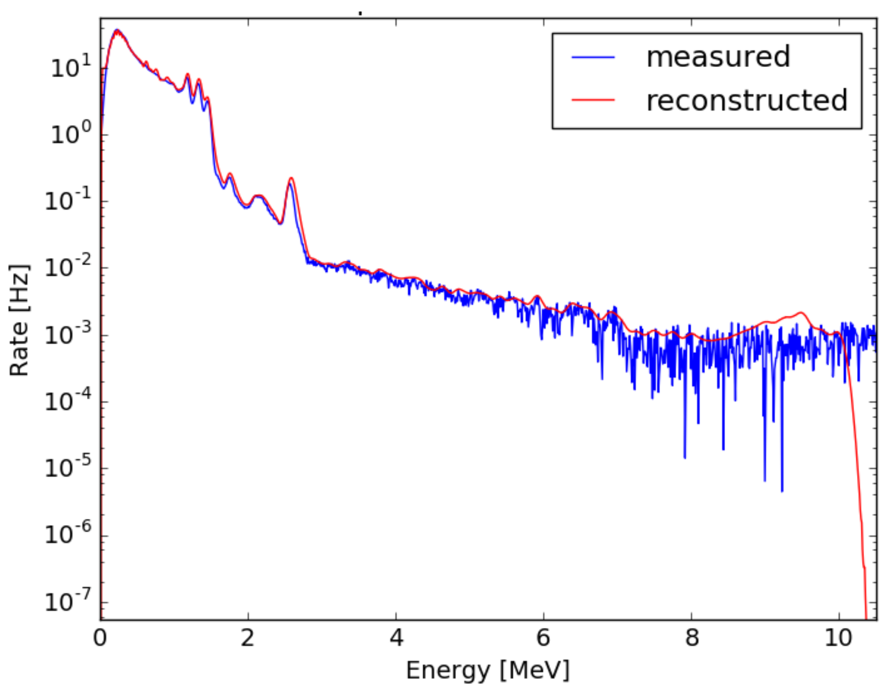

Figure C.3: reactor-off background (blue) plus reconstructed background (red) using simulated gammas. For this reconstruction, $\frac{\sum_i |R_i^{meas} - R_i^{reconst}|}{\sum_i R_i^{meas}} = 0.07$, where R_i is the rate at energy bin i.

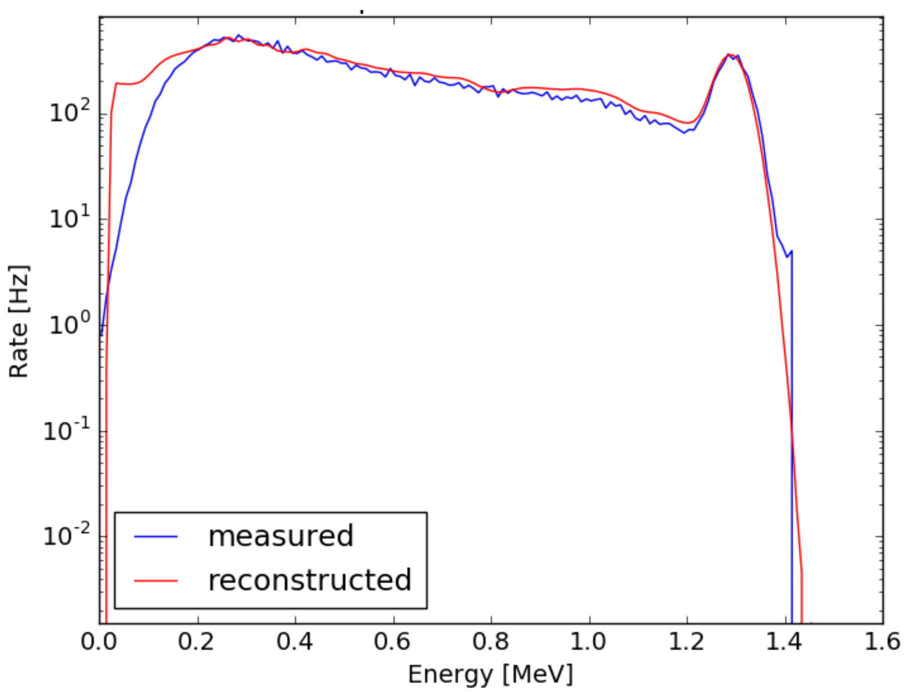

Figure C.4: Background from the MIF experiment (blue) plus simulation reconstruction (red). For this reconstruction, $\frac{\sum_i |R_i^{meas} - R_i^{reconst}|}{\sum_i R_i^{meas}} = 0.12$, where R_i is the rate at energy bin i.

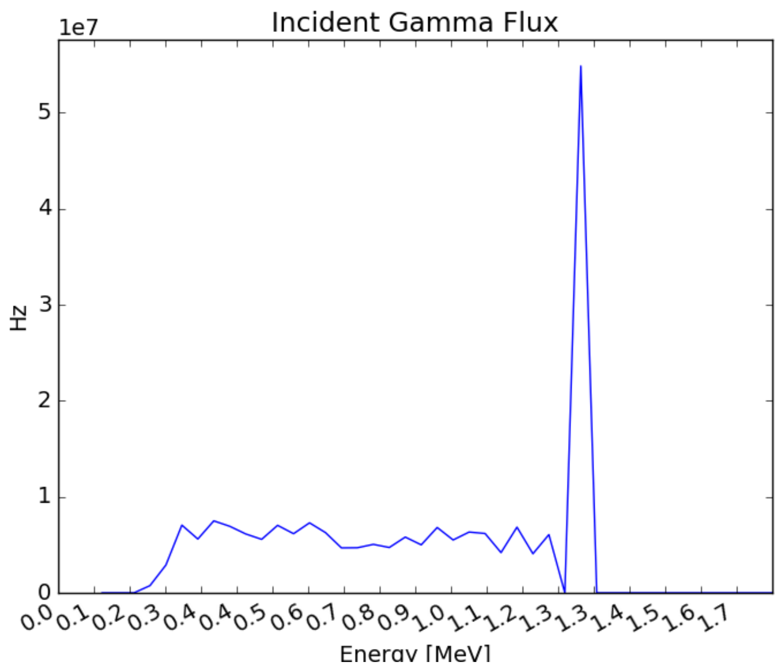

Figure C.5: Incident gamma spectrum for radiation detected from the MIF line. The reason it is not a pure ^{41}Ar spectrum is that it is shielded by lead, so many of the gammas undergo Compton scattering before reaching the detector.

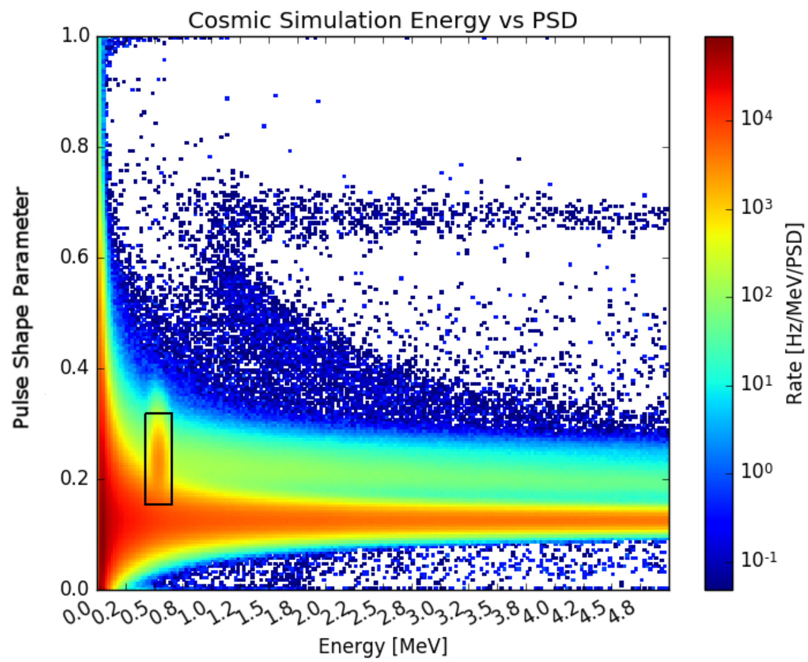

Figure C.6: Simulated PSD vs energy histogram for cosmic backgrounds in full PROSPECT AD-1 detector. Black box indicates events that are considered a neutron capture.

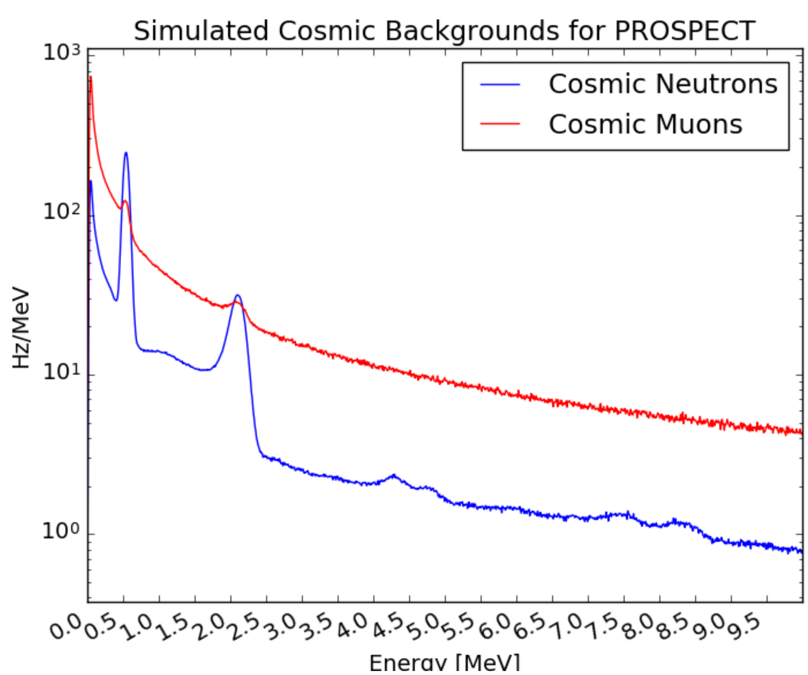

Figure C.7: Simulated energy depositions for cosmic backgrounds in full PROSPECT AD-1 detector.

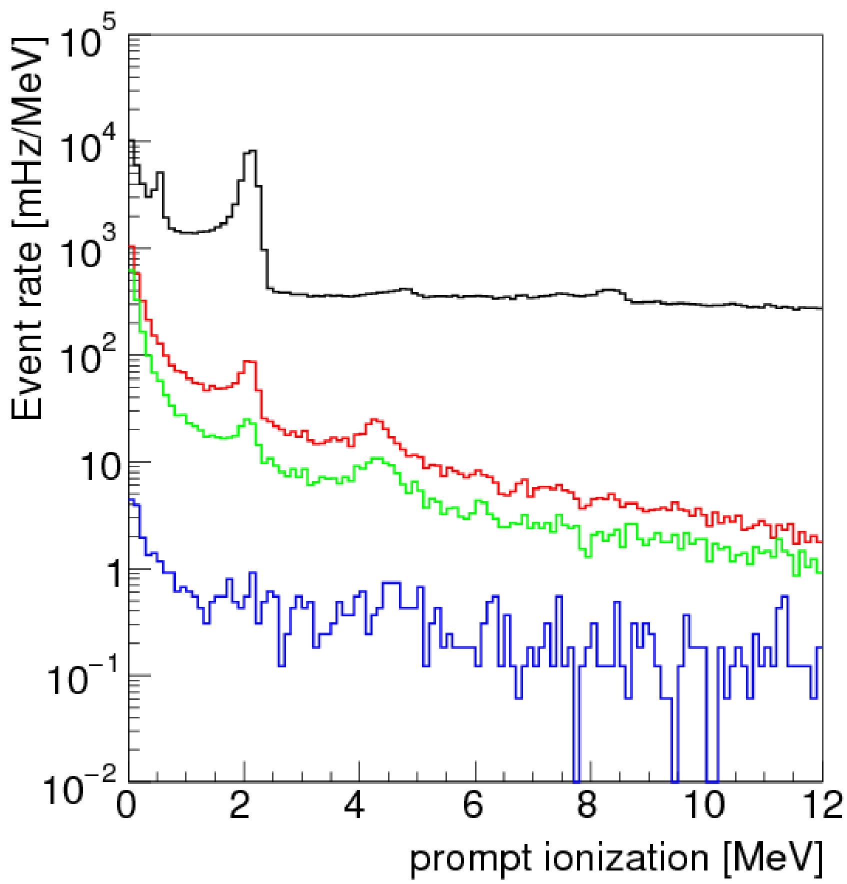

Figure C.8: IBD-like prompt energy depositions from cosmic neutron simulation. Black are positron-like ionization events that occur within 100 μs before a neutron capture. Red are events that pass the shower cut, green are events that pass the shower and topology cut, and blue are events that pass all cuts including the final fiducial cut.

Vita

Blaine Alexander Heffron was born on March 5, 1990 in Birmingham, Al. Blaine graduated from the University of North Carolina Chapel Hill in May of 2012 with a Bachelor's of Science in Physics. After working with an atmospheric modeling team at UNC's Environmental Engineering department for two years post-graduation, Blaine decided to return to study Physics, enrolling at the University of Tennessee Knoxville in the Fall of 2014 with a concentration in Experimental Nuclear Physics. Blaine will graduate with a Master's in December of 2016 and hopes to continue to be of service to those in need of problem solving, data analytics, or experimental physics services.